Advancements for Three-Dimensional Remote Sensing of the Atmosphere

William George Kulesz Martin

Submitted in partial fulfillment of the

requirements for the degree of

Doctor of Philosophy

in the Graduate School of Arts and Sciences

COLUMBIA UNIVERSITY

2014

ABSTRACT

Advancements for Three-Dimensional Remote Sensing of the Atmosphere

William George Kulesz Martin

Climate modeling efforts depend on remote sensing observations of clouds and aerosols in the atmosphere. This dissertation presents a foundation for using three-dimensional (3D) remote sensing techniques to retrieve cloud and aerosol properties in complex cloud fields. The initial research was aimed at establishing a set of single-scattering properties that could be used in subsequent 3D remote sensing applications. A theoretical stability analysis was used to evaluate what information about the particulate scattering material could be determined from *in situ* radiance and polarization measurements, and particle size and refractive index were retrieved from synthetic measurements with noise levels comparable to those of existing laboratory instruments. Subsequent research focused on the techniques necessary to retrieve 3D atmosphere and surface properties from images taken by an airborne or space-borne instrument. With the goal of using 3D retrieval methods to extend monitoring capabilities to regions with broken cloud fields, we formulated an efficient procedure for using codes that solve the 3D vector radiative transfer equation (VRTE) to adjust atmosphere and surface properties to fit multi-angle/multi-pixel polarimetric measurements of the atmosphere. Taken together, these two bodies of work contribute to ongoing research which focuses on developing new methods for retrieving aerosols in complex 3D cloud fields, and may extend monitoring capabilities to these currently unresolved scenes.

Contents

List of Figures **iii**

List of Tables **vi**

Acknowledgements **vii**

1 Introduction **1**

2 Remote sensing of airborne particles **8**
2.1 Single-scattering properties 17
2.2 Model for atmospheric remote sensing 29
2.3 Inverse problem and statistical optimization 31

3 Particle characterization **33**
3.1 Objectives 34
3.2 Aerosols, measurements and methods 37
3.3 Stability analysis results 46
3.3.1 Pure water 47
3.3.2 Sea spray 51
3.3.3 Sulfate 56
3.3.4 Tarballs 60
3.3.5 Sulfate and tarballs 64
3.3.6 Sea spray and tarballs 68
3.4 Concluding remarks 73

4 Remote sensing in 3D **75**
4.1 Objectives 76
4.2 Preliminaries 80
4.2.1 Forward and adjoint 3D VRTEs 84
4.3 Application to remote sensing 90
4.3.1 Model for polarimetric measurements 93

4.3.2 Data misfit and gradient calculation . . . 97
4.3.3 Iterative parameter adjustment . . . 102
4.3.4 Pseudo-forward problem . . . 106
4.4 Derivation of the fundamental adjoint property . . . 108
4.4.1 The streaming operators . . . 108
4.4.1.1 Chords and boundary points . . . 111
4.4.1.2 Rules for evaluating streaming operators . . . 114
4.4.1.3 Properties of streaming operators . . . 116
4.4.2 Integral equations for 3D VRTE . . . 116
4.4.2.1 Forward integral equations . . . 118
4.4.2.2 Adjoint integral equations . . . 121
4.4.3 Fundamental adjoint property for the 3D VRTE . . . 122
4.5 Concluding remarks . . . 125

5 Summary and outlook **127**
5.1 Outlook for single-scattering . . . 129
5.2 Outlook for 3D retrievals . . . 131

Bibliography **133**

A Appendix single-scattering calculations **145**
A.1 Light scattering measurables . . . 148
A.2 Particle microphysical parametrization . . . 150
A.3 Physics and forward modeling . . . 155
A.4 Inverse problem and numerical optimization . . . 161
A.5 Uncertainty analysis and retrievals . . . 164

B Technical results for adjoint methods **169**
B.1 Equivalence of Integral and differential equations of 3D VRT . . . 169
B.2 Elementary adjoint property results . . . 173

List of Figures

2.1 Scattering and absorption efficiencies written as functions of the phase-shifted size parameter, $z = 4\pi r(m_r - 1)/\lambda$. **upper:** The ratio of the scattering crossection to the geometric crossection is plotted as a function of increasing size, and for several values of complex refractive index. The gray region indicates the *resonance* interval, $2 \leq z \leq 7$. **lower:** The ratio of the absorption crossection to the geometric volume is plotted as a function of increasing size. 19

2.2 Contour plots showing the angular distribution of scattering, $\log(P_{11}(\Theta))$, for particles near resonance. Computations in each subplot correspond to the complex refractive index written in the lower-right corner of that subplot. In each subplot, the scattering angle is plotted along the horizontal axis and the particle size parameter, $\frac{2\pi r}{\lambda}$, is plotted along the vertical axis. Color coordinated to the wavelengths written above the top row of subplots, each subplot shows a dotted line that corresponds to particles with radius of, $r = 0.1\mu\mathsf{m}$. 23

2.3 Contour plots showing the ratio of scattering element, $P_{33}(\Theta)$, to the phase function element, $P_{11}(\Theta)$. The horizontal axes show the scattering angle and vertical axes show particle size parameter. Complex refractive index layout is identical to that used in Figure 2.2. 24

2.4 Contour plots showing the ratio of scattering element, $P_{12}(\Theta)$, to the phase function element, $P_{11}(\Theta)$. The horizontal axes show the scattering angle and vertical axes show particle size parameter. Complex refractive index layout is identical to that used in Figure 2.2. 25

2.5 Contour plots showing the ratio of scattering element, $P_{34}(\Theta)$, to the phase function element, $P_{11}(\Theta)$. The horizontal axes show the scattering angle and vertical axes show particle size parameter. Complex refractive index layout is identical to that used in Figure 2.2. 26

3.1 The microphysical parameterization and single-scattering properties of water droplets and sea spray. For each of these types of aerosols there are two rows of plots, showing the following quantities from left to right. **Rows 1&3:** (1) The total concentration of particles, (2) the size distribution as a function of particle radius, as in Eq. 3.1 and the basis functions, φ_k functions plotted below, (3) real refractive index as a function of wavelength, and (4) imaginary refractive index as a function of wavelength. Error bars show the standard deviation of the prior distribution for each particle property about its mean value. **Rows 2&4:** (1) The volume-scattering coefficient for each wavelength, (2) the volume-absorption coefficient for each wavelength, and the angular profiles of scattering matrix elements (3) $F_{11}(\Theta)/F_{11}(30°)$, (4) $F_{33}(\Theta)/F_{11}(\Theta)$, (5) $F_{12}(\Theta)/F_{11}(\Theta)$, and (6) $F_{34}(\Theta)/F_{11}(\Theta)$. Measurement error is visualized using error bars for the volume-scattering and volume-absorption coefficients and using shaded regions around the angular profiles of scattering matrix elements. 39

3.2 The microphysical parametrization of sulfate and tarballs and the single-scattering properties corresponding to the mean prior state. The layout is the same as in Fig. 3.1. 41

3.3 An aerosol mixture of sulfate and tarballs that contains equals geometric crossections of each type. The layout of particle parameters and single-scattering properties is the same as in Figure 3.1. 43

3.4 An aerosol mixture of sea spray and tarballs that contains equals geometric crossections of each type. The layout of particle parameters and single-scattering properties is the same as in Figure 3.1. 44

3.5 Water droplet prior and posterior uncertainty shown by error bars. Thin black error bars show prior uncertainty, purple error bars show posterior uncertainty without volume-coefficient measurements and pick error bars show posterior uncertainty with volume-coefficient measurements. Error patterns or principle components are plotted below the size distribution in each plot. Rows from top to bottom show increasing information. **Row 1:** Phase-profile measurements with and without volume coefficients. **Row 2:** Linear-profile measurements with and without volume coefficients. **Row 3:** Full-profile measurements with and without volume coefficients. The gray region shows resonating sizes at the shortest wavelength, $\lambda = 405$nm. 49

3.6 Synthetic retrievals of water droplets obtained by fitting full single-scattering measurements with random noise. Each row shows a randomly generated true state, selected to differ significantly from the mean. The true concentration is plotted as colored circles and the true size distribution is plotted as a colored line connecting colored circles. Retrievals are plotted with purple lines, and each corresponds to one of seven random samples of measurement error. 51

3.7 Sea spray prior and posterior uncertainty for concentration, size distribution and real refractive index. Descending rows have increasing measurements as in Figure 3.5, with purple lines and error bars corresponding to cases without volume-coefficient measurements and pink lines and error bars corresponding to cases with volume-coefficient measurements. The gray region shows resonating sizes at the shortest wavelength, $\lambda = 405$nm. 53
3.8 Synthetic retrievals of sea spray aerosols from full single-scattering measurements. The layout is similar to Figure 3.6 but including real refractive index, in the right-most column. 55
3.9 Sulfate prior and posterior uncertainty for concentration, size distribution, and real refractive index. Layout is the same as in Figure 3.5. The gray region shows resonating sizes at the shortest wavelength, $\lambda = 405$nm. . . 58
3.10 Synthetic retrievals of sulfate aerosol from full single-scattering measurements. The layout is the same as in Figure 3.8. 59
3.11 Tarballs prior and posterior uncertainty for concentration, size distribution, real refractive index and imaginary refractive index. The layout is similar to Figure 3.5, except plots of uncertainty for the real and imaginary refractive index are added in the two right-most columns. The gray region shows resonating sizes at the shortest wavelength, $\lambda = 405$nm. 62
3.12 Synthetic retrievals of tarballs from full single-scattering measurements with noise. As in Figure 3.6, each row shows a different true state with seven random samples of measurement error. 63
3.13 Prior and posterior uncertainties in for a mixture of sulfate and tarballs. The layout is similar to that of Figure 3.5. 65
3.14 Synthetic retrievals of the mixture of sulfate and tarballs from full single-scattering measurements with random samples noise. The layout is similar to Figure 3.6. 67
3.15 Prior and posterior uncertainties in for a mixture of sea spray and tarballs. The layout is similar to that of Figure 3.5. 70
3.16 Synthetic retrievals of the mixture of sea spray and tarballs from full single-scattering measurements with random samples noise. The layout is similar to Figure 3.6. 72

List of Tables

3.1 Stability analysis of pure water: degrees of freedom and bits of information 48
3.2 Relative uncertainty in pure water concentration 50
3.3 Stability analysis for sea spray: degrees of freedom and bits of information. 52
3.4 Relative uncertainty in sea spray concentration 54
3.5 Stability analysis for sulfate: degrees of freedom and bits of information . 57
3.6 Relative uncertainty in sulfate concentration 59
3.7 Stability analysis for tarballs: degrees of freedom and bits of information 61
3.8 Relative uncertainty in tarballs concentration 62
3.9 Stability analysis for the mixture of sulfate and tarballs 65
3.10 Relative uncertainty in concentration for mixed sulfate and tarballs . . . 66
3.11 Stability analysis for the mixture of sea spray and tarballs 69
3.12 Relative uncertainty in concentration for mixed sea spray and tarballs . . 71

A.1 Measurement constraints for the six subsets of complete single-scattering properties 149
A.2 Microphysical parameterizations under consideration and prior information. Spectral averages are shown for refractive index prior information. . 150

Acknowledgements

I am grateful to Lorenzo Polvani for bringing me to Columbia University, to Guillaume Bal for guiding my early efforts to simulate three-dimensional radiative transfer, and to Michael Mishchenko for reminding me to be happy. Above all others, I am grateful to Brian Cairns who did most of the dirty work. Brian met with me often, encouraged my writing efforts, and read my work. He has believed in me and allowed me the choice of my own destiny. I am also grateful to Michael Weinstein, Adam Sobel, David Keyes, Ovidiu Savin, David Bayer, and countless other members of the faculty here at Columbia University.

Yet their instruction was effective only due to prior knowledge, and I am grateful to the faculty of the Departments of Physics and Mathematics at Oregon State University for their open minds and open doors. Enrique Thomann taught me (proper) calculus and guided my first foray into computational science, along with Andy Karplus who also invited me to work in his X-ray crystallography laboratory — and then invited me over for lunch, followed by dinner.

Having worked alone recently, I can't help but miss the influence of other graduate students — like Kirk Knobelspesse, Wenjia Jing, Nick Hoel, Melinda Han, Ethan Coon, Clara Orbe, Yan Yan, Francois Monard, Casey Burlyson, and David Goluskin. You guys rock, and if my favorite is Francois, this is only because he was my roommate, and because he came from France.

Thank you to Susan Puckett for engaging me in life and to countless other friends from high school and college, including Karena Dokken and Carlin Lee. Without their support, I may have learned calculus earlier in life but I would be a different person. Thank you to my mother Molly who fooled me into piano lessons for eleven years and to my father Vincent who drove me home after most of them. Lastly thank you to my older brother Barth. It was probably his fault.

For tranquility and occupation.

Chapter 1

Introduction

The Fourth and Fifth Assessment Reports from the Intergovernmental Panel on Climate Change list aerosols as the atmospheric constituent with the most uncertain impact on global temperature change [1, 2], both through the direct radiative effects of the aerosols themselves and through the indirect effects that result from the influence of aerosols on clouds [3]. The impacts of aerosols on climate are predicted by computational models that include the processes governing sources of aerosols at the Earth's surface and the life cycle of aerosols after they are lofted into the atmosphere [4, 5]. Modeling these processes requires the guidance of accurate measurements of detailed particle microphysical properties in order to compute the correct radiative forcing [6]. The required measurements are a key service provided by the US National Aeronautics and Space Administration, through current satellite instruments and their commitment to monitoring the Earth from space. Missions planned for the coming decade place emphasis on reducing the uncertainties in

the effects of aerosols that are predicted by climate models. This includes reducing the uncertainties in radiative forcings and feedbacks, through chages to clouds, aerosols and other components of the Earth's atmosphere and surface [7].

Proper understanding of these feedbacks requires continual global monitoring of the state of Earth's atmosphere and surface. In the atmosphere, this amounts to identifying various types of aerosols with high confidence and quantifying their global impact on cloud processes. The identification of various types of aerosols is done using multi-angle polarimetry, which has been shown to provide the information needed to retrieve aerosol properties in cloud-free scenes [6, 8] and in scenes with aerosols above a strati-form cloud [9]. However, the retrieval of aerosol and cloud properties together in broken cloud fields with strong heterogeneity remains an open challenge that must be addressed to monitor the indirect effect of aerosols on clouds, and subsequent changes to cloud brightness and precipitation. Consider the case of fair-weather cumulus clouds as an example of broken cloud cover. Small and short-lived individual clouds vary on spatial scales of hundreds of meters and temporal scales of minutes, yet they comprise large fields which can extend for hundreds of kilometers, exerting significant influence over the radiation budget [10]. Moreover, fair-weather cumulus follow the diurnal cycle — they develop in late-morning and early-afternoon and in certain situations evolve into deep-convection and cause precipitation [11]. Given the dependence of cloud formation on aerosols, through their ability to act as cloud condensation nuclei (CCN), the retrieval of aerosols in fair-weather cumulus cloud fields is highly relevant. Another recurrent type of heterogeneity occurs along cloud edges, where enhanced backscattering and color ratio measurements

from CALIPSO indicate that cloud-aerosol interactions may extend as far as 15km into clear regions [12]. The ability of current technology to characterize aerosols is very limited in these regions, which are some of the most important places where clouds and aerosols mix and interact.

Issues related to retrieving cloud and aerosol properties near broken clouds arise for satellite based observations taken by the Multi-angle Imaging Spectro-Radiometer (MISR). At high spatial resolution (1km), only 17% of cloudy pixels are compatible with plane-parallel calculations of reflectance [13]. While the fraction of compatible pixels improves to 38% when data are averaged to a coarse spatial resolution of 18km, using plane-parallel radiative transfer alone leaves many gaps in coverage for aerosol and cloud retrieval products. Furthermore, averaging measurements to coarse resolution leads to biased retrievals, due to the non-linear dependence of measurements on cloud properties [11]. Another approach to increasing coverage is to fit data with weighted averages of calculations for pure-cloud and pure-aerosol columns, analogous to the fine-mode fraction retrieved by the Moderate Resolution Imaging Spectroradiometer (MODIS) [14]. However, this kind of approach neglects the spatial proximity of clouds and aerosols and limits the potential for simultaneous retrieval of structural properties like cloud height and horizontal extent.

Relative to these extensions of plane-parallel radiative transfer calculations, the use of the 3D vector radiative transfer equation (VRTE) for aerosol retrievals in broken cloud fields provides a more accurate account of the underlying radiative processes at work. As shown by Evans et. al. [15], using 3D calculations to fit simulated MISR measurements of fair-weather cumulus improves the fit with multi-angle measurements and provides

more accurate estimates of cloud optical thickness. Another kind of 3D retrieval based on stereoprogramming exploited motion-parallax effects in MISR's multi-angle data to determine cloud top height and thickness [16]. Intrisic benefits to using 3D retrievals include the removal of biases caused by the horizontal illumination of aerosols near clouds and by shadowing effects due to directional illumination of clouds. In addition, 3D retrieval methods fit well with new LIDAR and RADAR instruments which will provide cross-sectional or fully 3D constraints on atmospheric material. Two current examples are the cross-sectional constraints on aerosol backscattering by HSRL [17] and the 3D constraints on liquid-water volume concentration by microwave emission radiometry [18, 19]. These supplementary measurements effectively outline the spatial extent of clouds and aerosols, and they will provide the most benefit to aerosol property retrievals when used to impose 3D constraints on the distribution of particles in the atmosphere.

Compared with current technology, retrievals using the 3D VRTE do not impose default assumptions on spatial variability and provide the flexibility required to retrieve cloud-structure parameters in 3D, as well as to retrieve ambient aerosols in and around those clouds. The trade off is that many small-scale "independent-pixel" retrievals are replaced by a single large-scale retrieval, and there are many more unknown parameters and measurement constraints. Also, the numerical tools necessary for 3D retrievals are less well developed than the corresponding tools used in plane-parallel retrievals. While the developement of new retrieval algorithms goes beyond the scope of this dissertation, the consideration of futuristic retrievals has led us to address important issues of scale. In a recent paper we extend adjoint methods, which have been used in medical imaging

[20], to the 3D VRTE as used in remote sensing applications [21]. This contributes to the developement of 3D retrieval algorithms by showing how to use existing codes in the adjustment of 3D atmosphere and surface properties to fit multi-angle/multi-pixel polarimetric measurements.

The problem of retrieving clouds and aerosols from remote sensing measurements of the atmosphere contains, as an implicit sub-problem, the retrieval of properties which define the populations of airborne particles which make up clouds and aerosols. These properties must be infered from the way the particles scatter light, i.e. their single-scattering properties. Part of the reason for parametrizing the single-scattering properties and introducing an extra step is the following. While the scattering and absorption coefficients of aerosols may be sufficient to constrain the direct effects of aerosol, interactions between aerosols and clouds have a complicated dependence on the physical properties of aerosols. For example, the primary factor in determining cloud droplet number concentration is the number concentration of available CCN, and this is determined primarily by the number concentration and size distribution of aerosols [22, 23]. Another reason for retrieving aerosol properties is that certain types of aerosols may make good regulation targets. Regulating the emission of light-absorbing carbon (LAC) aerosols may help mitigate global warming in the short term and improve air-quality and food production [24]. Identifying LAC aerosols with high confidence would be needed to monitor compliance. One final reason is that the aerosol properties parameterize the single-scattering properties in terms of a limited number of physically meaningful unknowns.

This parameterization of aerosol and cloud properties was the focus of our initial research.

The single-scattering properties are used in the 3D VRTE and fully determine the radiative effects of scattering material in the atmosphere, though there are additional complexities due to multiple scattering and spatial variability. The single-scattering properties therefore contain more information than can be measured in the atmosphere. Understanding the limitations which are inherent to the retrieval of aerosols from measurements of single scattering, lets us form realistic expectations for retrievals in the atmosphere [25]. Furthermore, the validation of 3D retrievals of clouds and aerosols in the atmosphere will rely, to a large extent, on measurements of single-scattering properties taken *in situ* by sampling atmospheric aerosols from an aircraft in flight. These measurements may be valuable for validating the 3D retrievals of clouds and aerosols from the multisensor data of future NASA missions, e.g. the Aerosol and Cloud Ecosystem mission which will be discussed briefly in Chapter 5 as a topic of future work.

Research into the parameterization of the single-scattering properties of clouds and aerosols is complementary to our research on using adjoint methods to adjust 3D cloud and aerosol parameters in atmospheric remote sensing. Both are essential to our long-term goal of developing 3D retrieval methods that can retrieve cloud and aerosol properties in broken cloud fields. However, this is a highly challenging endevour, so we have selected intermediate objectives which will have immediate significance as well as contribute to our long term plans. Firstly, we analyze the elementary problem of retrieving particle properties from single-scattering measurements. The retrieval algorithms we developed are applicable to sub-orbital instruments that will be used to validate satellite retrieval products,

and they provide insight into the theoretical limitations which are inherent to the characterization of particles using light-scattering measurements. Secondly, we derive adjoint methods for the full 3D VRTE in order to provide the computational efficiency required for adjusting 3D atmosphere and surface parameters to fit multi-angle polarimetric and radiometric measurements.

This thesis presents background in Chapter 2 and novel research in Chapters 3 and 4. Chapter 2 gives an overview of some relevant and well-known results in the field of atmospheric remote sensing and provides background and context for our own research efforts. Chapter 3 contains the results of a systematic theoretical analysis of how much particle information can be retrieved from measurements of scatterd light [25]. Chapter 4 derives adjoint methods and describes and efficient method for adjusting 3D cloud and aerosol properties to fit radiometric and polarimetric measurements of scattered sunlight [21]. A summary and brief description of plans for future work is presented in Chapter 5.

Chapter 2

Remote sensing of airborne particles

To relate our work to current remote sensing efforts, this chapter describes the components that make up a system for observing airborne particles. These include measurements, a forward model, and tools of statistical inference [26]. Each observation system is built around measurements, and for the remote sensing of clouds and aerosols in the atmosphere we are interested in radiometric or polarimetric measurements of scattered sunlight or thermal emission. The observation system must then use these measurements to infer the state of the atmosphere and surface. That is, to constrain unknown parameters such as cloud droplet effective radius, cloud optical thickness, trace gas concentrations, temperature profile, surface albedo, and so forth. The forward model relates these unknown parameters to the observations, rigorously as a function with inputs for each unknown parameter and outputs for each measurement. Statistical inference is then used to select the state of the atmosphere and surface which agrees most closely with observations and

prior information. Clouds and aerosols are composed of small airborne particles, and we seek to quantify the abundance of these particles as well as their microphysical properties: like their size distribution, shape, and complex refractive index. Measurements generally couple scattering from the surface and atmosphere so as to require the retrieval of both together. The objective is to process the radiometric and polarimetric measurements in order to estimate the state of the atmosphere and surface to within reliable estimates of uncertainty, and to provide these estimates as a data product for use by the scientific community.

Our work concerns two distinct types of observations that we refer to as *single-scattering* and *multiple-scattering* measurements. The first measurable quantities that we consider are the single-scattering properties of aerosols. Measurements of these are made in controlled laboratory settings [27, 28] and made *in situ*, both at surface observation sites [29, 30] and inside aircrafts during field campaigns [31]. The single-scattering properties provide a complete set of coefficients for the radiative transfer equation, which can then be used to model measurements of the atmosphere. So in that sense, they completely characterize how the airborne particles interact with radiation in small volumes of the atmosphere. The second type of measurement is taken in the atmosphere where multiple orders of scattering occur. These data present a much greater challenge to observation systems since atmosphere and surface properties can vary in space, and this variability must also be determined from the measurements. Moreover, the process of multiple scattering has smoothing effects which wipe out information contained in angular features, e.g. halos and rainbows, which might otherwise be useful in resolving the physical

properties of clouds and aerosols.

The foundation for using the VRTE to model measurements of incoherent light dates back to 1852, when George Gabriel Stokes derived a representation for keeping track of the measurable radiative effects caused by light incident on a detector [32]. Four parameters are needed and these are denoted by I, Q, U, and V. The intensity, I, can be integrated over the crossection of a detector and solid angle of view to give the total incident power. However, it is an incomplete characterization of incoherent light due to the underlying transverse oscillations which are to be measured. All four Stokes parameters are needed to compute the measurements of an ideal polarization analyzer (an optical device made up of a polarizer, retarder and detector). As described by Mishchenko et al. [33], radiation propagating in direction, $\boldsymbol{v}$, consists of electromagnetic oscillations in the transverse directions, denoted by $\boldsymbol{\theta}$ with $0 = \boldsymbol{\theta} \cdot \boldsymbol{v}$ and $\boldsymbol{\varphi} = \boldsymbol{v} \times \boldsymbol{\theta}$. Suppose that we place, in front of the detector, a polarizer with axis of transmission along the transverse direction,

$$\boldsymbol{p} = \boldsymbol{\theta} \cos(\eta) + \boldsymbol{\varphi} \sin(\eta), \tag{2.1}$$

and after this a retarder, which introduces a phase shift of $+\zeta/2$ in waves along the $\boldsymbol{\theta}$ axis and a phase shift of $-\zeta/2$ in waves along the $\boldsymbol{\varphi}$ axis. The specific intensity, $\hat{y}$, which is measured by the detector will now be a function of measurement variables, η and ζ:

$$\hat{y}(\eta, \zeta) = \frac{1}{2}(I + Q\cos(2\eta) - U\sin(2\eta)\cos(\zeta) - V\sin(2\eta)\sin(\eta)). \tag{2.2}$$

The measured intensity scales linearly with each Stokes parameter and the full set is required to compute accurate predictions for arbitrary measurement variables, η and ζ. That is, all four Stokes parameters are needed to fully characterize the transverse oscillations which can be measured by a polarization analyzer and retarder. The observations of interest are made of quasi-monochromatic light, in which case the Stokes parameters satisfy the following inequality:

$$I^2 \geq Q^2 + U^2 + V^2. \tag{2.3}$$

This dissertation assumes the use of the VRTE in solving for the Stokes parameters and in analyzing measurements, but it is important to comment that this model is an approximation to the macroscopic Maxwell's equations, which more generally describe the physics of electromagnetic waves in the Earth's atmosphere. As an approximation, there are limitations to the useful application of the VRTE.

This point is emphasized by a brief remark on the add-ability of Stokes parameters, a property that is essential to the usage of the VRTE, for which the solution is a linear function of light sources. As discussed by Mishchenko et al. [33], a quasi-monochromatic beam of light can be thought of as an incoherent superposition of mono-chromatic plane waves. The Stokes parameters are defined as time-averaged, quadratic combinations of the amplitudes of transverse electromagnetic field oscillations. Given the "squaring" of these amplitudes it may seem strange, at first, that the Stokes vectors are addable since the amplitudes themselves must be addable in accordance with the super-position principle of

Maxwell's equations. Adding two coherent plane waves quadruples the measured intensity when they are in phase, and results in a measured intensity of zero when they are out of phase. The apparent issue is resolved for the addition of incoherent light sources, that is, light sources which have random differences in their frequency or phase. In such situations, the Stokes parameters for the combination of the two light sources is equal to the sum of the Stokes vectors for the individual light sources. Therefore, the incoherence of light sources is essential to the useful application of the VRTE.

Having introduced the four Stokes parameters and discussed their importance for computing polarimetric measurements, we now discuss how the VRTE is used to connect the properties of airborne particles to these measurements. Particles affect the Stokes parameters through absorption, and scattering. Energy is absorbed in proportion to the volume-absorption coefficient, σ_{abs}, and scattered in proportion to the volume-scattering coefficient, σ_{sca}, and both of these processes affect all Stokes parameters equally[1]. The Stokes parameters are addable and scalable, and therefore naturally considered to be elements of a four-component vector:

$$\boldsymbol{u}(\boldsymbol{x},\boldsymbol{v}) = \begin{bmatrix} I(\boldsymbol{x},\boldsymbol{v}) \\ Q(\boldsymbol{x},\boldsymbol{v}) \\ U(\boldsymbol{x},\boldsymbol{v}) \\ V(\boldsymbol{x},\boldsymbol{v}) \end{bmatrix}. \tag{2.4}$$

[1] in the absence of dichroism which is negligible in the cases of interest

Unlike the process of absorption where energy is lost, the process of scattering redirects energy conservatively. In the redirection of this energy, the Stokes parameters are transformed according to a 4×4 matrix operation. Collectively, the processes of absorption and scattering are described in a volumetric region by the 3D VRTE:

$$\boldsymbol{v} \cdot \nabla \boldsymbol{u} + \sigma \boldsymbol{u} - \mathscr{Z}[\,\boldsymbol{u}\,] = \boldsymbol{f}_{\odot}, \tag{2.5}$$

where the volume-extinction coefficient, σ, is the sum of the volume-absorption and volume-scattering coefficients, $\sigma = \sigma_{\text{abs}} + \sigma_{sca}$. Scattering is described by the linear integral operator, $\mathscr{Z}[\,\cdot\,]$. The Stokes-vector solution, $\boldsymbol{u}$, depends linearly on any internal sources, defined by the source vector $\boldsymbol{f}_{\odot}$, and on incoming radiation which will be described in Chapter 4.

The scattering operator, $\mathscr{Z}$, is written explicitly as follows:

$$\mathscr{Z}[\,\boldsymbol{u}\,](\boldsymbol{x}, \boldsymbol{v}) = \frac{1}{4\pi} \int_{\mathbb{S}^2} \boldsymbol{Z}(\boldsymbol{x}, \boldsymbol{v}, \boldsymbol{v}') \boldsymbol{u}(\boldsymbol{x}, \boldsymbol{v}') \, \mathrm{d}S_{\boldsymbol{v}'}, \tag{2.6}$$

where the Stokes vector at each outgoing direction, $\boldsymbol{v}$, is computed by integrating over all incoming directions, $\boldsymbol{v}'$. In the cases of interest, which will include the scattering of randomly oriented particles with a plane of mirror symmetry, the scattering kernel, $\boldsymbol{Z}$, is a 4×4 matrix-valued function which has the simplified form [34]:

$$\boldsymbol{Z}(\boldsymbol{x}, \boldsymbol{v}, \boldsymbol{v}') = \boldsymbol{L}\left(\alpha(\boldsymbol{v}, \boldsymbol{v}')\right) \boldsymbol{F}\left(\Theta(\boldsymbol{v}, \boldsymbol{v}')\right) \boldsymbol{L}\left(\alpha'(\boldsymbol{v}, \boldsymbol{v}')\right), \tag{2.7}$$

where the scattering matrix, $\boldsymbol{F}$, depends only on the scattering angle, $\Theta = \arccos(\boldsymbol{v} \cdot \boldsymbol{v}')$, between incoming and outgoing directions:

$$\boldsymbol{F}(\Theta) = \begin{bmatrix} F_{11}(\Theta) & F_{12}(\Theta) & & \\ F_{12}(\Theta) & F_{22}(\Theta) & & \\ & & F_{33}(\Theta) & F_{34}(\Theta) \\ & & -F_{34}(\Theta) & F_{44}(\Theta) \end{bmatrix}. \tag{2.8}$$

The rotation matrices, $\boldsymbol{L}(\alpha')$ and $\boldsymbol{L}(\alpha)$, account for the transformation of Stokes vectors from the standard basis to the plane of scattering, and then back to the standard basis. The rotation matrices correspond to the choice of standard spherical coordinates in defining transverse directions, $\boldsymbol{\theta}$ and $\boldsymbol{\phi}$, and they are written as follows:

$$\boldsymbol{L}(\alpha) = \begin{bmatrix} 1 & & & \\ & \cos(2\alpha) & -\sin(2\alpha) & \\ & \sin(2\alpha) & \cos(2\alpha) & \\ & & & 1 \end{bmatrix}, \tag{2.9}$$

with arguments, α' and α, given by:

$$\alpha'(\boldsymbol{v}, \boldsymbol{v}') = \arccos\left(\frac{\boldsymbol{v}' \times \hat{\boldsymbol{z}}}{||\boldsymbol{v}' \times \hat{\boldsymbol{z}}||} \cdot \frac{\boldsymbol{v}' \times \boldsymbol{v}}{||\boldsymbol{v}' \times \boldsymbol{v}||} \right), \tag{2.10}$$

$$\alpha(\boldsymbol{v}, \boldsymbol{v}') = \arccos\left(\frac{\boldsymbol{v} \times \hat{\boldsymbol{z}}}{||\boldsymbol{v} \times \hat{\boldsymbol{z}}||} \cdot \frac{\boldsymbol{v} \times \boldsymbol{v}'}{||\boldsymbol{v} \times \boldsymbol{v}'||} \right). \tag{2.11}$$

The unit vector along the z-axis, $\hat{\boldsymbol{z}}$, corresponds to the direction with polar coordinate

equal to zero, $\theta = 0$. Based on the Eqs. (2.5) - (2.11), we can see that the properties which govern these Stokes parameters, and therefore measurements, are the single-scattering properties. For a certain light-source the Stokes vector is determined entirely by the volume-absorption coefficient, σ_{abs}; the volume-scattering coefficient, σ_{sca}; and the angularly-dependent elements of volume-scattering matrix, $\boldsymbol{F}(\Theta)$.

In remote sensing applications, these single-scattering properties are derived for atmospheric particle populations by solving Maxwell's equations. The far field radiative effects of individual particles are computed for an incident plane wave of radiation, and these are averaged over all orientations and a distribution of many types of particles to compute the single-scattering properties which enter into the VRTE. The parameters which define the distribution of particles include the density or concentration of particles, their complex refractive index, and the parameters which define the distribution of particle sizes and shapes. These are the target parameters of the retrieval algorithms and the unknowns which must be inferred from measurements

The single-scattering properties of an individual particle are determined by the electromagnetic field that is produced when it is illuminated with a plane wave of quasi-monochromatic light. For a spherical particle these are functions of the microphysical state variable,

$$\boldsymbol{\xi} = \begin{bmatrix} r \\ m_r \\ m_i \end{bmatrix}, \tag{2.12}$$

where r is particle radius and $m = m_r(\lambda) + \mathrm{i}m_i(\lambda)$ is the complex refractive index at wavelength λ, using Lorenz-Mie theory. They are written as $\sigma_{\text{mono}}(\boldsymbol{\xi})$ and $\boldsymbol{F}_{\text{mono}}(\theta; \boldsymbol{\xi})$. Poly-disperse populations consisting of particles with different sizes and refractive indices are represented by the measure $\mathrm{d}N(\boldsymbol{\xi})$ over the continuum of states $\boldsymbol{\xi} \in \boldsymbol{\Xi}$. This differential form is defined explicitly in Appendix A.2, as a function of unknown parameters. It can be integrated over subsets of state space to obtain the number concentration of such particles. In particular, integrating over the entire state space gives the total number concentration:

$$N_0 = \int_{\boldsymbol{\Xi}} \mathrm{d}N(\boldsymbol{\xi}), \tag{2.13}$$

which has units of particles/cm^3. The scattering of poly-disperse populations is computed by solving macroscopic Maxwell's equations for one particle at a time and evaluating the integral over $\mathrm{d}N(\boldsymbol{\xi})$ numerically:

$$\sigma = \int_{\boldsymbol{\Xi}} \sigma_{\text{mono}}(\boldsymbol{\xi})\, \mathrm{d}N(\boldsymbol{\xi}), \tag{2.14}$$

$$\boldsymbol{F}(\theta) = \int_{\boldsymbol{\Xi}} \boldsymbol{F}_{\text{mono}}(\theta; \boldsymbol{\xi})\, \mathrm{d}N(\boldsymbol{\xi}). \tag{2.15}$$

These equations are strictly valid for the average scattering of infinitely many particles for which measurements are made one particle at a time. However, under certain assumptions which include the wide separation of individual particles, the use of Eqs. (2.14) and (2.15) in computing single-scattering properties for the VRTE is justifiable as an approximation for computing polarimetric observations [33].

In Section 2.1 we discuss the single-scattering properties of spherical aerosols and describe how scattering behavior changes with the wavelength of light and with particle properties like size and complex refractive index. In Section 2.2 we discuss the use of the VRTE modeling observations of the atmosphere. Lastly, in Section 2.3 we describe the methods of statistical inference which are commonly used to develop iterative retrieval algorithms and to provide uncertainty estimates for the retrieved parameters.

2.1 Single-scattering properties

This section aims to visualize the single-scattering properties which were introduced in the previous section as coefficients of the 3D VRTE. Specifically, we will focus on the volume-scattering coefficient, the volume-absorption coefficient, and the volume-scattering matrix elements — looking at how these single-scattering properties change as functions of particle properties. The calculations shown are for spherical particles and were generated with a Mie code developed by Mishchenko [35]. The output single-scattering properties are averaged over a vary narrow distribution of sizes, approximately equal to the resolution of the plots shown. This avoids sharp discontinuities in the figures which are sometimes caused by the inadvertent sampling of micro-resonances if averaging is not used.

The first quantities considered are the volume-scattering and volume-absorption coefficients. They are computed from the volume-extinction coefficient and scattering matrix

in Eqs. (2.14) and (2.15):

$$\sigma_{\text{sca}} = \frac{1}{2}\int_0^{\pi} F_{11}(\Theta)\ \sin(\Theta)\ \mathrm{d}\Theta, \tag{2.16}$$

$$\sigma_{\text{abs}} = \sigma - \sigma_{\text{sca}}, \tag{2.17}$$

and they are functions of wavelength, λ, in addition to being functions of the particle properties: r, m_r, and m_i. Instead of visualizing these directly, we look at the so-called scattering and absorption *efficiencies*, which are obtained by normalizing by the geometric cross-sectional area of the particles, or by their geometric volume. We also visualize the efficiencies as a function of the phase-shifted size parameter:

$$z = \frac{4\pi r(m_r - 1)}{\lambda}. \tag{2.18}$$

The efficiencies are shown in Figure 2.1. To visualize the scattering of a particle, we show the ratio of the particle's scattering crossection to it's geometric crossection:

$$Q_{\text{sca}}(z, m_r, m_i) = \frac{\sigma_{sca}(\lambda,\ z\lambda/(4\pi(m_r - 1)),\ m_r,\ m_i)}{\pi r^2}, \tag{2.19}$$

which is independent of wavelength, except through the implicit wavelength dependence of the phase-shifted size parameter and complex refractive index. To visualize the absorption of a particle, we show the ratio of the particle's absorption crossection to its geometric

volume:

$$E_{\text{abs}}(z, \lambda, m_r, m_i) = \frac{\sigma_{abs}(\lambda,\, z\lambda/(4\pi(m_r - 1)),\, m_r,\, m_i)}{\frac{4}{3}\pi r^3}, \tag{2.20}$$

noting that this quantity scales with the inverse of the wavelength of light.

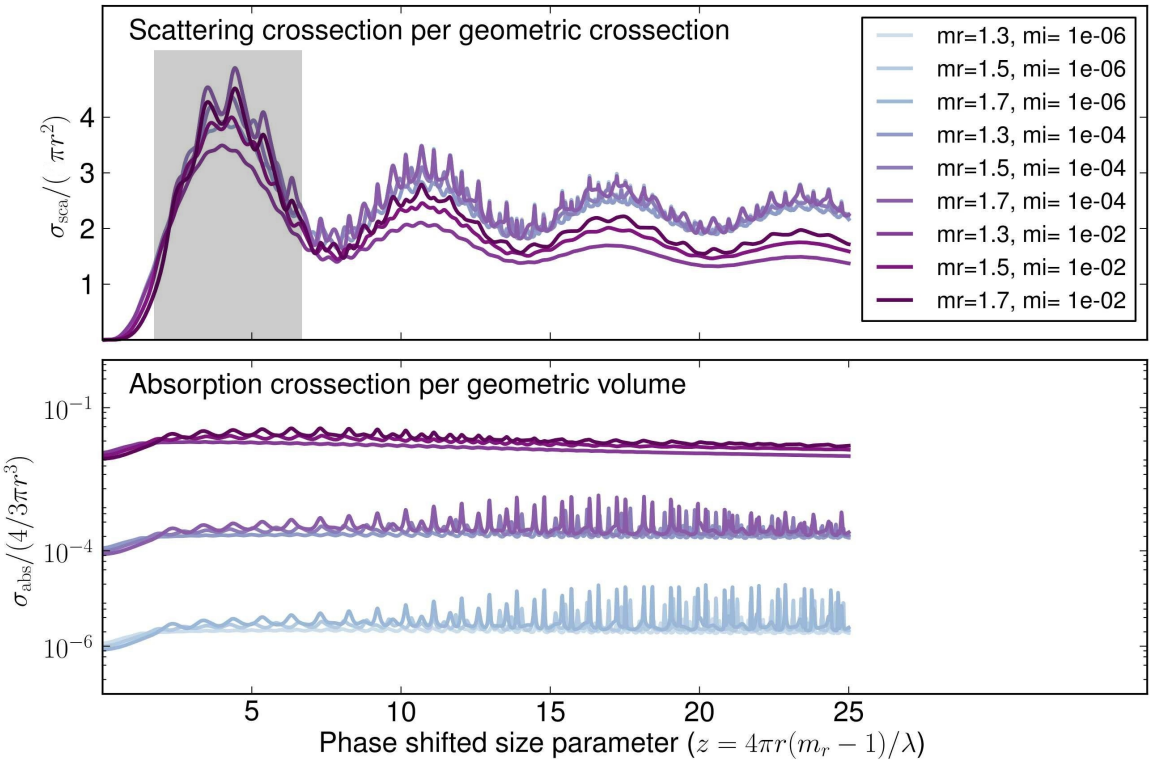

FIGURE 2.1: Scattering and absorption efficiencies written as functions of the phase-shifted size parameter, $z = 4\pi r(m_r - 1)/\lambda$. **upper:** The ratio of the scattering crossection to the geometric crossection is plotted as a function of increasing size, and for several values of complex refractive index. The gray region indicates the *resonance* interval, $2 \leq z \leq 7$. **lower:** The ratio of the absorption crossection to the geometric volume is plotted as a function of increasing size.

By plotting the scattering efficiency as a function of the phase-shifted size parameter, the crests and troughs are aligned for all values of the real-refractive index. This allows us to define particles as *resonating* when their phase-shifted size parameter is on the following

interval:

$$2 \leq z = \frac{4\pi r(m_r - 1)}{\lambda} \leq 7. \tag{2.21}$$

Henceforth, we refer to particles in this interval as *resonating* at a certain wavelength of light, λ. Such particles have maximal scattering crossection for their geometric crossection — scattering up to four times more energy than their geometric crossection might indicate. The interval of resonance is a helpful reference for interpreting, in Chapter 3, the loss of information as particles become smaller than about one-quarter the measured wavelength of light.

Particles which are smaller than the resonance size have volume-scattering coefficient which decreases rapidly with increasing wavelength, and decreasing size and mass:

$$\sigma_{\text{sca}} \sim \frac{r^6}{\lambda^4} \text{ (Aerosol Number Concentration)}, \tag{2.22}$$

$$\sim \frac{r^3}{\lambda^4} \text{ (Aerosol Mass Concentration)}. \tag{2.23}$$

Particles become invisible to detection by scattering very rapidly below the interval of resonance. One implication is that clouds become non-scattering at longer wavelengths.

Absorption behaves rather differently, with absorption depending on the total mass concentration independent of how small individual particles become:

$$\sigma_{abs} \sim \frac{r^3 m_i}{\lambda} \text{ (Aerosol Number Concentration)}, \tag{2.24}$$

$$\sim \frac{m_i}{\lambda} \text{ (Aerosol Mass Concentration)}. \tag{2.25}$$

The implication is that accurate measurements of absorption may add information about the presence of particles which are too small to recover by scattering measurements alone. The dependence on imaginary refractive index, m_i, as seen in Figure 2.1 also suggests the importance of absorption measurements in retrieving this parameter. One further implication is that although the scattering of fine-mode aerosols is negligible at infra-red wavelengths, their absorption can be significant if their imaginary refractive index is large enough.

The other single-scattering properties are described by the angular profiles of scattering matrix elements. These profiles are representative of the elements of the volume-scattering matrix written in Eq. (2.15), and therefore describe how the process of scattering transforms the angular distribution of the intensity and polarization of light. To remove the dependence of scattering-matrix elements on the volume-scattering coefficient, we use the angular profile of the log of the normalized phase function,

$$\log\left(\frac{F_{11}(\Theta)}{\frac{1}{2}\int_0^\pi F_{11}(\Theta)\sin(\Theta)\mathrm{d}\Theta}\right), \tag{2.26}$$

and the ratios of the other scattering matrix elements to $F_{11}(\Theta)$:

$$\frac{F_{12}(\Theta)}{F_{11}(\Theta)}, \qquad \frac{F_{33}(\Theta)}{F_{11}(\Theta)}, \quad \text{and} \qquad \frac{F_{34}(\Theta)}{F_{11}(\Theta)}. \tag{2.27}$$

These normalized profiles depend on particle size through the *standard* size parameter, $x = 2\pi r/\lambda$, more closely than on the phase-shifted size parameter in Eq. (2.18), so the standard size parameter is used in visualizing them. The profiles are shown using the contour plots in Figures 2.2 - 2.5, for each of the four elements of the scattering matrix. The scattering angle is plotted along the horizontal axis, from forward scattering when $\Theta = 0°$, to back scattering when $\Theta = 180°$. The size parameter is increased along the vertical axis. Each figure contains several rows and columns of subplots, corresponding to slightly different real and imaginary complex refractive indices — the real refractive index is increased vertically from bottom to top, and the imaginary refractive index is increased horizontally from left to right.

Calculations for various values of complex refractive index are shown to help us consider how the angular-profiles of scattering matrix elements change with particle size and complex refractive index. For very small particles all profiles are indistinguishable from the Rayleigh scattering of molecules. The Rayleigh like behavior persists for the phase function until the size parameter increases above one half, and for the other four scattering profiles until the size parameter increases above one or two. Below these size parameters there is little change in the angular profiles, both as functions of small changes in size and

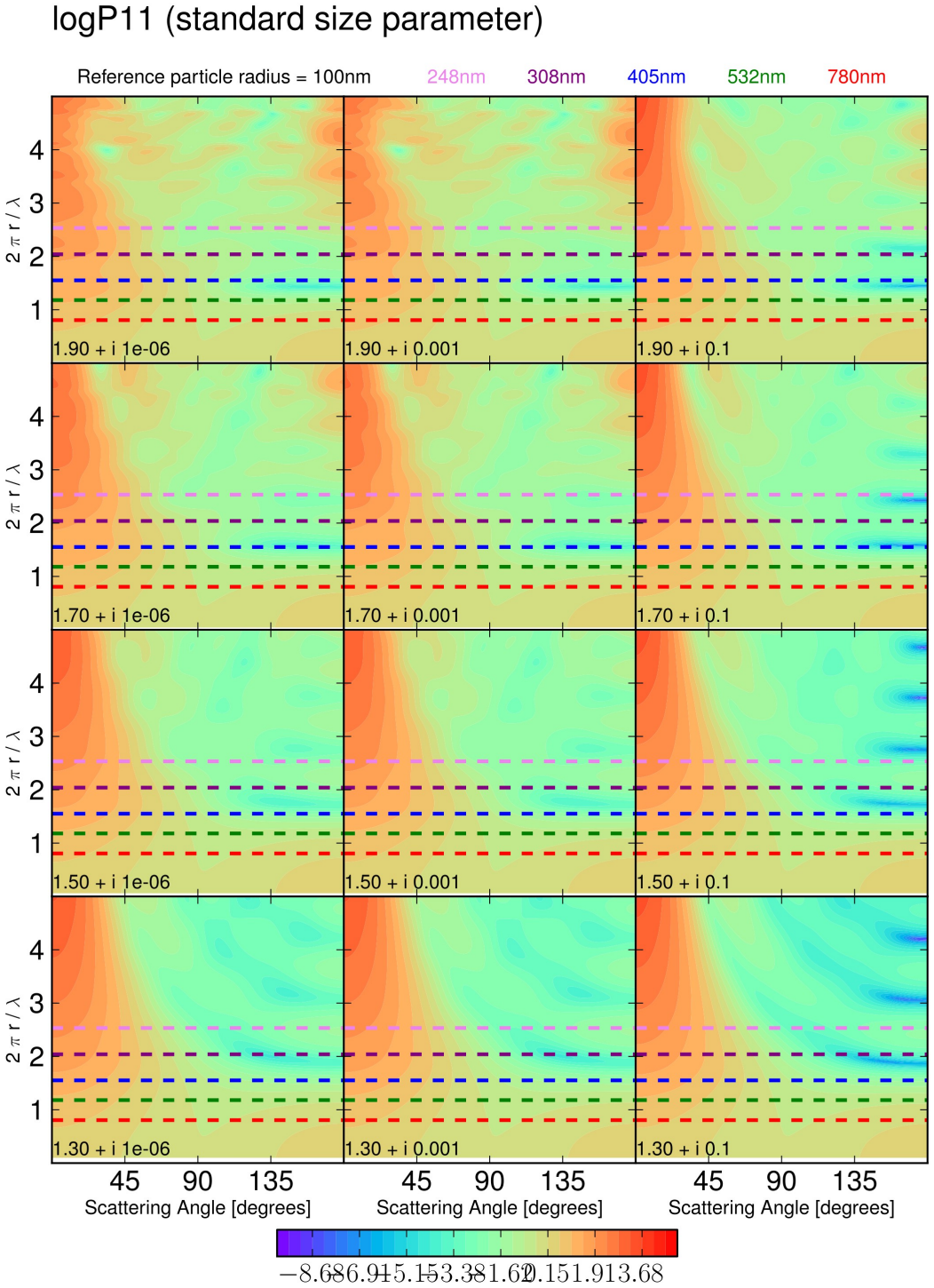

FIGURE 2.2: Contour plots showing the angular distribution of scattering, $\log(P_{11}(\Theta))$, for particles near resonance. Computations in each subplot correspond to the complex refractive index written in the lower-right corner of that subplot. In each subplot, the scattering angle is plotted along the horizontal axis and the particle size parameter, $\frac{2\pi r}{\lambda}$, is plotted along the vertical axis. Color coordinated to the wavelengths written above the top row of subplots, each subplot shows a dotted line that corresponds to particles with radius of, $r = 0.1\mu$m.

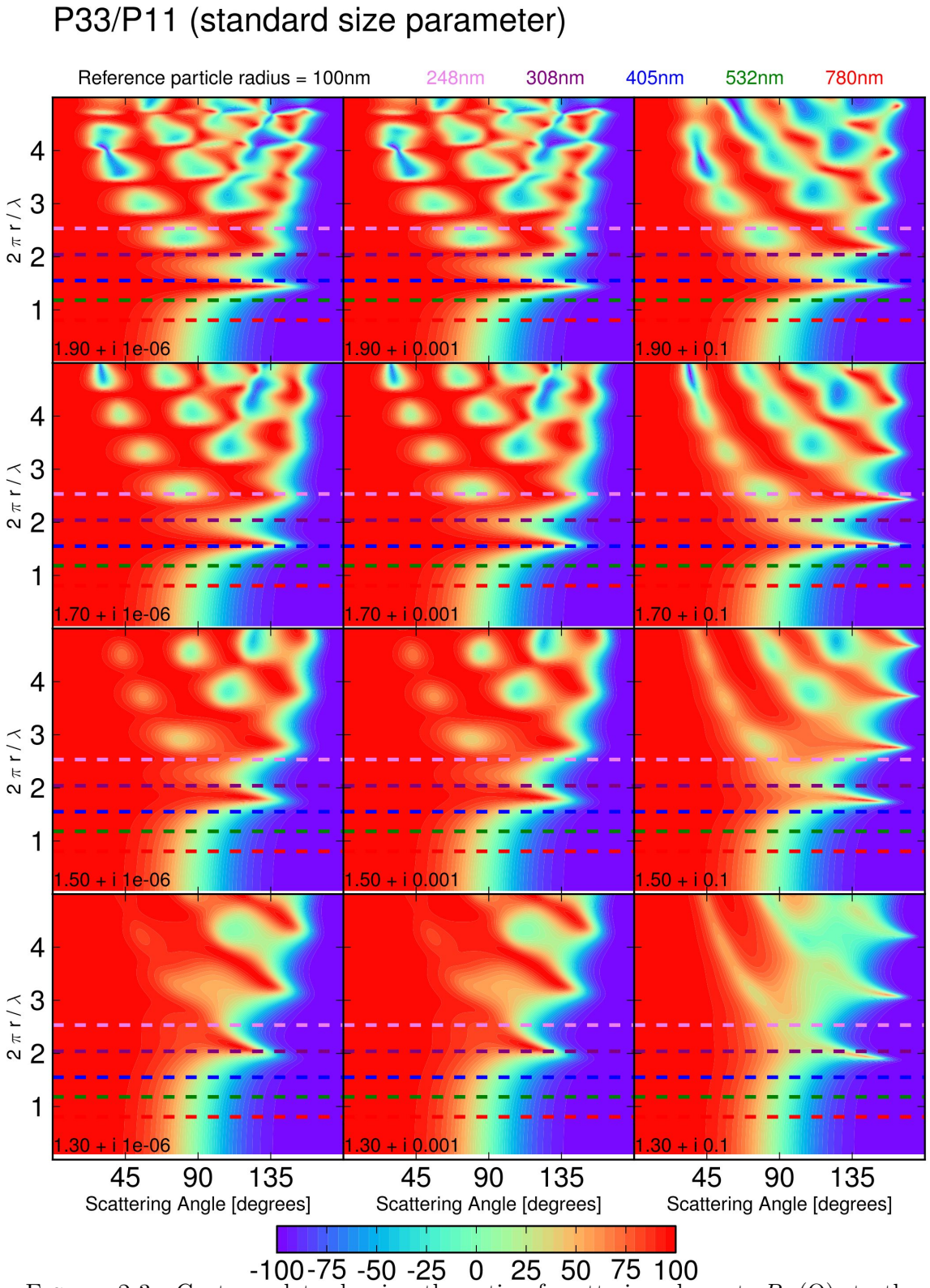

FIGURE 2.3: Contour plots showing the ratio of scattering element, $P_{33}(\Theta)$, to the phase function element, $P_{11}(\Theta)$. The horizontal axes show the scattering angle and vertical axes show particle size parameter. Complex refractive index layout is identical to that used in Figure 2.2.

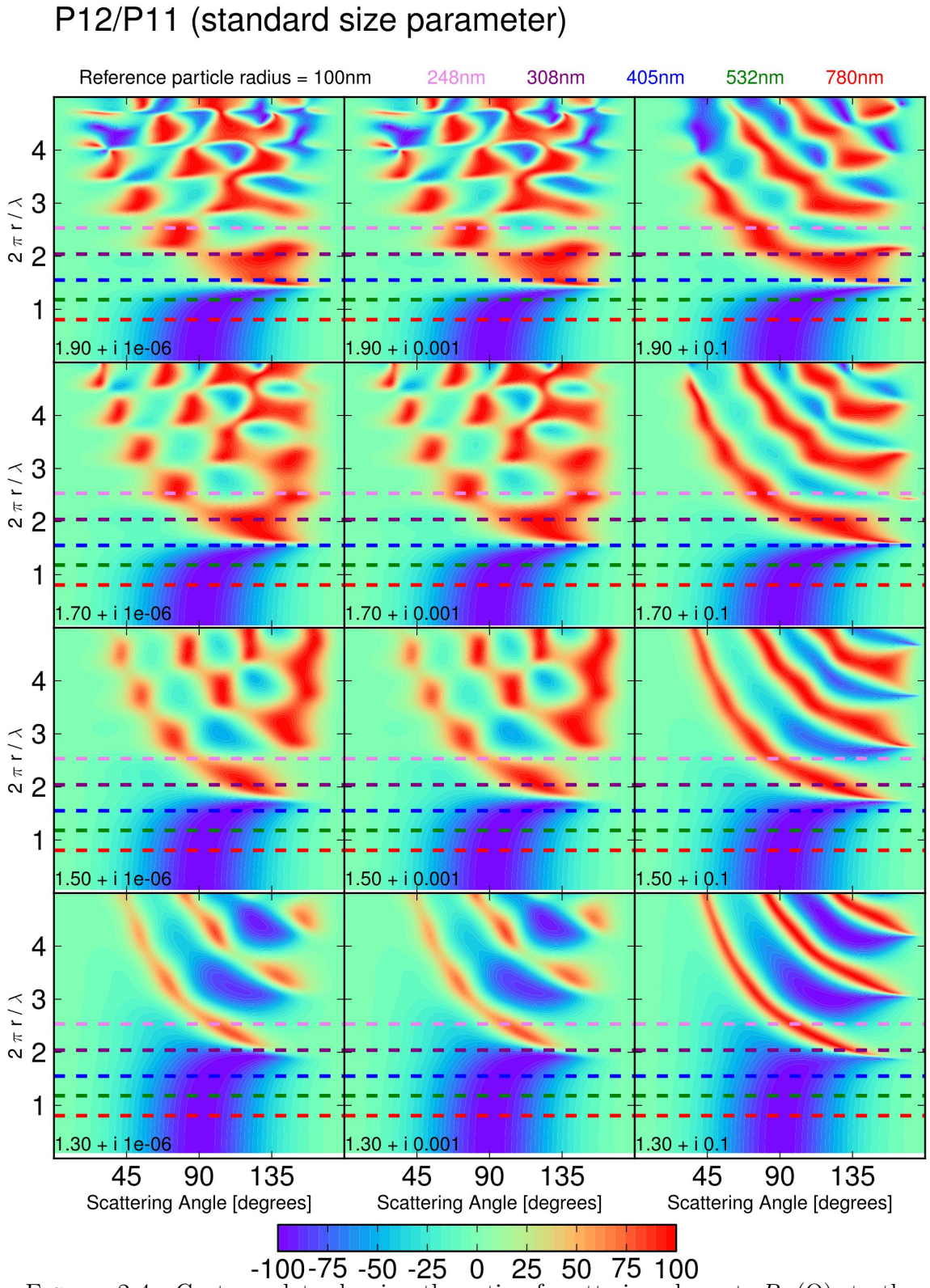

FIGURE 2.4: Contour plots showing the ratio of scattering element, $P_{12}(\Theta)$, to the phase function element, $P_{11}(\Theta)$. The horizontal axes show the scattering angle and vertical axes show particle size parameter. Complex refractive index layout is identical to that used in Figure 2.2.

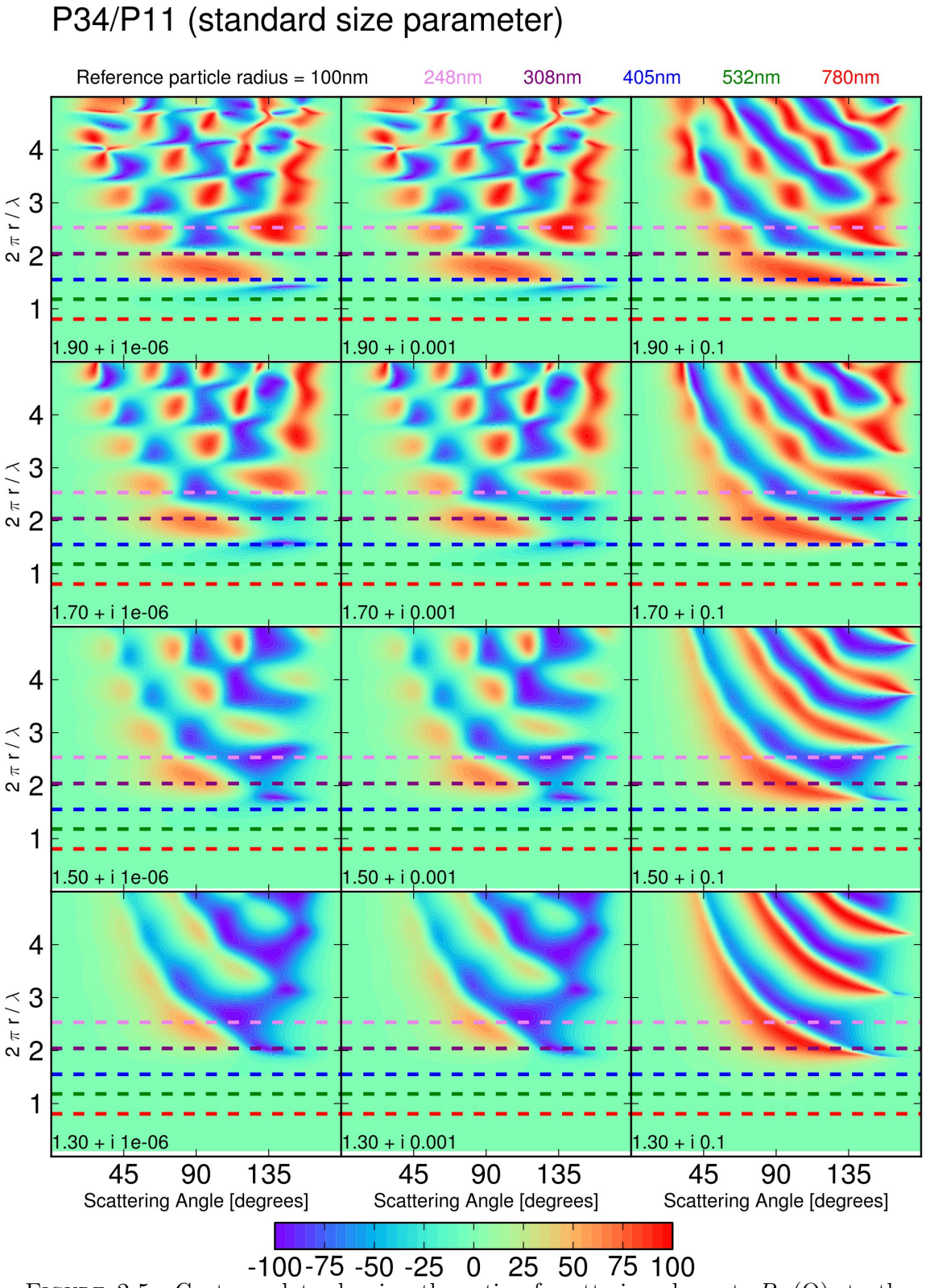

FIGURE 2.5: Contour plots showing the ratio of scattering element, $P_{34}(\Theta)$, to the phase function element, $P_{11}(\Theta)$. The horizontal axes show the scattering angle and vertical axes show particle size parameter. Complex refractive index layout is identical to that used in Figure 2.2.

as functions of the complex refractive index. As such, we may rule out the use of scattering matrix elements to resolve, for example, the complex refractive index very small particles. Likewise, measurements of these profiles will be insensitive to slight variations in the size distribution of very small particles.

Larger particles, with size parameters greater than two, exhibit scattering profiles that are much different from the Rayleigh scattering of molecules. Furthermore, the profiles change as real refractive index is increased from the bottom to top rows. By comparing calculations for different values of real and imaginary refractive index, the angular profiles appear to provide rich and informative scattering behavior. Subject to a more detailed analysis in Chapter 3, the profiles show a dependence on particle size and complex refractive index that may be used to constrain these properties of airborne particles. There is also clear evidence in these figures that using shorter wavelengths of light will resolve smaller particles. To visualize the benefits of measuring shorter wavelengths, we have drawn dotted lines to indicate the size parameter of particles with radius, $r = 100$nm, and have done so for several different wavelengths in the ultra-violet and visible regions of the spectrum. While the ultra-violet regions look promising for retrieving small particles, the benefits may be offset by increased scattering and absorption by molecules.

In summary of the single-scattering properties, we recall that they define a model for how light energy interacts with material in the atmosphere and on the surface. By showing Lorenz-Mie scattering calculations we have described the transition of scattering properties out of the Rayleigh regime of small particles. Maximal scattering efficiency

occurs for particles with size, r, and real refractive index, m_r, on the resonance interval:

$$2 \leq \frac{4\pi r(m_r - 1)}{\lambda} \leq 7. \tag{2.28}$$

This interval will be used to interpret results in Chapter 3 where smaller particles are shown to be unconstrained by single-scattering measurements, but resonating particles are constrained quite well by single-scattering measurements. A population of airborne particles with sizes large enough to resonate with the measured wavelength of light will contribute scattering signal in proportion to their geometric crossection. While small particles scatter much less efficiently than large particles, we noted that absorption remains proportional to the total mass-concentration of particles. For the purpose of characterizing populations of particles which are large enough to resonate, the angular profiles of scattering matrix elements appear to exhibit strong dependence on particles size and complex refractive index. As with the scattering efficiency, however, the angular profiles of small particles appear to present less information than angular profiles of larger have. All profiles converge to Rayleigh scattering. This leads us to expect that the properties of small particles will be difficult or impossible to characterize, but motivates a careful analysis of the information content of measurements of the single-scattering properties. This is the objective of work presented in Chapter 3, where we seek to determine how much information about the size and complex refractive index of a population of airborne particles can be inferred from measurements of their single-scattering properties.

2.2 Model for atmospheric remote sensing

The 3D VRTE is a tool for modeling polarimetric measurements of the atmosphere, where the effects of multiple scattering can be significant. The atmosphere and surface of the Earth are illuminated by sunlight and they absorb and scatter this incoming solar energy. This process gives rise to measurable radiative effects that contain information about the composition of the Earth's surface and atmosphere. The forward model may be defined, in general terms, as a function for computing a vector of measurements from a vector of unknown parameters. Suppose we have M measurements stored in the vector, $\hat{\boldsymbol{y}} = (\hat{y}^m)$ for $0 \leq m < M$, and that these each correspond to the polarimetric reading of a single pixel on a ground, air, or space borne sensor. From these data, we seek to determine N unknown parameters, stored in the vector, $\boldsymbol{a} = (a^n)$ for $0 \leq n < N$, where these define a three-dimensional distribution of cloud, aerosol, and surface properties. Using the parametrization of single-scattering properties in terms of particle properties, from Section 2.1, the polarimetric measurements of atmospheric radiation are modeled as functions of cloud, aerosol, and surface properties.

First, the values of the volume-extinction coefficient, $\sigma(\boldsymbol{x}; \boldsymbol{a})$ and the volume-scattering matrix, $\boldsymbol{Z}(\boldsymbol{x}, \boldsymbol{v}, \boldsymbol{v}'; \boldsymbol{a})$ are written explicitly as smooth functions of the vector of parameters, $\boldsymbol{a}$. They must be smooth to guarantee the existence of derivatives, $\partial\sigma/\partial a^n$ and $\partial\boldsymbol{Z}/\partial a^n$. Second, the VRTE is used to solve for the multiple scattering of incoming solar radiation and determine the Stokes vector solution, $\boldsymbol{u}(\boldsymbol{x}, \boldsymbol{v}; \boldsymbol{a})$. For any atmospheric state, $\boldsymbol{a}$, a solver for the VRTE can be represented as a linear operator, $\mathcal{U}_{\boldsymbol{a}}$, which acts

on the specified light source, $\boldsymbol{f}_{\odot}(\boldsymbol{x}, \boldsymbol{v})$, and returns the Stokes vector solution, $\boldsymbol{u}(\boldsymbol{x}, \boldsymbol{v})$:

$$\boldsymbol{u} = \mathcal{U}_{\boldsymbol{a}}[\, \boldsymbol{f}_{\odot}\,]. \tag{2.29}$$

In the third and last step, we write the measurable quantities which correspond to elements of the data vector, $\hat{\boldsymbol{y}}$, as inner products of the solution, $\boldsymbol{u}(\boldsymbol{x}, \boldsymbol{v})$, with a polarimetric-analyzer response function, $\boldsymbol{p}^{m}_{\odot}(\boldsymbol{x}, \boldsymbol{v})$:

$$y^{m}(\boldsymbol{a}) = \left\langle \boldsymbol{p}^{m}_{\odot}, \boldsymbol{u} \right\rangle, \tag{2.30}$$

for each measurement, $0 \leq m < M$. Given the clear apertures of typical Earth observing instruments we note that the polarization analyzers will be effectively Dirac-delta distributions in the location variable with angular integrations being determined by the field of view of the given sensor or pixel. The forward model is therefore a composition of operations for computing the single-scattering properties of particles followed by operations for computing the multiple-scattering measurements that correspond to the spatially variable single-scattering properties. This procedure provides the forward model which links observations to the 3D distribution of clouds and aerosols in the atmosphere.

2.3 Inverse problem and statistical optimization

It is possible to measure either single-scattering or multiple-scattering properties, and there are important applications of both techniques. In the case of single-scattering measurements, the forward model is developed directly from the calculations introduced in Section 2.1. Multiple-scattering measurements of the atmosphere require, in addition to these single-scattering calculations, a radiative transfer solver as described using general formula in Section 2.2. In either case, we model scattering measurements as a function of the properties of airborne particles of interest, and the framework of statistical optimization provides a means of estimating these properties and quantifying their uncertainty.

The physical relationship between the unknown parameter vector, $\boldsymbol{a}$, and the measurement vector, $\hat{\boldsymbol{y}}$, is written using the notation, $\boldsymbol{y}(\boldsymbol{a})$, for both single-scattering and multiple-scattering measurements. Statistical optimization is based on a measurement model that includes a model for noise, and we will assume Gaussian random noise throughout this thesis. The error in the measurement vector is modeled as a random variable that follows a multi-variate Normal distribution, $\boldsymbol{\epsilon} \sim \text{Normal}\ (\mathbf{0}, \boldsymbol{S}_{\boldsymbol{\epsilon}})$, with mean zero and covariance matrix, $\boldsymbol{S}_{\boldsymbol{\epsilon}}$. The measurement model is therefore written as follows:

$$\hat{\boldsymbol{y}} = \boldsymbol{y}\left(\boldsymbol{x}\right) + \boldsymbol{\epsilon}. \tag{2.31}$$

Non-linear least squares fitting is used to select the particle microphysical state that agrees best with data in the sense that it maximizes the likelihood of measuring the

observed data. This maximum likelihood estimate is equivalent to the minimization of the data objective function,

$$\Phi_{\text{data}}(\boldsymbol{a}) = \frac{1}{2}\ (\hat{\boldsymbol{y}} - \boldsymbol{y}(\boldsymbol{a}))^T\ \boldsymbol{S}_{\boldsymbol{\epsilon}}^{-1}\ (\hat{\boldsymbol{y}} - \boldsymbol{y}(\boldsymbol{a}))\,. \tag{2.32}$$

Additional constraints can be added by imposing pseudo-measurement constraints in a manner similar to [36] using a prior objective function,

$$\Phi_{\text{prior}}(\boldsymbol{a}) = \frac{1}{2}\,\boldsymbol{h}(\boldsymbol{a})^T\ \boldsymbol{S}_{\boldsymbol{h}}^{-1}\,\boldsymbol{h}(\boldsymbol{a})\,. \tag{2.33}$$

This expression allows the values of functions acting on microphysical parameters to be constrained using Gaussian priors with covariance matrix $\boldsymbol{S}_{\boldsymbol{h}}$. Such constraints include positivity of loading, variability of refractive index, and smoothness and normalization of size distribution. Within this framework, we carry out local uncertainty analysis, synthetic retrievals, and error characterization.

Chapter 3

Particle characterization

This chapter focuses on the sensitivity of single-scattering measurements to aerosol microphysical properties, like size distribution and complex refractive index. We present a theoretical study which analyzes several hypothetical sets of single-scattering measurements at three visible wavelengths: 405, 532, and 780nm. Full data includes all angularly dependent scattering-matrix elements and both the volume-scattering and volume-absorption coefficients. Information content and microphysical parameter resolution is computed for full data and for several incomplete data subsets. Comparing resolution for these measurement sets allows us to quantify, for instance, the importance of polarization for resolving the size-distribution and complex refractive index and the importance of volume-coefficients for resolving concentration and complex refractive index. The following results about the sensitivity of single-scattering measurements to aerosol properties

will be discussed: (1) Although even the phase-function alone offers reasonable constraints on the size distribution for larger particles, all single-scattering measurements fail to constrain the size distribution for very-small particles. (2) Uncertainty estimates for particle number concentration are much worse than for other loading parameters, like particle surface-area concentration and particle volume and mass concentration. (3) Polarimetric measurements improve retrieval uncertainty estimates in the size distribution and complex refractive index for larger particles. (4) Measuring the absorption coefficient becomes increasingly important for determining the complex refractive index of smaller particles as their scattering behavior approaches the Rayleigh limit. While these results apply to single-scattering measurements only, they may provide useful intuition about satellite and aircraft retrievals of aerosols in the atmosphere.

3.1 Objectives

Existing remote sensing techniques can sample large regions of the atmosphere and enable monitoring on a global scale through the use of satellite, airborne, and ground based sensors. A difficulty in interpreting such measurements is that they depend on scattering in large volumes of the atmosphere, which contain airborne particle populations with significant spatial variability. Another difficulty is that multiple scattering and radiative smoothing reduce the amount of local information that is available for retrieving particle microphysical properties [32, 37, 38]. An alternative and complementary approach involves the measurement of single-scattering properties using "local" techniques, which

exchange the vast spatial coverage of remote sensing for increased optical information. These instruments, called nephelometers, are designed to minimize multiple scattering and spatial variation, thereby enabling the retrieval algorithm to focus entirely on retrieving the microphysical properties of the aerosols. This leads to many more independent scattering measurements (per microphysical retrieval) than is possible using remote sensing of the atmosphere [39].

Observation systems for estimating the microphysical properties of atmospheric aerosol particles have been developed for various instruments since the 1970's [29, 40–44], with each of these instruments measuring some of the single-scattering properties of aerosols. More recent nephelometers are capable of measuring any of the single-scattering properties of aerosol particles at multiple visible wavelengths [28, 31, 45–49]. Modern laboratory instruments are capable of measuring (or estimating) all of the single-scattering properties introduces in Chapter 2 at visible wavelengths [28, 46–48], and an airborne instrument is being developed to measure a limited set of polarimetric single-scattering properties and help validate aerosol retrievals based on remote sensing [31]. Taking appropriate combinations of these instruments offers the potential for measurements of the theoretical maximum of information contained in the single-scattering far field of visible light, and this rich dataset provides a unique tool for studying the microphysical properties of airborne particles in a population.

However, the theoretical models used to analyze these measurements were rather simplistic, and discrepancies in instrumentation and modeling approaches have obscured notions of which microphysical properties can be resolved by measurements and which cannot.

A few examples of microphysical targets which are of great interest but need further study include the number concentration of CCN, the spectral signature in the complex refractive indices for bimodal aerosol populations (with coarse and fine modes), and the mixing fractions of different types of similarly sized particles based on differences in their refractive indices. If these targets can be resolved, then a careful analysis is needed to determine which single-scattering measurements must be made as well as the required accuracy of those measurements. This kind of information is very useful for guiding the design and optimization of new instruments. Our work aims to address these questions in a systematic way for the characterization of spherical aerosols using measurements of single scattering in the visible spectrum.

We also seek to develop retrieval algorithms which are applicable to a general class of observation systems that combine data from modern nephelometry instruments. These optical measurements include the spectrally dependent volume-scattering and volume-absorption coefficients, σ_{sca} and σ_{abs}, along with the angularly dependent elements of the Stokes scattering matrix, which fully characterizes the radiative properties of a population of aerosol particles in a small volume of the atmosphere [33, 38]. The specific microphysical parameters used here include the concentration of particle geometric crossection, the normalized size distribution, and the spectrally dependent complex refractive index. Although similar to previous microphysical parametrizations in many regards, our strategy of parameterizing particles by type facilitates the inclusion of prior constraints and permits the modeling of more diverse populations of externally mixed spherical particles that may have similar sizes but different compositions [8, 50, 51].

In lieu of experimental data, we substitute synthetic data generated by known particle populations with random measurement errors that are consistent with those found in existing instruments. Given realistic assumptions about the measurement system and prior assumptions on particle microphysics, we then discuss the certainty with which microphysical targets of interest can be estimated. We consider six idealized measurement sets, each of which is analogous to a combination of data taken by the following groups [28, 31, 46–48]. Each measurement set is subject to the same stability analysis to isolate the effects of data set choice and permit an inter-comparison of the theoretical expectations for the retrieval capabilities associated with each measurement set for a given type of particle. The stability analysis is repeated for several common particle types. In each we compare the information content and posterior uncertainties for all six measurement sets, and present synthetic retrievals for the full single-scattering measurements. This stability analysis draws on methods from previous work [8, 26, 50–53], with the goal of determining realistic expectations for particle retrievals and the theoretical capabilities (and limitations) inherent to spherical particle characterization by visible single scattering measurements. See Appendix B for a complete description of computational details.

3.2 Aerosols, measurements and methods

Water droplets are abundant in the atmosphere and are composed of pure water in liquid water clouds and of salt water in sea spray. In the case of sea spray, the particles are generated at the surface of the ocean by wind and are often observed, for example, by

the AERONET monitoring station in Lanai Hawaii [30]. Sea spray has a real refractive index that is slightly larger than that of pure water, and both have negligible imaginary refractive index. Populations of these aerosols have spherical particles with radii as large ten microns or so. The particle microphysical parameters that define each type of particle are shown in Figure 3.1 along with their corresponding single-scattering properties. The prior size distribution is plotted as a normalized probability distribution of geometric crossection density over the natural log of particle radius, $\log(r)$:

$$\frac{dS_j(r)}{d\log r} = \pi r^3 \sum_{k=0}^{K_j-1} p_j^k \varphi_{jk}(r)\,. \tag{3.1}$$

The set of basis functions, φ_{jk}, are smooth polynomial "bumps" and are plotted in Figures 3.1 and 3.2. For pure water and sea spray the size distribution is compactly supported on the interval of particle radii between $r_{\min} = .01\mu$m and $r_{\max} = 15\mu$m. The particle types differ in real refractive index, with sea spray having a slightly larger and more variable real refractive index than liquid water clouds.

In addition to these populations, two kinds of smaller aerosols are considered: sulfate and tarballs. Sulfate aerosols are found most often as a solute or precipitate in liquid droplets and impact global climate with a relative cooling of -0.4 Wm^{-2} [1]. Most sulfate in the atmosphere results from fossil fuel combustion (72%), but other significant sources include marine phytoplankton (19%), volcanic eruptions (7%), and biomass burning (2%)[1]. Sulfate is non-absorbing at visible wavelengths and has a negligable imaginary refractive index. This is very different from tarballs which are generated by

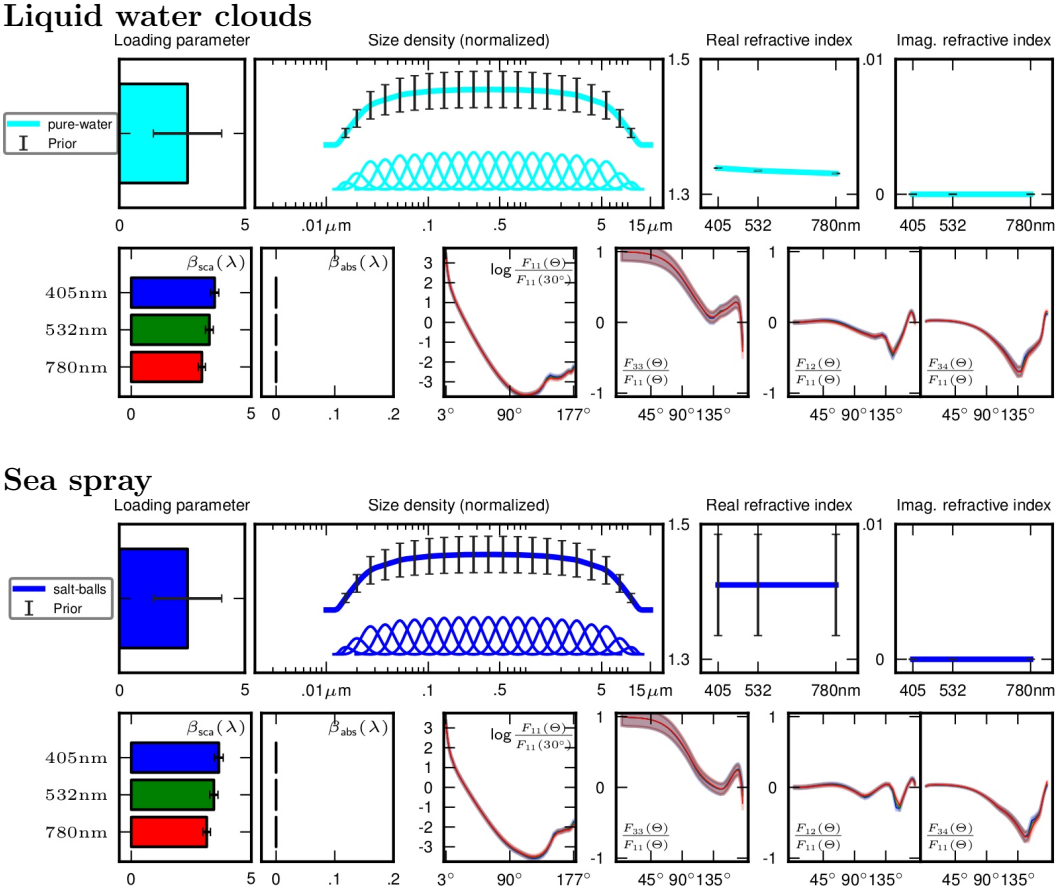

FIGURE 3.1: The microphysical parameterization and single-scattering properties of water droplets and sea spray. For each of these types of aerosols there are two rows of plots, showing the following quantities from left to right. **Rows 1&3:** (1) The total concentration of particles, (2) the size distribution as a function of particle radius, as in Eq. 3.1 and the basis functions, φ_k functions plotted below, (3) real refractive index as a function of wavelength, and (4) imaginary refractive index as a function of wavelength. Error bars show the standard deviation of the prior distribution for each particle property about its mean value. **Rows 2&4:** (1) The volume-scattering coefficient for each wavelength, (2) the volume-absorption coefficient for each wavelength, and the angular profiles of scattering matrix elements (3) $F_{11}(\Theta)/F_{11}(30°)$, (4) $F_{33}(\Theta)/F_{11}(\Theta)$, (5) $F_{12}(\Theta)/F_{11}(\Theta)$, and (6) $F_{34}(\Theta)/F_{11}(\Theta)$. Measurement error is visualized using error bars for the volume-scattering and volume-absorption coefficients and using shaded regions around the angular profiles of scattering matrix elements.

some forest fires and contain light-absorbing carbon [54, 55]. Tarballs are also called brown carbon to distinguish them from soot, or black carbon which is also made in forest fires. Compared with soot, which has a large imaginary refractive index at all wavelengths [56], tarballs absorb less efficiently at red wavelengths. They have large values of imaginary refractive index at ultra-violet wavelengths which decrease toward longer red wavelengths. This spectral behavior in imaginary refractive index was observed in a laboratory setting for tarballs generated by burning moist plant material, e.g. tundra moss [47]. The set of basis functions that we use to represent the size distribution of sulfate and tarballs are identical, and both are compactly supported on the interval between $r_{\min} = .006\mu$m and $r_{\max} = 1.75\mu$m. The parametrizations of these two types of small particles are shown in Fig. 3.2, along with their single scattering properties.

In addition to populations with only one type of particle, we consider mixtures of two types of particles. This is done to test whether using different prior constraints on complex refractive index allows the retrieval of the particle properties of both modes — to classify both aerosols in the mixture. For example, we consider the retrieval of a mixture of sulfate and tarballs together. The prior for individual modes of sulfate and tarballs have identical size distributions and differ only in their complex refractive index. In this regard our approach differs from two conventional approaches: one approach uses a single spectrally dependent refractive index for all particles regarless of size [57], and another approach uses two spectrally independent refractive indices, one for small particles and one for large particles [58, 59]. Our approach uses mixtures of one or more types of aerosol, with each type representing a class of particles with an approximatly-known size

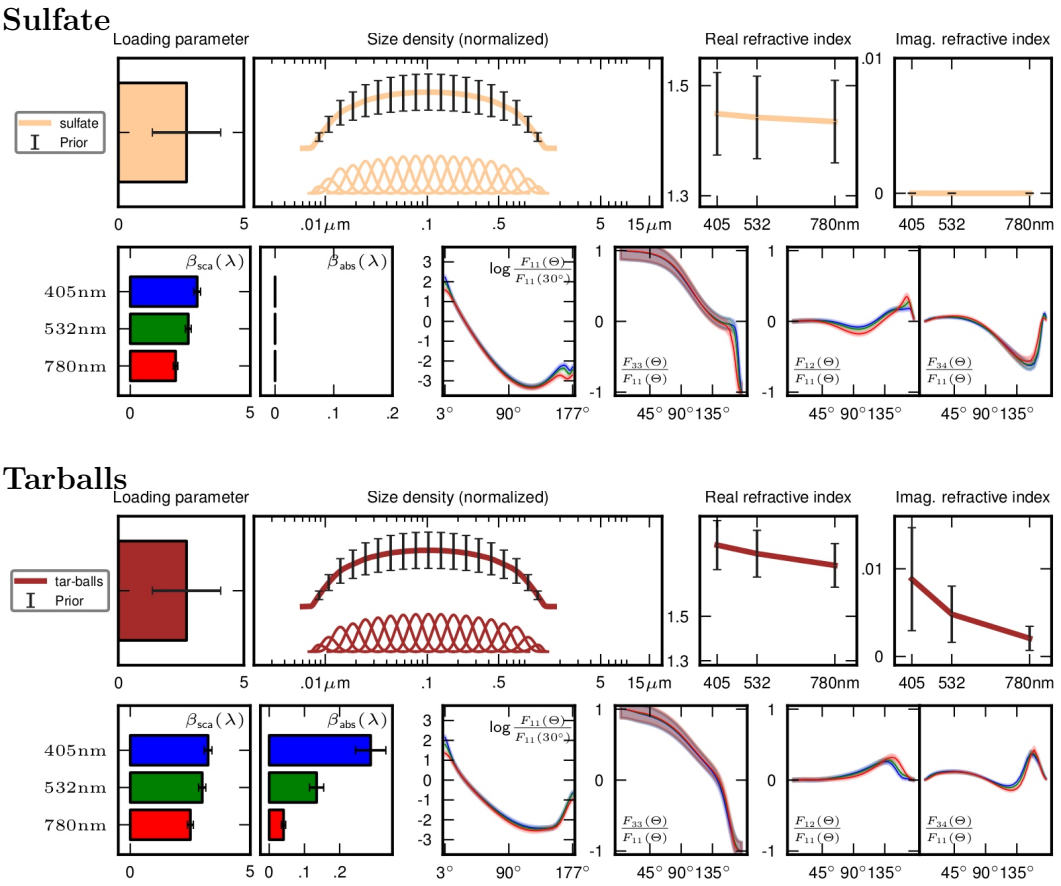

FIGURE 3.2: The microphysical parametrization of sulfate and tarballs and the single-scattering properties corresponding to the mean prior state. The layout is the same as in Fig. 3.1.

and complex refractive index. The approximate knownledge is defined by upper and lower bounds on particle size and by a Gaussian distribution over complex refractive index. The difference is subtle, but significant in that it permits retrievals and stability analyses for mixtures of two kinds of particles which have similar sizes but differences in their complex refractive index and composition.

One potential application for this increased flexibility would help understand how the various components of biomass burning smoke interact and evolve in the first twelve hours after combustion [4, 54, 55]. Such smoke plumes are hypothesized to include external

mixtures of sulfate, soot, and tarballs. All three types of particles are similarly sized but have distinct refractive indices, and in the case of soot distinct shape. Tar balls have been created in laboratory settings and characterized by approaches which combine particle impactor determined size distribution and photo acoustic integrating nephelometer measurements [46, 47]. By replacing the sparse sampling of size distribution by the impactor, with continual measurements of the scattering matrix elements [48], our use of a mode based parameterization may permit the retrieval of the particle microphyscis of sulfate, tar balls, and soot as these components of the smoke evolve in time. Such a time-dependent retrieval of particle properties could test a hypothesis made by [54, 55]: that sulfate aerosols absorb enough water-vapor from the initially humid environment so as to cause tarballs lose water and become smaller and more concentrated. Excluding soot, which is not yet in the scope of our lookup tables, we consider a mixture of sulfate and tarballs to assess the extent to which their different refractive indices enable simultaneous retrievals of both sets of microphysical parameters. The parameterization for this mixture of sulfate and tarballs is shown in Figure 3.3 along with their combined single-scattering properties.

The other application is motivated by retrievals biomass burning aerosol by AERONET stations in Africa [30], which assumed that aerosols populations were present with only a single complex refractive index (possibly spectrally dependent). The retreivals of African savanna aerosol show two distinct size modes but only a single complex refractive index. Hypothesizing that the large mode is an accumulation mode of mostly water and that the small mode is an Atkins mode of LAC, the retrieved refractive index of $(1.51 + \mathrm{i}0.021)$

Mixture of sulfate and tarballs

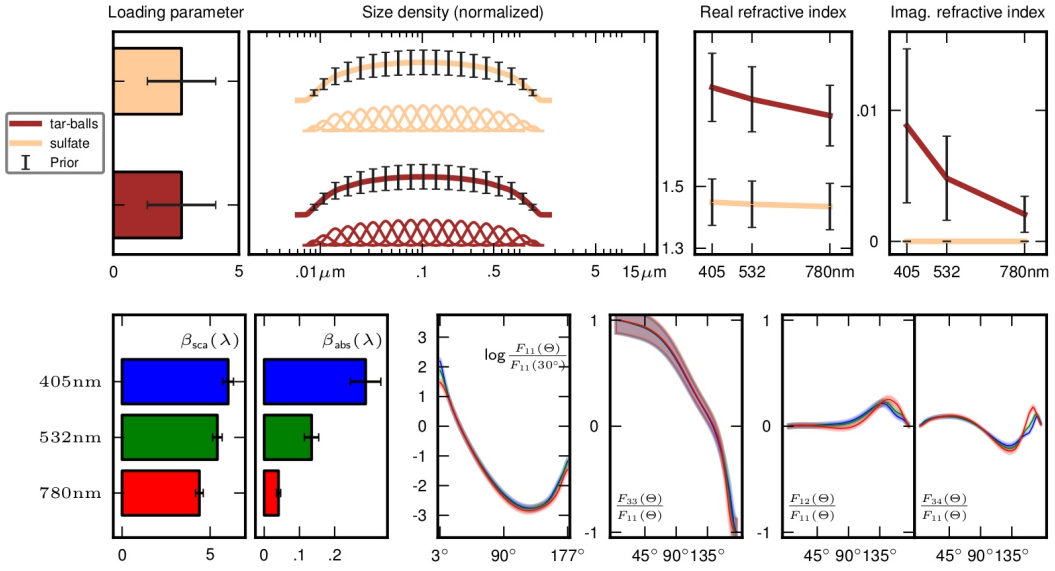

FIGURE 3.3: An aerosol mixture of sulfate and tarballs that contains equals geometric crossections of each type. The layout of particle parameters and single-scattering properties is the same as in Figure 3.1.

might be interpreted as an "effective" refractive index. Concern over the effects of such assumptions motivates simultanious retrievals of sea spray and tarballs. Parameters for externally mixed tarballs and sea spray are shown in Figure 3.4 along with their single-scattering properties.

These particle populations are analyzed in Section 3.3 to determine the degree to which single-scattering measurements can characterize them. This is done using a linear stability analysis (based on Baysian inference) and a synthetic retrieval study, in which we retrieve aerosol properties from artificial data with random noise. The details are presented in Appendix B, but a brief overview of our approach will suffice for the interpretation of

Mixture of Sea spray and tarballs

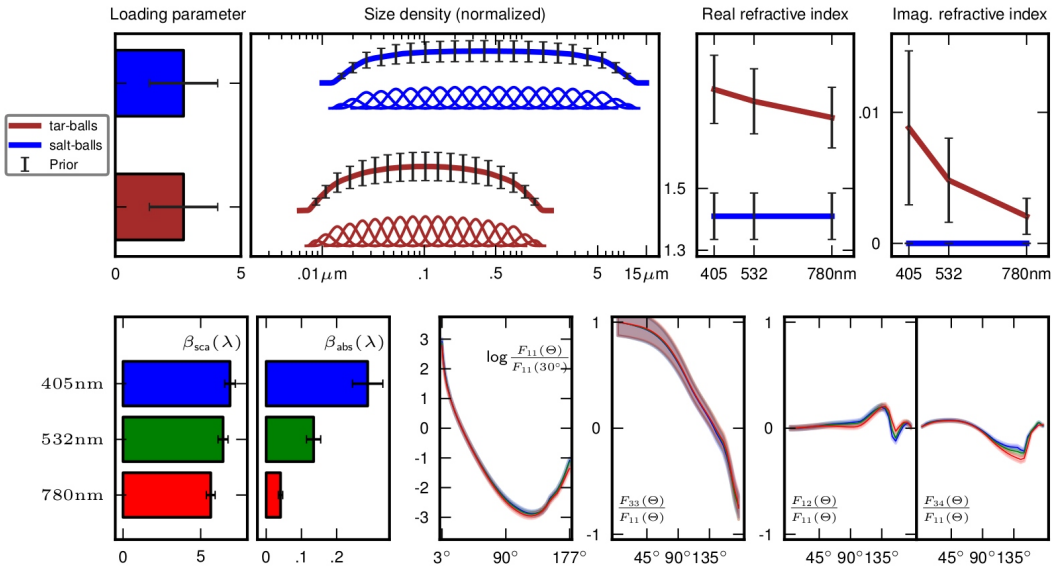

FIGURE 3.4: An aerosol mixture of sea spray and tarballs that contains equals geometric crossections of each type. The layout of particle parameters and single-scattering properties is the same as in Figure 3.1.

results. We seek to quantify the information content of full measurements of the single-scattering properties and of incomplete subsets of full measurements. Six sets of single-scattering measurements are considered. Though the sets are theoretical constructs, they are consistent with existing instruments [46–48]. There are three measurement subsets for the angular profiles of the scattering-matrix elements. The most basic set of measurements are called the *phase-profile* measurements,

$$\log\left(\frac{F_{11}(\Theta)}{F_{11}(30^\circ)}\right). \tag{3.2}$$

Then we add polarimetric constraints to obtain the *linear-profile* measurement set by including the ratio,

$$\frac{F_{12}(\Theta)}{F_{11}(\Theta)}, \tag{3.3}$$

and the *full-profile* measurement set by include the remaining two ratios,

$$\frac{F_{33}(\Theta)}{F_{11}(\Theta)} \quad \text{and} \quad \frac{F_{34}(\Theta)}{F_{11}(\Theta)}. \tag{3.4}$$

This gives three subsets of full measurements of the single-scattering properties. Each set includes three visible wavelengths and 51 scattering angles. Since we are interested also in studying the information in the volume-scattering and volume-absorption coefficients, we repeat the linear stability analyses with and without these *volume-coefficient* measurements. So, in total there are six subsets of measurements and six populations of aerosols, and an analysis is done for each combination. We chose to use relative error for both the volume-scattering coefficient (15%) and volume-absorption coefficient (5%) to match the values given by the group which makes these measurements [46].

Each analysis begins by linearizing the forward model about the mean prior state to create an approximate linear model which is amenable to Bayesian error estimation techniques. Using the approximate linear forward model with assumptions of a Gaussian prior and a Gaussian measurement error distribution, the posterior distribution is guaranteed to be Gaussian as well [26, 60]. Computation of the prior and posterior uncertainty covariance matrices is done using Eqs. (A.29) and (A.66). The model is linearized about the mean

prior state $\boldsymbol{x}_{\text{prior}}$ in order to analyze the information in posterior parameter covariance matrix $\boldsymbol{S}_{\text{post}}(\boldsymbol{x}_{\text{prior}})$, relative to the information in the prior covariance matrix $\boldsymbol{S}_{\text{prior}}(\boldsymbol{x}_{\text{prior}})$. These parameter uncertainty covariance matrices are computed for each of the measurement sets and used to quantify the information content of noisy measurements. Following the linear stability analysis of each type of aerosol, we show synthetic retrievals to support the conclusions drawn from the linearization approach. These synthetic retrievals also varify our retrieval methodology as presented in Appendix A.4 and show that retrievals of many important aerosol properties are stable with respect to measurement noise.

3.3 Stability analysis results

This section presents results about how well various subsets of complete single-scattering measurements can resolve the aerosol properties of the populations introduced in Section 3.2. In summary, visible light scattering measurements resolve the particle size distribution (geometric cross-section density function) for particles with radius larger than 100nm, but are relatively insensitive to smaller particles. Polarimetric measurements reduce the uncertainty in the size distribution relative to measurements of the phase function alone. Measurement sets which include the volume-scattering and volume-absorption coefficients can resolve certain measures of particle concentration but not others. The volume and mass concentrations are resolved to 3-5% relative uncertainty, the geometric crossection and surface-area concentration are resolved to between 5-15% relative uncertainty,

and the number concentration is resolved to between 22-26% relative uncertainty. Estimates of cloud condensation nuclei are resolved to between 11-21% relative uncertainty. In addition to enabling the retrieval of particle concentration, the measurements of the volume-scattering and volume-absorption coefficients also improve resolution for the spectrally dependent complex refractive index. Lastly, we consider the retrieval of external mixtures, including tarballs mixed with sulfate and tarballs mixed with sea spray, and we show evidence that visible light scattering measurements may be capable of discriminating between similarly sized particle with different composition, i.e. complex refractive index.

3.3.1 Pure water

The linear stability analysis of pure water is shown Tables 3.1 and 3.2 and in Figure 3.5 for all measurement sets, and synthetic retrievals are shown in Figure 3.6. Real and imaginary refractive indices are constrained tighly to their well-known values in nature.

The Shannon information content and resolved degrees of fredom in Table 3.1 quantify the magnitude of the constraints on microphysical properties resulting from each of the measurement sets. There are about 6 bits of information on the concentration of water droplets for measurement sets which include volume-absorption and volume-scattering coefficients, and is independent of which set of scattering profiles are measured. However, information on the size distribution does increase with the addition of polarimetric measurements. The phase-profile measurements provide 46 bits of information and this

number increases to 51 bits for linear-profile measurements and 89 bits for full-profile measurements. Information for real and imaginary refractive index is essentially zero, since these properties are constrained by the prior to their known values.

TABLE 3.1: Stability analysis of pure water: degrees of freedom and bits of information

			Information [bits]		
	d_{signal}	d_{prior}	Total	Concentration	Size
Phase-profile data	10.0	18.0	46	0	46
Phase with coeficients	11.3	16.7	55	6	46
Linear-profile data	10.8	17.2	51	0	51
Linear with coeficients	12.1	15.9	60	6	51
Full-profile data	13.2	14.8	89	0	89
Full with coeficients	14.5	13.5	97	6	89

In stability analysis plots from Figure 3.5, the prior and posterior error bars can be compared for all six measurements to see which parameters are resolved and how the resolution changes with increasingly rich data. The geometric crossection concentration is unconstrained without volume-coefficient measurements, and constrained equally well will any scattering-profile measurement. The uncertainty in the size distribution of larger particles is greatly reduced by all scattering-profile measurements, but particles which are smaller than the reasonance interval are unconstrained. The error paterns show a similar cutoff in resolution for the size distribution. The polarimetric constraints, in linear-profile and full-profile measurement sets, improve posterior constraints on the size distribution when compared with phase function only measurements.

Table 3.2 shows the relative uncertainties for several measures of particle concentration, including number, area and volume concentrations. Also, The relative uncertainty in CCN concnetration estimates are given which compute the uncertainty in number concentration

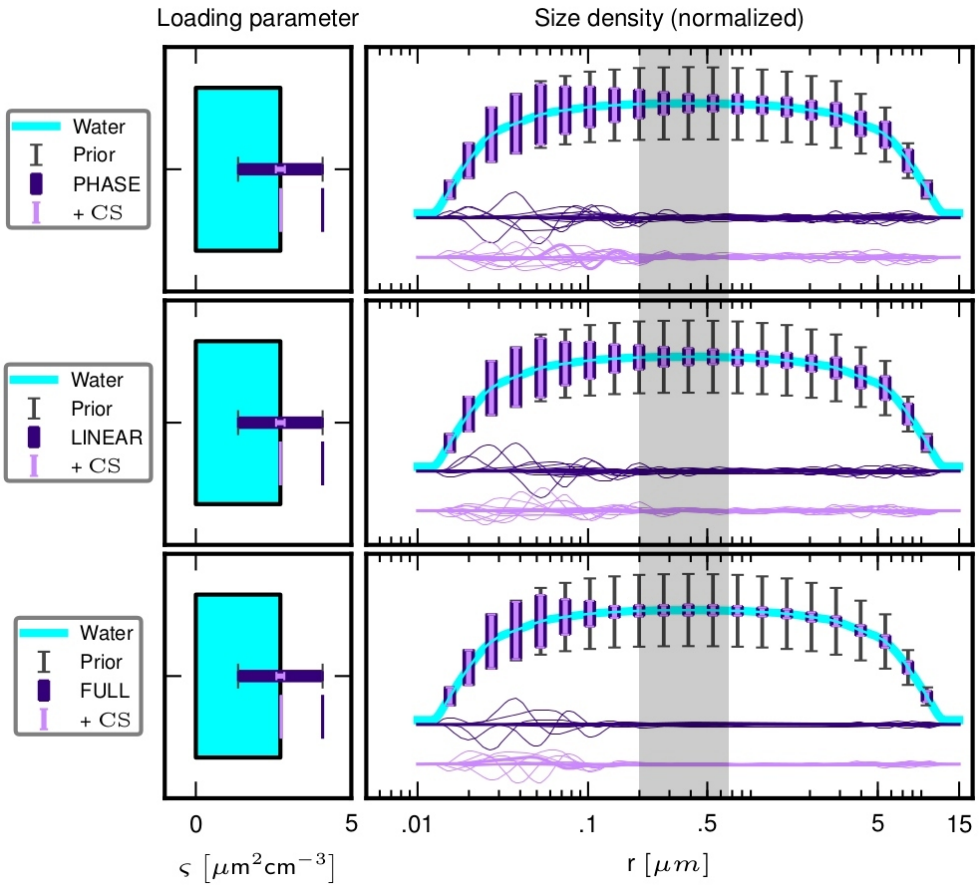

FIGURE 3.5: Water droplet prior and posterior uncertainty shown by error bars. Thin black error bars show prior uncertainty, purple error bars show posterior uncertainty without volume-coefficient measurements and pick error bars show posterior uncertainty with volume-coefficient measurements. Error patterns or principle components are plotted below the size distribution in each plot. Rows from top to bottom show increasing information. **Row 1:** Phase-profile measurements with and without volume coefficients. **Row 2:** Linear-profile measurements with and without volume coefficients. **Row 3:** Full-profile measurements with and without volume coefficients. The gray region shows resonating sizes at the shortest wavelength, $\lambda = 405$nm.

of particles larger then the specified radius. All concentrations for liquid water droplets have prior relative uncertainty between 50-54%. Volume (or equivilantly mass) concentration is resolved to 3% relative uncertainty, suface area concentration is resolved to 5% relative uncertainty, and number concentration is resolved to 23% relative uncertainty. Loading parameters were not resolved by measurement sets without volume-coefficient

constraints so these are excluded from the table. Uncertainty reduction is independent of which scattering-profile measurement set is used.

TABLE 3.2: Relative uncertainty in pure water concentration

	Concentration			CCN		
% Uncertainty	Number	Area	Volume	$r_{>31\text{nm}}$	$r_{>37\text{nm}}$	$r_{>43\text{nm}}$
Prior	54%	50%	52%	54%	54%	54%
Phase with coeficients	23%	5%	4%	22%	20%	18%
Linear with coeficients	23%	5%	4%	21%	19%	17%
Full with coeficients	23%	5%	3%	19%	16%	13%

The synthetic retrieval study for water droplets is shown in Figure 3.6 and uses the full set of scattering matrix measurements along with volume-scattering and volume absorption coefficients to constrain particle concentration and size distribution. The true microphysical state has a concentration that is slightly offset from the prior and a size distribution that wiggles above and below the prior. Seven samples of noisy synthetic data are generated for each true state and used according to the retrieval algorithm described in Appendix B. The retrieved loading parameters match the true loading for all samples of noise, and the retrieved size distributions match the true size distribution for particles which are large enough to reasonate with the observed wavelengths of light.

The case of liquid water droplets is easiest due to the known refractive index and dominant fraction of large particles. Measurements of the volume-scattering and volume-absorption coefficients are needed to retrieve concentration when measured along with the phase profile. Particle volume and surface area concentration are resolved well, but number concentration remains poorly constrained due to uncertainty in size distribution of the

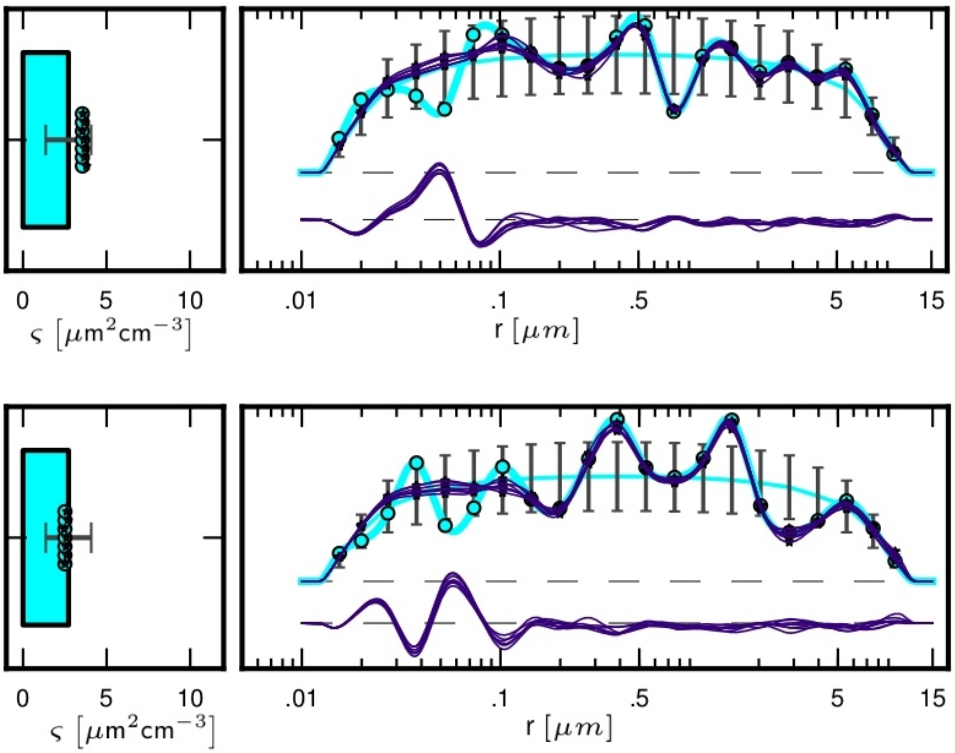

FIGURE 3.6: Synthetic retrievals of water droplets obtained by fitting full single-scattering measurements with random noise. Each row shows a randomly generated true state, selected to differ significantly from the mean. The true concentration is plotted as colored circles and the true size distribution is plotted as a colored line connecting colored circles. Retrievals are plotted with purple lines, and each corresponds to one of seven random samples of measurement error.

smallest particles. The size distribution of larger particles is resolved well with phase-profile measurements alone, and resolution improves when polarimetric constraints are added. All measurement sets fail to constrain the size distribution of particles with radius below the reasonance interval.

3.3.2 Sea spray

The linear stability analysis of sea spray is shown in Tables 3.3 and 3.4 and in Figure 3.7 for all measurement sets. A synthetic retrieval study is shown in Figure 3.8. The

prior distribution for the sea spray aerosol is the same as that for pure water with regards to the concentration and size distribution. However, the prior distribution of sea spray allows much more variability in real refractive index. The standard deviation is choosen to be consistent with the real refractive index of hydrated salt droplets when they are subjected to a range of relative humidities, 40-100% [61].

Table 3.3 shows the general results of the linear stability analysis in terms of the number of degrees of freedom resolved by measurement and prior, and the information content for various subsets of the unknown parameters. Measurements of the volume-scattering and volume-absorption coefficients provide 6-7 bits of information for particle concentration and also provide 7-9 bits of information for the imaginary refractive index. The scattering-profile measurements provide 45-94 bits of information for the size distribution and 19-29 bits of information for the real refractive index, but they add little information for the loading and imaginary refractive index.

TABLE 3.3: Stability analysis for sea spray: degrees of freedom and bits of information.

			Information [bits]				
	d_{signal}	d_{prior}	Total	Concentration	Size	Real	Imaginary
Phase-profile data	13.2	14.8	66.9	0.0	44.5	19.5	0.0
Phase with coef.	16.6	11.4	85.0	6.4	44.8	19.9	7.5
Linear-profile data	14.1	13.9	75.0	0.0	51.7	21.5	0.0
Linear with coef.	17.7	10.3	92.9	6.6	51.8	21.8	8.0
Full-profile data	16.7	11.3	123.2	0.0	94.0	28.5	0.0
Full with coef.	20.3	7.7	140.9	6.9	94.0	28.6	8.9

The stability analyses for sea spray is visualized in Figure 3.7. The concentration is unconstrained without volume-coefficient measurements and constrained equally well by any set of scattering-profile measurements. The size distribution of particles which are large

enough to reasonate with the measured wavelengths of light show posterior uncertainty estimates that are much smaller than those of the prior. Error paterns show a similar cutoff in resolution for the size distribution. This suggests that measurements of the phase function alone may be adiquate for retrieving the real refractive index of sea spray. Still, there is noticable benefit to makeing measurements of polarization, as can be seen by comparing uncertainties in the size distribution for phase-profile measurements with those of the linear-profile and full-profile measurements. All measurement sets constrain the posterior error bars for real refractive index.

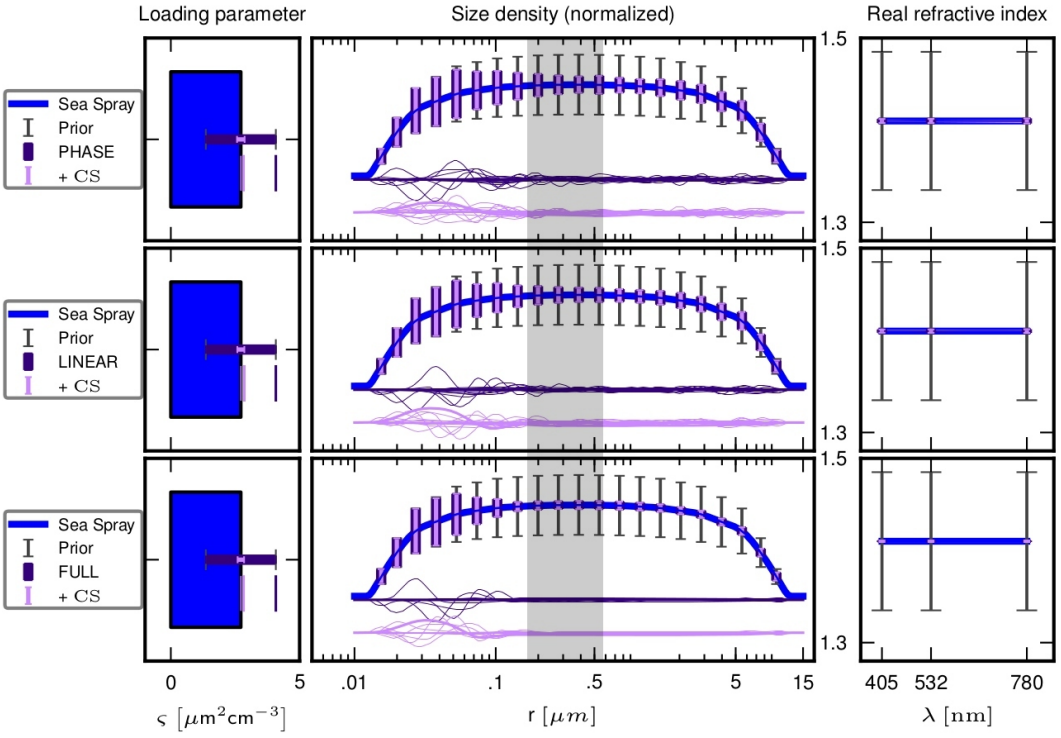

FIGURE 3.7: Sea spray prior and posterior uncertainty for concentration, size distribution and real refractive index. Descending rows have increasing measurements as in Figure 3.5, with purple lines and error bars corresponding to cases without volume-coefficient measurements and pink lines and error bars corresponding to cases with volume-coefficient measurements. The gray region shows resonating sizes at the shortest wavelength, $\lambda = 405$nm.

Shown in Table 3.4, the relative uncertainty in the concentration of sea spray has a

baseline of 50-54%, which is the prior uncertainty in concentration. In the posterior distributions, the volume concentration has 3-4% relative uncertainty, the suface area concentration has 5% relative uncertainty, and number concentration has 22-23% relative uncertainty. Retrieving the volume and area concentrations seem possible with any measurement set provided that it includes the volume-scattering and volume-absorption coefficients. Relative uncertainty in the number concentration of CCN varies from 11-21% and depends on the radius at which particles become large enough to act as CCN. Since small particles are poorly constrained, the relative uncertainty in CCN concentration improves for larger radii. Here, also, we see lower relative uncertainty for polarimetric measurements, presumably because the linear-profile and full-profile measurements reduce the uncertainty in the particle size distribution, as can be seen in Figure 3.7.

Table 3.4: Relative uncertainty in sea spray concentration

	Concentration			CCN		
% Uncertainty	Number	Area	Volume	$r_{>31\text{nm}}$	$r_{>37\text{nm}}$	$r_{>43\text{nm}}$
Prior	54%	50%	52%	54%	54%	54%
Phase with coeficients	23%	5%	4%	21%	19%	17%
Linear with coeficients	23%	5%	4%	21%	18%	16%
Full with coeficients	22%	5%	3%	19%	15%	12%

Synthetic retrievals for sea spray are made using the complete set of scattering data and are shown in Figure 3.8. The true state was selected from random samples of the prior so as to differ considerably from the mean. Therefore the true state presents a challange to the retrieval algorithm, yet agrees with the prior constraints. For all seven samples of measurement noise the retrieved microphysical states are seen to match the concentration

and real refractive index quite well. The size distribution is retrieved for particles which are large enough to reasonate but not for smaller particles.

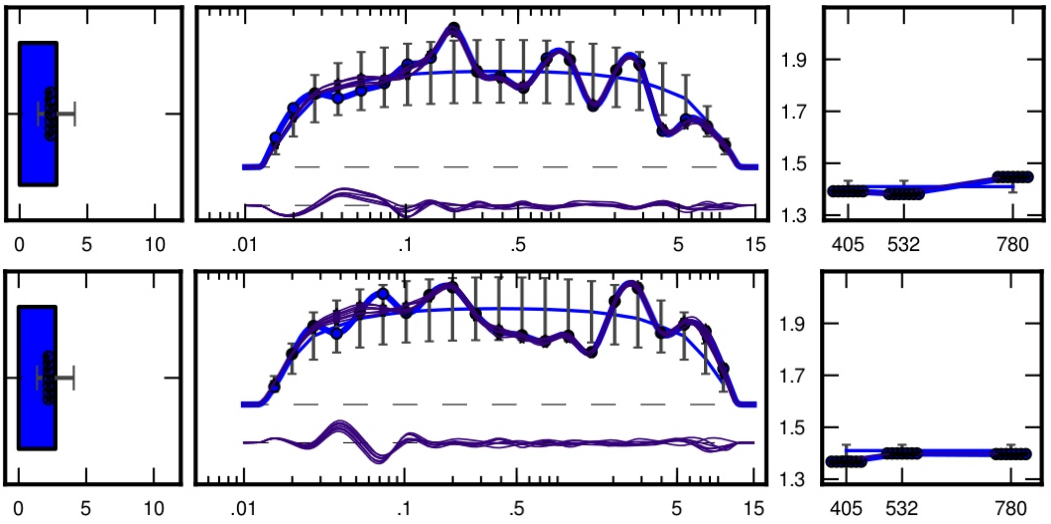

FIGURE 3.8: Synthetic retrievals of sea spray aerosols from full single-scattering measurements. The layout is similar to Figure 3.6 but including real refractive index, in the right-most column.

The case of sea spray aerosols introduced the challenge of a variable real refractive index. Measurements of the volume-scattering and volume-absorption coefficients are nessesary to constrain particle volume and area concentrations, and measurements of the phase profile are sufficient to make this possible. The measurements are only marginally sensitive to number concentration and CCN concentration. Measurements of the phase profile provide good constraints on reasonating portions of the size distribution and the spectrally dependent values of the real refractive index. The addition of polarimetric constraints reduces the uncertainty of both the size distribution and real refractive index. All measurement sets fail to constrain the size distribution particles which are too small to reasonate with the observed wavelengths of light. Synthetic retrievals are stable and

accurate for all microphysical properties, with the exception of the size distribution for small particles.

3.3.3 Sulfate

The linear stability analysis of sulfate aerosols is shown Tables 3.5 and 3.6 and in Figure 3.9, and synthetic retrievals are shown in Figure 3.10. Hydrated sulfate is a small, scattering aerosol and is modeled using a size distribution that is shifted toward smaller particles with radii on the interval, 0.006-1.75μm. The prior distribution of refractive index is consistent with the variability for ammonium sulfate in relative humidity 40-100% [61]. Real refractive index is larger and more variable than for water. The small size of sulfate aerosols leads to a substantial fraction of the geometric cross-section concentration coming from unresolved particles. While this may be undesirable in opperational retrievals, doing so in the stability analysis helps to provide insight into how the uncertainty in small particles may affect resolved parameters.

Table 3.5 shows the general results of the linear stability analysis. Measurements of the volume-scattering and volume-absorption coefficients profide 5-6 bits of information for particle concentration but provide less than 1 bit of information for the remaining unknown parameters. The profile measurements of the scattering matrix provide 45-94 bits of information for the size distribution and 19-29 bits of information for the real refractive index. The imaginary refractive index is constrained very tightly by the prior.

TABLE 3.5: Stability analysis for sulfate: degrees of freedom and bits of information

			Information [bits]				
	d_{signal}	d_{prior}	Total	Concentration	Size	Real	Imaginary
Phase-profile data	10.5	15.5	58.1	0.0	35.0	19.4	0.0
Phase with coef.	11.5	14.5	66.6	5.1	35.2	19.4	0.0
Linear-profile data	11.2	14.8	65.2	0.0	41.3	21.6	0.0
Linear with coef.	12.2	13.8	73.7	5.3	41.4	21.6	0.0
Full-profile data	12.7	13.3	101.7	0.0	71.4	28.9	0.0
Full with coef.	13.7	12.3	110.2	5.5	71.4	28.9	0.0

The stability analyses for sulfate aerosol is visualized in Figure 3.9. The concentration of sulfate particles is unconstrained without measurements of the volume-scattering and volume-absorption coefficients, and constrained equally well by each of the sets of scattering-profile measurements. The uncertainty in particle size distribution is well constrained for particles which are large enough to reasonate, but poorly constrained for very small particles. Polarimetric measurements improve posterior constraints on the size distribution when compared with phase function only measurements. All measurement sets constrain the posterior error bars for real refractive index, suggesting that the phase function may be sufficient for retrieving the real refractive index of sulfate aerosol.

Shown in Table 3.6, the relative uncertainty in various measures of sulfate concentration have a baseline of 51-53% uncertainty, corresponding to that of the prior distribution. In the posterior distributions, the volume concentration is resolved to 3% relative uncertainty, the suface area concentration is resolved to 8-9% relative uncertainty, and number concentration is resolved to 23-24% relative uncertainty. Loading parameters are unresolved in the absense of volume-coefficient measurements and resolved similarly well

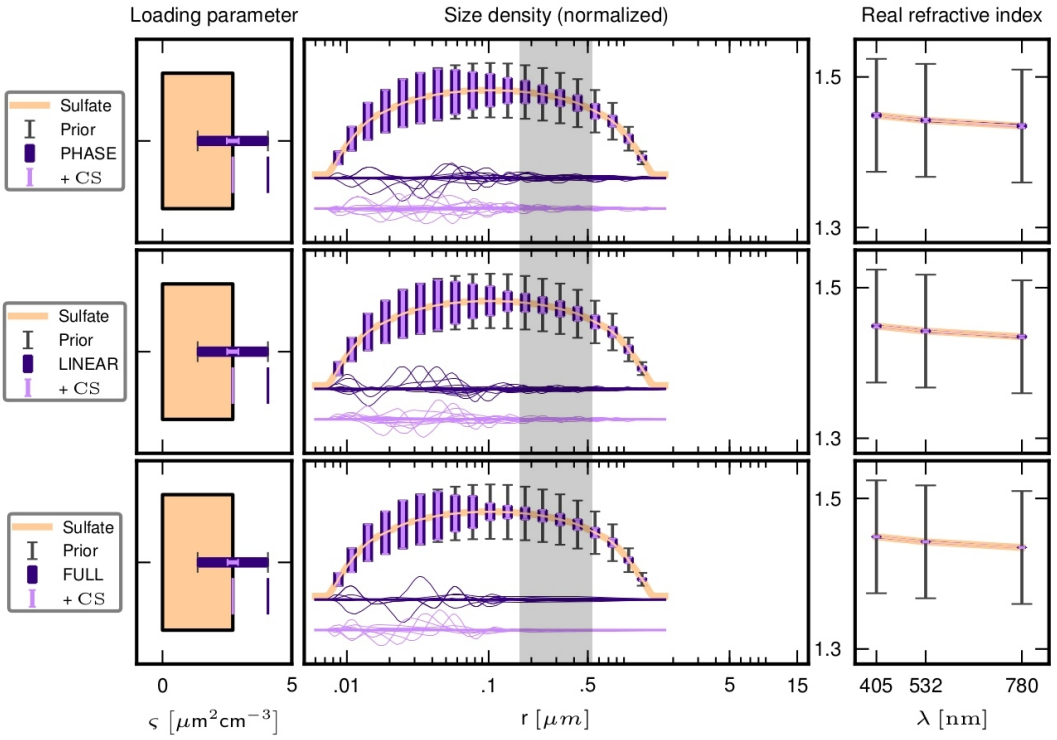

FIGURE 3.9: Sulfate prior and posterior uncertainty for concentration, size distribution, and real refractive index. Layout is the same as in Figure 3.5. The gray region shows resonating sizes at the shortest wavelength, $\lambda = 405$nm.

with or without polarimetric measurements. Relative uncertainty in the concentration of active CCN is 11-21%, and improves with polarimetric measurements — likely, due to decreased uncertainty in the size distribution. We note that the low uncertainty of 3% in volume concentration may be missleading, caused in part by our use of relative measurement error for the volume-absorption coefficient. A more realistic model for measurement error would include a combination of relative and absolute error, to impose a limit on the utility of absorption measurements for weakly absorbing aerosols like sulfate.

Figure 3.10 shows synthetic retrievals of the properties of sulfate aerosols, obtained by fitting full measurements with noise. With the exeption of small particles, the properties of sulfate are retrieved accurately and are stable with respect to measurement noise. As

TABLE 3.6: Relative uncertainty in sulfate concentration

	Concentration			CCN		
% Uncertainty	Number	Area	Volume	$r_{>31\text{nm}}$	$r_{>37\text{nm}}$	$r_{>43\text{nm}}$
Prior	53%	50%	51%	53%	53%	53%
Phase with coeficients	24%	9%	3%	21%	19%	16%
Linear with coeficients	24%	8%	3%	20%	17%	14%
Full with coeficients	23%	8%	3%	18%	15%	11%

with sea spray, the concentration and real refractive index are constrained close to their known true values. Variability in the size distribution for larger particles retrieved well, but error is seen for smaller particles. The measurment residules for these retrievals were well within noise levels.

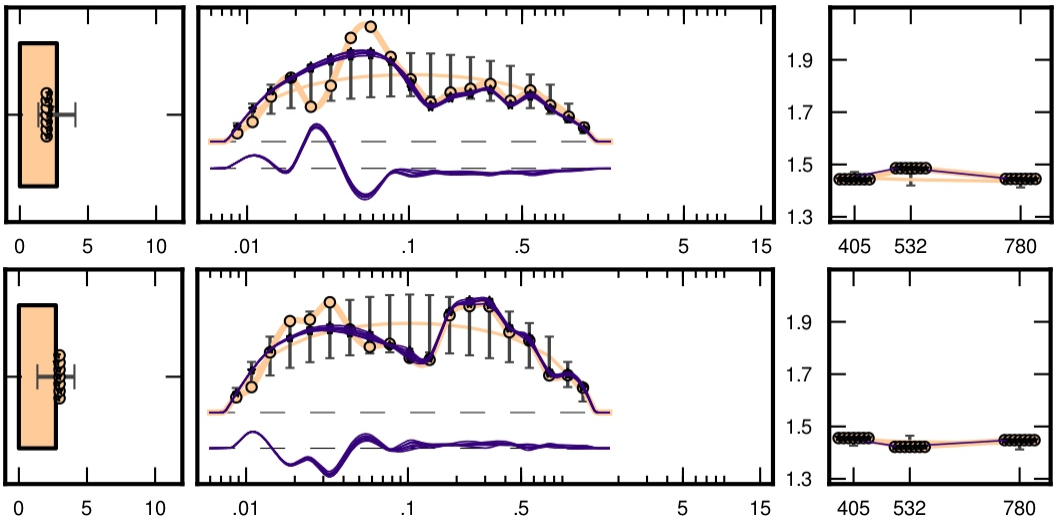

FIGURE 3.10: Synthetic retrievals of sulfate aerosol from full single-scattering measurements. The layout is the same as in Figure 3.8.

The case of sulfate aerosols included a much larger fraction of small particles than did the cases of sea spray and pure water. About one half the geometric crossection came from particles which were too small to reasonate with visible wavelengths of light. Still, certain measures of concentration were resolved along with the real refractive index and the size distribution of larger particles. Measurements of volume-coefficients were are nessesary

for resolving the volume and area concentration, and measurements of volume-coefficients and the phase profile where sufficient for this purpose. The number concentration was not resolved, and full measurement showed only marginally sensitive to concentration of active CCN. The real refractive index was resolved by all measurement sets. The benefit of polarimetric constraints is seen mostly in the uncertainty reduction of the size distribution, where linear-profile and full-profile measurements provide significant uncertainty reduction beyond measurements of the phase profile alone. Synthetic retrievals are stable and accurate for all sulfate properties, with the exception of the size distribution for small particles.

3.3.4 Tarballs

The linear stability analysis of tarballs is shown Tables 3.7 and 3.8 and in Figure 3.11 for all measurement sets, and synthetic retrievals are shown in Figure 3.12. The prior loading and size distribution for tarballs match those of the sulfate aerosol case, but the spectrally dependant values of the complex refractive index are much larger and more variable. Mean prior values for refractive index match those of laboratory retrievals [47].

The general results of the linear stability analysis are shown in Table 3.7. Measurements of volume-scattering and volume-absorption provide 5-6 bits of information for the concentration and 2-4 bits of information for the imaginary refractive index. The scattering matrix measurements provide 31-73 bits of information for the size distribution, 19-36 bits

of information for the real refractive index, and 11-17 bits of information for the imaginary refractive index. For tarball aerosols it seems that both volume-coefficients and scattering-profile measurements provide information for the imaginary refractive index.

TABLE 3.7: Stability analysis for tarballs: degrees of freedom and bits of information

			Information [bits]				
	d_{signal}	d_{prior}	Total	Concentration	Size	Real	Imaginary
Phase-profile data	12.3	13.7	71.6	0.0	31.0	19.6	11.2
Phase with coeficients	13.9	12.1	84.7	5.0	32.1	19.9	15.7
Linear-profile data	13.2	12.8	79.4	0.0	37.3	22.5	12.1
Linear with coefficients	14.7	11.3	92.0	5.3	38.4	22.6	16.2
Full-profile data	16.0	10.0	129.6	0.0	72.8	36.3	16.5
Full with coefficients	17.2	8.8	140.4	5.6	73.7	36.5	18.8

A more detailed view of the linear stability analysis for tarballs is shown in Figure 3.11. Concentration is unconstrained without volume-coefficient measurements and constrained similarly well for any set of scattering-profile measurements. Scattering matrix measurements provide constraints on the size distribution of particles which are large enough to resonate with visible light. Real refractive index is resolved well by all measurement sets, but the imaginary refractive index seems to be a more challenging target. Both volume-coefficients and scattering-profile measurements are needed to provide the strongest constraints, and this is especially noticable at the longest wavelength. This is likely due to the longer wavelength corresponding to a smaller size parameter, as discussed in Chapter 2.

The relative uncertainty in the concentration of tarballs is shown in Table 3.8. The baseline uncertainty for the concentration of tarballs is 51-53%, corresponding to that of the prior. In the posterior distributions, the volume concentration is resolved to 3% relative

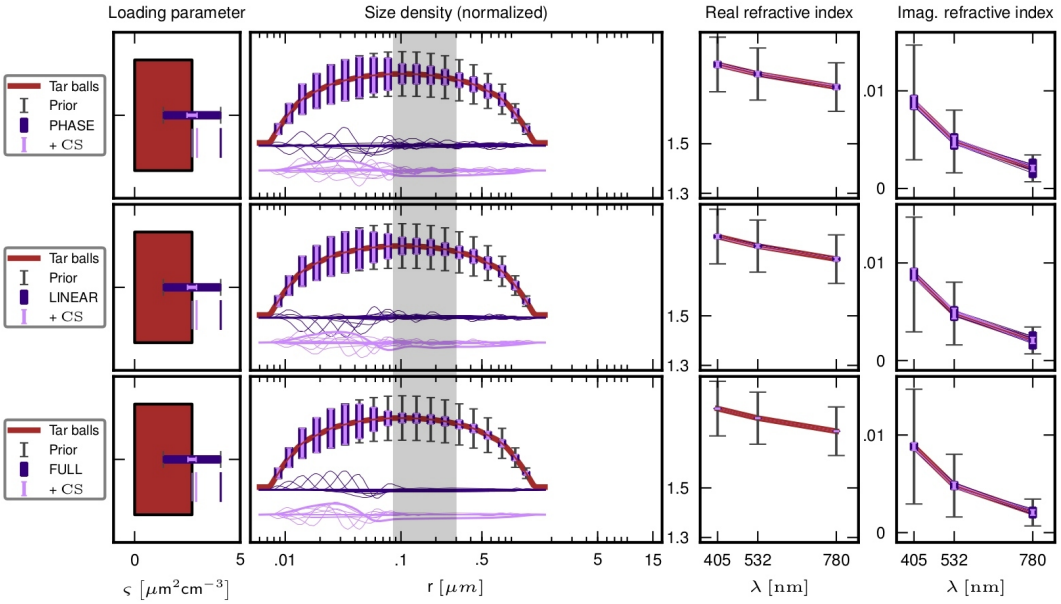

FIGURE 3.11: Tarballs prior and posterior uncertainty for concentration, size distribution, real refractive index and imaginary refractive index. The layout is similar to Figure 3.5, except plots of uncertainty for the real and imaginary refractive index are added in the two right-most columns. The gray region shows resonating sizes at the shortest wavelength, $\lambda = 405$nm.

uncertainty, the suface area concentration is resolved to 7-9% relative uncertainty, and the number concentration is resolved to 23-24% relative uncertainty. Loading parameters are unresolved without measurements of the volume-coefficients and resolved similarly with or without polarimetric measurements. The posterior relative uncertainty in CCN concentration is 8-21%, and improves with polarimetric measurements.

TABLE 3.8: Relative uncertainty in tarballs concentration

	Concentration			CCN		
% Uncertainty	Number	Area	Volume	$r_{>31\text{nm}}$	$r_{>37\text{nm}}$	$r_{>43\text{nm}}$
Prior	53%	50%	51%	53%	53%	53%
Phase with coefficients	24%	9%	3%	21%	19%	17%
Linear with coefficients	24%	8%	3%	19%	16%	12%
Full with coefficients	23%	7%	3%	16%	12%	8%

Synthetic retrievals for tarballs are shown in Figure 3.12. This case promising results

for the retrieval of spectrally dependent real and imaginary refractive index full measurements of single scattering properties. Note that the true values of refractive index are plotted with a colored circle and the retrievals are plotted with an astrix, so a filled circle corresponts to low retrieval error. By comparing the true and retrieved refractive indices, we see that, dispite significant deviation from their prior values, the real and imaginary refractive indices are retrieved quite well.

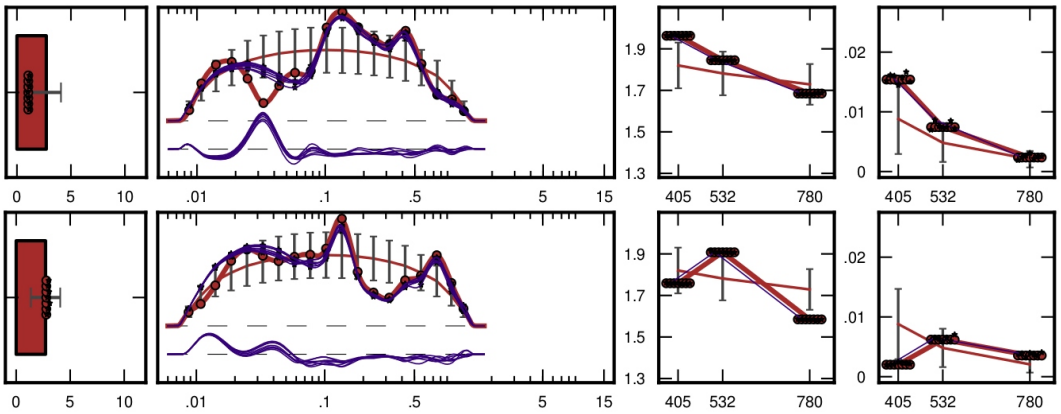

FIGURE 3.12: Synthetic retrievals of tarballs from full single-scattering measurements with noise. As in Figure 3.6, each row shows a different true state with seven random samples of measurement error.

The stability analysis and synthetic retrieval studies for tarballs show promising results for the characterization of this type of aerosol with measurements of the single-scattering properties. With the exception of small particles, all parameters are estimated to better than prior uncertainty and show low sensitivity to measurement errors. Refractive index retrievals for excellent accuracy dispite being far from the assumed prior mean. The dominante error pattern from the linear analysis is used to interpret the retrieval errors present in the loading and normalized size distribution.

3.3.5 Sulfate and tarballs

The linear stability analysis for the combined case of sulfate and tarballs is shown Tables 3.9 and 3.10 and in Figure 3.13 for all measurement sets, and synthetic retrievals are shown in Figure 3.14. The combined case of sulfate and tarballs consists of a small scattering mode (sulfate) which is externally mixed with a small absorping mode (tarballs). This mixed particle population poses the greatest challenge of cases considered here due to the apparent degeneracy in size distribution basis functions, which overlap perfectly for the two modes. The apparent degeneracy averted through the assumptions on prior distributions of refractive are substantially different for the two modes. Without the strong dependence of Mie single scattering properties on particle refractive index, the overlapping size distribution basis funtions for sulfate and tarballs would be indestinguishable from eachother.

Looking at the information content for this mixed population shows results that are similar single mode population with certain exceptions. We note that concentration is constrained by scattering-profile measurements alone, even without measurements of the volume-absorption and volume-scattering coefficients — due to the sensitivity of these data to changes in their mixing ratio. Measurements of the volume coefficients are still needed to resolve concentration well, and they are still needed to provide the best constraints on imaginary refractive index. More so than in the cases with a single mode of aerosol, the addition of polarization measurment seems to be required for resolving significant fraction of the aerosol properties beyond prior uncertainty.

TABLE 3.9: Stability analysis for the mixture of sulfate and tarballs

	d_{signal}	d_{prior}	Information [bits] Total	Concentration	Size	Real	Imaginary
Phase-profile data	15.7	36.3	77.8	3.5	30.9	16.5	6.5
Phase with coefficients	18.2	33.8	93.0	8.2	33.6	17.6	13.8
Linear-profile data	18.7	33.3	93.8	3.9	39.7	24.7	7.8
Linear with coefficients	20.9	31.1	107.9	8.9	41.7	25.6	14.2
Full-profile data	26.1	25.9	178.3	4.4	94.5	45.6	13.2
Full with coefficients	27.5	24.5	189.7	9.6	96.3	46.3	17.1

The fact that uncertainty for overlaping portions of the size distribution is reduce for both types of particles in figure 3.13 provides clear evidence for optical discrimination of similarly sized aerosols based on different refractive indices.

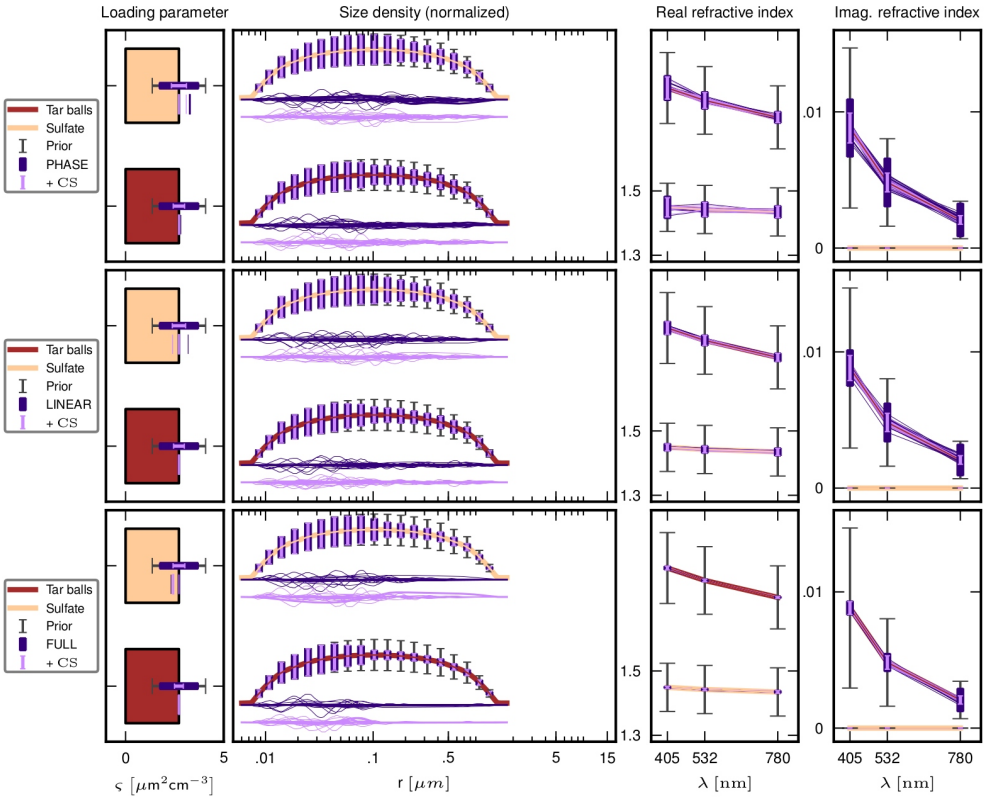

FIGURE 3.13: Prior and posterior uncertainties in for a mixture of sulfate and tarballs. The layout is similar to that of Figure 3.5.

The relative uncertainty in concentrations of tarballs and sulfate are shown in Table 3.10.

Prior concentration has relative uncertainty of 51-53%. Posterior distributions resolve the volume concentration to 3-5% relative uncertainty, the suface area concentration to 8-14% relative uncertainty, and the number concentration to 24-26% relative uncertainty. Volume coefficients are required. The relative uncertainty in CCN concentration is 13-27%, and improves with polarimetric measurements.

TABLE 3.10: Relative uncertainty in concentration for mixed sulfate and tarballs

Sulfate	Concentration			CCN		
% Uncertainty	Number	Area	Volume	$r_{>31\text{nm}}$	$r_{>37\text{nm}}$	$r_{>43\text{nm}}$
Prior	53%	50%	51%	53%	53%	53%
Phase with coefficients	26%	14%	6%	27%	27%	26%
Linear with coefficients	26%	12%	5%	26%	25%	24%
Full with coefficients	25%	11%	4%	25%	24%	23%

Tarballs	Concentration			CCN		
% Uncertainty	Number	Area	Volume	$r_{>31\text{nm}}$	$r_{>37\text{nm}}$	$r_{>43\text{nm}}$
Prior	53%	50%	51%	53%	53%	53%
Phase with coefficients	25%	11%	5%	23%	22%	20%
Linear with coefficients	24%	10%	4%	22%	20%	18%
Full with coefficients	24%	8%	3%	19%	16%	13%

The synthetic retrievals from full single-scattering measurements match true properties quite well for the mixture of sulfate and tarballs. Both size distributions are resolved for the larger-sized reasonating particles. The retrieved concentrations are clustered around the true concentrations for both modes. A slight bias in sulfate concentration appears to be balaced by an opposite bias in the retrieved size distribution, which is due to the normalization of the size distribution. This is consistent with the leading error pattern found by the linear stability analysis in figure 3.13. The retrieval of real and imaginary refractive index is fit quite accurately, given the large deviation between true and prior

values. Some sensitivity to measurement noise is observable but the sensitivity appears to be consistent with the linear stability analysis.

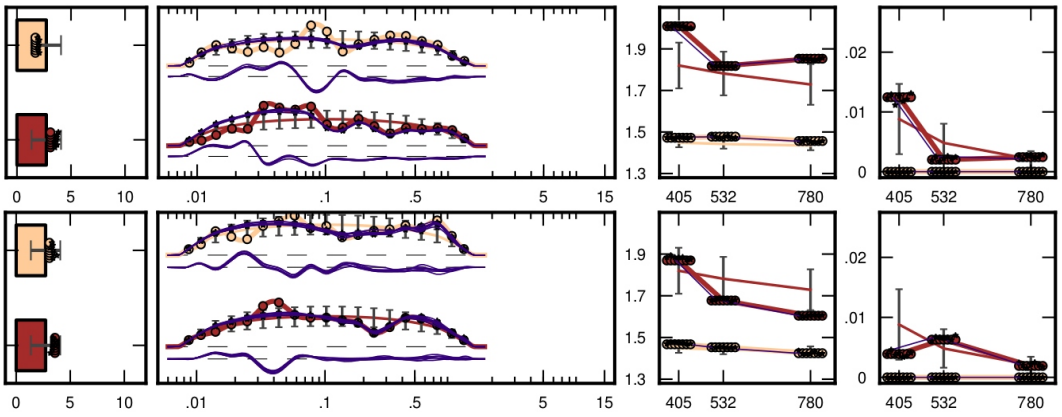

FIGURE 3.14: Synthetic retrievals of the mixture of sulfate and tarballs from full single-scattering measurements with random samples noise. The layout is similar to Figure 3.6.

The stability analysis for this observation system provides encouraging results. However, it is important to coment on an observation that was made when the mixing ratio of sulfate and tarballs was varried. These results are not shown, but we observed that the relative signal from the non-dominant mode causes larger retrieval errors and greater sensitivity to measurement noise. Likewise, the uncertainty for the dominant mode benefited and uncertainty was seen to converge to match the results of the corresponding single-mode analysis. It seemed that a ratio of one part in four was sufficient to provide substantial reduction of uncertainty in both modes in a mixture. The results within that range of mixing ratios are similar to equal mixture of sulfate and tarballs presented here. The complex refractive index and size distribution of larger particles are constrainted by full-profile measurements. And with the addition of volume-scattering and volume-absorption

coefficients, the concentration and imaginary refractive index of the aerosols are also constrained.

3.3.6 Sea spray and tarballs

The linear stability analysis of combined case of sea spray and tarballs is shown Tables 3.11 and 3.12 and in Figure 3.15 for all measurement sets. Following this, we show a synthetic retrieval study in Figure 3.16. Results for tarballs mixed with sea spary are slightly improved over those for the mixture with sulfate. We attribute this to the larger particles which are present in sea spray. This eliminates some the "apparrent degeneracy" caused by the complete overlap of the size distribution of sulfate and tarballs in Section 3.3.5. The size distribution for two modes in this mixture (sea spray and tarballs) do overlap, but only partily.

The linear stability analysis is summarized by Table 3.11. Without full scattering-profile measurements most of the information comes from the prior, and there is a large increase in information content when full scattering-profile measurements are added. For example, while the linear-profile measurements provide 47 bits of information for the size distribution, the ammount of information increases by nearly 60 bits with the additional polarimetric constraints that are contained in the full-profile measurments. The measurement sets which contain volume-coefficients provide 10-11 bits of information for

concentration and 14-17 bits of information for the imaginary refractive index, and without volume-coefficients the information content decreses to 4-5 bits for concentration and 6-13 bits for imaginary refractive index.

TABLE 3.11: Stability analysis for the mixture of sea spray and tarballs

			Information [bits]				
	d_{signal}	d_{prior}	Total	Concentration	Size	Real	Imaginary
Phase-profile data	18.9	35.1	88.2	4.4	36.3	22.2	6.1
Phase with coefficients	21.4	32.6	103.6	9.6	39.3	23.2	13.7
Linear-profile data	21.7	32.3	103.5	4.9	46.7	28.9	7.6
Linear with coefficients	23.7	30.3	117.7	10.4	48.8	29.5	14.2
Full-profile data	29.9	24.1	206.4	5.4	115.3	52.6	13.3
Full with coefficients	31.3	22.7	217.9	11.1	117.5	52.8	17.3

It seems that measurements of the volume coefficients and the full-scattering profile may be required to constrain the size distribution and complex refractive index, and the uncertainty reduction results, plotted in Figure 3.15, support these findings. Polarimetric measurements improve the resolution for both the size distribution and complex refractive index. Also, there is a noticable wavelength dependence in the uncertainty reduction in real and imaginary refractive index. The uncertainty in the imaginary refractive index for tarballs depends less on volume-coefficient measurements at shorter wavelengths than it does at larger wavelengths. This is consistent with the single-scattering calculations in Chapter 2, which show scattering profiles that approach the Rayleigh limit for smaller valumes of the particle size parameter, $x = \frac{2\pi r}{\lambda}$. This implies that measurements of the volume-coefficients may become increasingly important for resolving the imaginary refractive index, especially for longer wavelength measurements and smaller sized particles. This is likely due to the information contained in the volume-absorption coefficient, based

the dependence of absorption on particle volume concentration independent of size, as seen in Chapter 2.

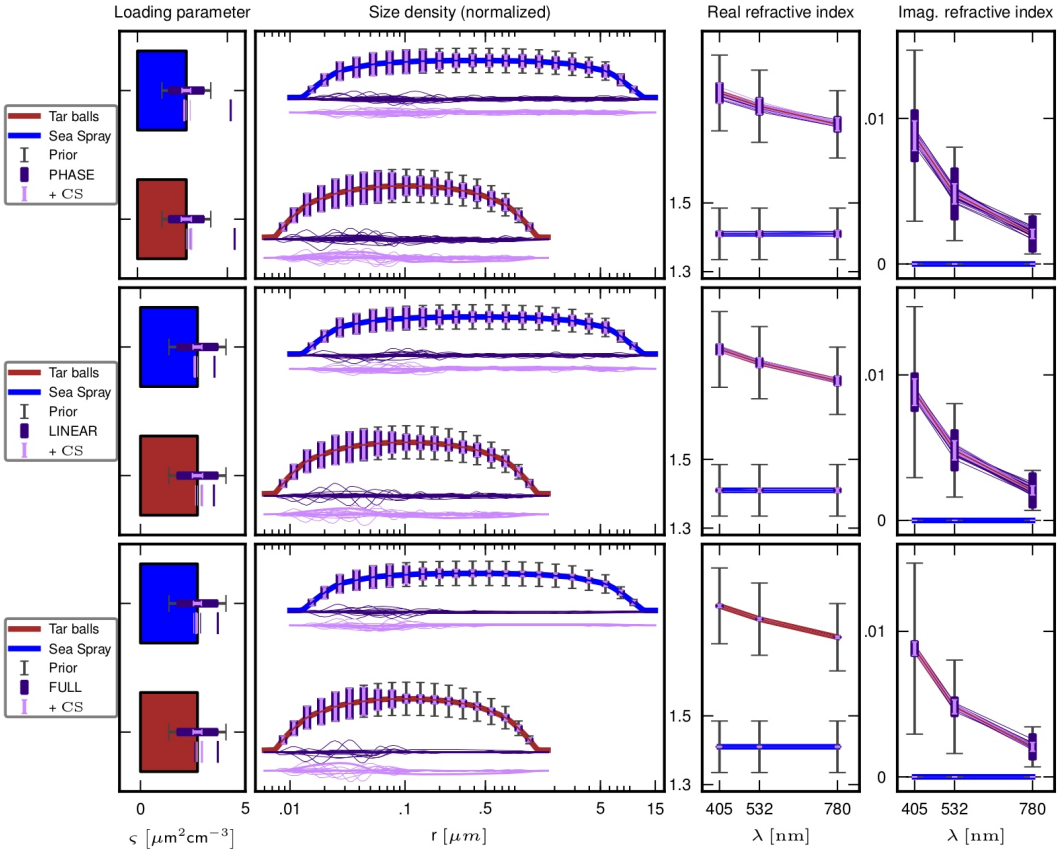

FIGURE 3.15: Prior and posterior uncertainties in for a mixture of sea spray and tarballs. The layout is similar to that of Figure 3.5.

The relative uncertainty of several measures of concentration are shown in Table 3.12. The baseline for relative uncertainty for each mode of particle in the mixture the relative uncertainty in concentration of the prior and this is 50-54%. The posterior distributions for the mixture of sea spray and tarballs have 3-7% relative uncertainty in volume concentration, 7-10% relative uncertainty in suface area concentration, and 23-25% relative uncertainty in the number concentration. Measurement sets without constraints on the volume coefficients provide some information, but only in the relative concentration of

the two types of particles. The posterior relative uncertainty in CCN concentration is 11-27%, and improves with polarimetric measurements. Relative uncertainty decreases for CCN concentration estimates that use a larger cutoff radius.

TABLE 3.12: Relative uncertainty in concentration for mixed sea spray and tarballs

Sea spray	Concentration			CCN		
% Uncertainty	Number	Area	Volume	$r_{>31\text{nm}}$	$r_{>37\text{nm}}$	$r_{>43\text{nm}}$
Prior	54%	50%	52%	54%	54%	54%
Phase with coefficients	25%	9%	7%	27%	27%	27%
Linear with coefficients	25%	8%	6%	26%	26%	25%
Full with coefficients	24%	7%	4%	25%	25%	24%
Tarballs	Concentration			CCN		
% Uncertainty	Number	Area	Volume	$r_{>31\text{nm}}$	$r_{>37\text{nm}}$	$r_{>43\text{nm}}$
Prior	53%	50%	51%	53%	53%	53%
Phase with coefficients	25%	10%	5%	24%	22%	21%
Linear with coefficients	24%	9%	4%	21%	18%	16%
Full with coefficients	23%	8%	3%	18%	15%	11%

The synthetic retrieval study of the mixed population of sea spray and tarballs is shown in Figure 3.16. All microphysical parameters are retrieved with the exception of the size distributions of small particles, and the retrievals are stabile with respect to measurement noise. Retrievals of the imaginary refractive index of tarballs are somewhat sensitive to noise, but the spread of values is comparable to the uncertainy seen in the linear stability analysis. The relative uncertainty of dependes on the mixing ratio of particles, and we noticed that retrievals of a mode degraded once the mixing ratio degraded below one part in four. However, in the first row of Figure 3.16 the fraction of tarballs is about one part in three, yet the retrieved concentration and complex refractive index values remain in close agreement with the true values.

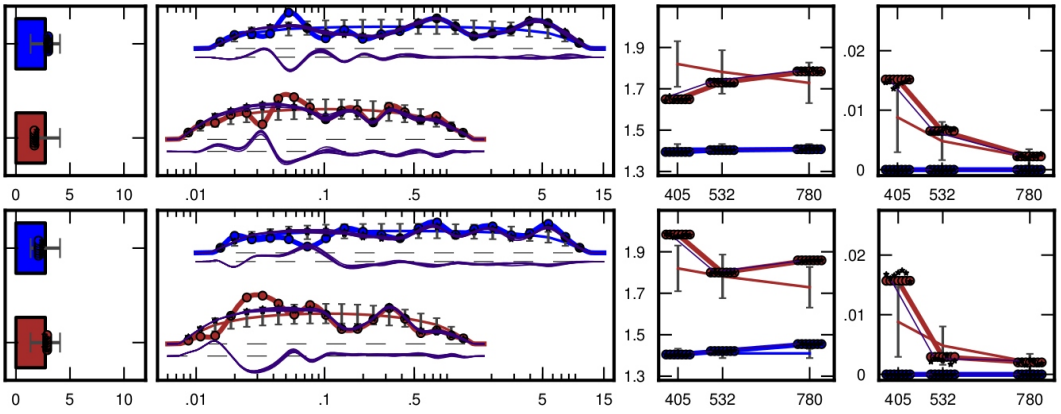

FIGURE 3.16: Synthetic retrievals of the mixture of sea spray and tarballs from full single-scattering measurements with random samples noise. The layout is similar to Figure 3.6.

We are optimistic that dual mode retrievals of sea spray and tarballs may be possible with full measurements of the scattering-matrix profiles together with measurements of the volume-scattering and volume-absorption coefficients. The concentration, size distribution, and spectrally dependent real refractive index are well constrained for both modes. This is seen in both the linear stability analysis and in the synthetic retrieval study. The large number of unknown parameters does seem to require full measurements, and in particular, the volume-coefficient measurements become increasingly important for longer wavelengths. Similarly, we expect that measurements of the volume-absorption coefficient are important for retrieving the imaginary refractive index of tarball — especially if the particles are smaller than those used in this study. As with the mixture of sulfate and tarballs, the mixing ratio of particles determines the extent to which each type of aerosol in the mixture is constrained. Mixing ratios down to one part in four seemed to allow retrieval of the complex refractive indices of both modes.

3.4 Concluding remarks

This chapter presented a theoretical analysis to determine what microphysical properties of airborne particles may be infered from noisy and incomplete measurements of their single-scattering properties. Small particles are very difficult to characterize. The uncertainty in the size distribution of small particles was unimproved, even with full measurements of the single-scattering properties. One of the most unfortunate consiquences is the poor estimates of particle number concintration — which plays an important role in cloud formation and is therefore a desirable retrieval target. The results are much more encouraging for particles which are large enough to reasonate with the measured wavelengths of light. For these larger particles, the size-distribution is well constrained even by incomplete measurements. We see this in both the linear stability analysis and in synthetic retrievals. Using full measurements, we see significant reduction in the uncertainty of size distribution and complex refractive index, even for bi-modal mixtures of aerosols with overlapping size distributions when their complex refractive indecies are separated by prior constraints. Incoroprating measurements of polarization has clear benefits over measurements of the phase-function profile alone and it is shown to reduce the uncertainty in the size distribution and complex refractive index. Measurements of the volume-scattering and volume-absorption coefficients constrain the mass concentration of aerosols quite well and also add information for the retrieval of imaginary refractive index. Therefore, the retrieval of larger particles seems reasonable and we expect that the size distribution and complex refractive index of one or two modes of aerosol may be

infered from single-scattering measurements.

Chapter 4

Remote sensing in 3D

This chapter derives an efficient procedure for using the three-dimensional (3D) vector radiative transfer equation (VRTE) to adjust atmosphere and surface properties and improve their fit with multi-angle/multi-pixel radiometric and polarimetric measurements of scattered sunlight. The proposed adjoint method uses the 3D VRTE to compute the measurement misfit function and the adjoint 3D VRTE to compute its gradient with respect to all unknown parameters.

In the remote sensing problems of interest, the scalar-valued misfit function quantifies agreement with data as a function of atmosphere and surface properties, and its gradient guides the search through this parameter space. Remote sensing of the atmosphere and surface in a three-dimensional region may require thousands of unknown parameters and millions of data points. Many approaches would require calls to the 3D VRTE solver in proportion to the number of unknown parameters or measurements. To avoid this issue

of scale, we focus on computing the gradient of the misfit function as an alternative to the Jacobian of the measurement operator. The resulting adjoint method provides a way to adjust 3D atmosphere and surface properties with only two calls to the 3D VRTE solver for each spectral channel, regardless of the number of retrieval parameters, measurement view angles or pixels.

This gives a procedure for adjusting atmosphere and surface parameters that will scale to the large problems of 3D remote sensing. For certain types of multi-angle/multi-pixel polarimetric measurements, this encourages the development of a new class of three-dimensional retrieval algorithms with more flexible parameterizations of spatial heterogeneity, less reliance on data screening procedures, and improved coverage in terms of the resolved physical processes in the Earth's atmosphere.

4.1 Objectives

More accurate and complete monitoring of cloud and aerosol properties is needed to reduce uncertainties in both the radiative forcing of climate and feedbacks between the radiative forcing and changes in global temperature that are the result of changes to clouds and their properties [7]. While multi-angle polarimetric measurements and plane parallel retrieval methods provide the capabilities necessary for regions that are horizontally homogeneous [6, 8, 9], the retrieval of aerosols in broken cloud fields and near cloud edges remains an open challenge which limits the coverage and accuracy of retrievals [11–13]. Using the three-dimensional (3D) vector radiative transfer equation (VRTE) can address this

issue by explicitly accounting for the spatial distribution of solar illumination, scattering material, and polarimetric measurements. In contrast to plane-parallel and spherical models for radiative transfer, the 3D VRTE places no default restrictions on the spatial variability of the atmosphere and surface [62]. Work to extend coverage with 3D methods has shown promise for determining average cloud optical thickness [15] and cloud top height [16]. However, as a side effect of the increased flexibility, the 3D VRTE leads to retrieval problems with many more unknown parameters and multi-pixel measurement constraints. A significant concern is therefore the extent to which a proposed algorithm scales "gracefully" to large problems. The objective of this work is to formulate an adjoint method for the 3D VRTE which maintains the scalability required for application to atmospheric remote sensing problems.

Adjoint methods and other linearization procedures can reduce the number of radiative transfer simulations needed over the course of an iterative procedure for fitting data [63, 64]. During each iteration, the current estimate of the atmosphere and surface properties is adjusted to improve its fit with measurements. Making the right adjustment requires knowledge of how the fit will change when the adjustment is made. This in turn entails solving the 3D VRTE for each wavelength to evaluate the misfit between model and measurements and its gradient with respect to unknown parameters. It is worth noting that, brute-force numerical differencing could be used to compute the gradient with $\mathcal{O}(LN)$ radiative transfer computations, where N is the number of parameters and L is the number of wavelengths. Adjoint methods provide an alternative route to computing this derivative, and analogous work in the field of medical imaging shows that the number of

calls to the radiative transfer solver can be as low as two: one forward solve for evaluating the misfit with data and one adjoint solve for computing the gradient with respect to retrieval parameters [20, 65, 66]. Although this result was specific to angularly-averaged measurements in the frequency domain with wavelength-independent parameters, it is an example of a scalable adjoint method derived for an analogous scalar transport equation. We define a retrieval adjustment procedure as *scalable* if it can be applied to problems with arbitrarily many measurement constraints and unknown parameters without requiring additional calls to a radiative transfer simulation. A scalable method can require $\mathcal{O}(L)$ radiative transfer solutions at each step, but not $\mathcal{O}(LN)$ or $\mathcal{O}(M)$, where M is the number of measurements (including all wavelengths, view angles and pixels).

Previous work on adjoint/linearization methods for remote sensing provides this kind of improved efficiency for plane-parallel [67], spherical [68–70], and pseudo-spherical radiative transfer models [71–73]. Also, adjoint techniques have been used to approximate solutions to the 3D VRTE for atmospheric properties with small deviations from plane-parallel symmetry [74, 75]. To our knowledge, the use of adjoint methods to develop a scalable remote sensing methodology that relies on the 3D VRTE has not hitherto been considered. This topic is of current interest due to the advancement of computational techniques, which simulate 3D scalar and vector RT in the Earth's atmosphere [76–80], including the recently released vectorized Spherical Harmonic Discrete Ordinate Method code by Evans [81]. So far, the primary application of these codes has been synthetic studies which assess errors associated with plane-parallel retrievals [82, 83]. In our view an equally important direction of research deals with how to incorporate simulations of

the 3D VRTE directly into cloud and aerosol retrieval algorithms [15]: for example, using multi-pixel methods to improve single-pixel retrievals by accounting for adjacency effects, or perhaps, using a futuristic 3D parameterization of clouds and aerosols to retrieve their spatial variability in complex scenes with broken cloud cover. The objective of this paper is to provide the necessary theoretical foundation for such endeavors, by extending adjoint methods to allow scalable computations of the misfit function and its gradient using codes that solve the 3D VRTE.

To ensure that the adjoint method derived here meets the needs of the atmospheric remote sensing community, the theoretical description of measurements is consistent with ground-based, air-borne, and space-borne polarimeters, and the parameter-adjustment methods are similar to those used in operational retrieval algorithms [51, 67]. The method focuses on minimizing a misfit function for passive measurements of scattered sunlight, but active measurements and measurements at other wavelengths may be included as prior constraints on spatial variability: using high spectral resolution LIDAR to constrain the aerosol scattering coefficient [17] or microwave cloud tomography to constrain cloud-droplet volume concentration [18, 19]. Moreover, we formulate the adjoint framework in a manner that is consistent with the complex microphysical parameterizations needed to model single-scattering properties in the Earth's atmosphere [33]. The procedure is outlined using the standard integro-differential form of the 3D VRTE and derived using an equivalent integral formulation, written using concise operator notation for the processes of streaming, scattering and reflection. The integral formulation and associated operators are related to existing numerical solutions, and we describe how to extend such codes to

solve adjoint radiative transfer by using the reciprocity principle to write the adjoint Stokes-vector solution in terms of a slight modification to the usual forward solution.

Preliminary definitions are given in Section 4.2 with the fundamental adjoint property asserted but left temporarily unproven. The use of adjoint methods in developing a scalable procedure for adjusting parameters as part of a remote sensing methodology is described in Section 4.3. Then, the general framework for forward and adjoint 3D VRTE is derived in Section 4.4 and the fundamental adjoint property is proven in Theorem 4.4. Supplementary technical results are presented in B.1 and B.2.

4.2 Preliminaries

This section introduces the theoretical framework of the forward and adjoint 3D VRTE as needed for large scale 3D remote sensing of the atmosphere and surface. We generalize adjoint methods to arbitrary boundary conditions, and this entails a mild reformulation of the forward 3D VRTE as a boundary value problem and proof of the *fundamental adjoint property* for the corresponding boundary value problem of adjoint 3D VRTE. The logical progression that we choose to follow is to define the forward and adjoint 3D VRTEs as independent boundary value problems. Then, we prove the fundamental adjoint property which relates them. The first task is to define the domain.

Definition 4.1 (Domain)**.** The spatial region of interest is an open, connected, and bounded set $D \subset \mathbb{R}^3$ with smooth boundary $\partial D \subset \mathbb{R}^3$ — smooth to guarantee that

the bounding surface has a continuous outward-pointing normal vector. The region is described implicitly by it's *signed-distance-to-boundary* function:

$$h(\boldsymbol{x}) = \begin{cases} -\inf\limits_{\boldsymbol{x}' \in \partial D} \|\boldsymbol{x} - \boldsymbol{x}'\| & \text{for} \quad \boldsymbol{x} \in (D \cup \partial D) \\ \inf\limits_{\boldsymbol{x}' \in \partial D} \|\boldsymbol{x} - \boldsymbol{x}'\| & \text{for} \quad \boldsymbol{x} \in \mathbb{R}^3 \backslash (D \cup \partial D) \end{cases} . \tag{4.1}$$

The useful properties of h are that it is continuous on $\mathbb{R}^3$ and differentiable near the boundary, with gradient $\nabla h(\boldsymbol{x})$ equal to the unit normal vector pointing out of the domain for each $\boldsymbol{x} \in \partial D$. The function value determines if a given point, $\boldsymbol{x} \in \mathbb{R}^3$, is inside the region of interest, $h(\boldsymbol{x}) < 0$; on its boundary, $h(\boldsymbol{x}) = 0$; or outside, $h(\boldsymbol{x}) > 0$.

Taking the direction vector $\boldsymbol{v}$ to be always in the unit sphere, $\mathbb{S}^2 \subset \mathbb{R}^3$; we define the three regions making up the domain of the 3D VRTE: the *internal set*,

$$D \times \mathbb{S}^2 = \{\, (\boldsymbol{x}, \boldsymbol{v}) : \; h(\boldsymbol{x}) < 0 \,\}, \tag{4.2}$$

the *outgoing set*,

$$\Gamma_+ = \{\, (\boldsymbol{x}, \boldsymbol{v}_+) : \; h(\boldsymbol{x}) = 0 \quad \text{and} \quad \boldsymbol{v}_+ \cdot \nabla h(\boldsymbol{x}) > 0 \,\}, \tag{4.3}$$

and the *incoming set*,

$$\Gamma_- = \{\, (\boldsymbol{x}, \boldsymbol{v}_-) : \; h(\boldsymbol{x}) = 0 \quad \text{and} \quad \boldsymbol{v}_- \cdot \nabla h(\boldsymbol{x}) < 0 \,\}. \tag{4.4}$$

Inner products of Stokes-vector and source-vector functions are defined for each domain: the *internal inner product*,

$$\langle \boldsymbol{w}, \boldsymbol{u} \rangle_{D\times\mathbb{S}^2} = \int_{h(\boldsymbol{x})<0} \mathrm{d}V_{\boldsymbol{x}} \int_{\mathbb{S}^2} \mathrm{d}S_{\boldsymbol{v}}\; \boldsymbol{w}(\boldsymbol{x},\boldsymbol{v}) \cdot \boldsymbol{u}(\boldsymbol{x},\boldsymbol{v}), \tag{4.5}$$

the *outgoing inner product*,

$$\langle \boldsymbol{q}, \boldsymbol{u} \rangle_{\Gamma_+} = \int_{h(\boldsymbol{x})=0} \mathrm{d}S_{\boldsymbol{x}} \int_{\boldsymbol{v}_+\cdot\nabla h(\boldsymbol{x})>0} \mathrm{d}S_{\boldsymbol{v}_+}\; |\boldsymbol{v}_+\cdot\nabla h(\boldsymbol{x})|\, \boldsymbol{q}(\boldsymbol{x},\boldsymbol{v}_+) \cdot \boldsymbol{u}(\boldsymbol{x},\boldsymbol{v}_+), \tag{4.6}$$

and the *incoming inner product*,

$$\langle \boldsymbol{w}, \boldsymbol{g} \rangle_{\Gamma_-} = \int_{h(\boldsymbol{x})=0} \mathrm{d}S_{\boldsymbol{x}} \int_{\boldsymbol{v}_-\cdot\nabla h(\boldsymbol{x})<0} \mathrm{d}S_{\boldsymbol{v}_-}\; |\boldsymbol{v}_-\cdot\nabla h(\boldsymbol{x})|\, \boldsymbol{w}(\boldsymbol{x},\boldsymbol{v}_-)\cdot\boldsymbol{g}(\boldsymbol{x},\boldsymbol{v}_-). \tag{4.7}$$

These elementary inner products appear so often in pairs that is helpful to write the *forward inner product* as,

$$\left\langle \begin{Bmatrix} \boldsymbol{p} \\ \boldsymbol{q} \end{Bmatrix}, \begin{Bmatrix} \boldsymbol{u}|_{D\times\mathbb{S}^2} \\ \boldsymbol{u}|_{\Gamma_+} \end{Bmatrix} \right\rangle_{D\times\mathbb{S}^2\oplus\Gamma_+} = \langle \boldsymbol{p}, \boldsymbol{u} \rangle_{D\times\mathbb{S}^2} + \langle \boldsymbol{q}, \boldsymbol{u} \rangle_{\Gamma_+}, \tag{4.8}$$

and the *adjoint inner product* as,

$$\left\langle \begin{Bmatrix} \boldsymbol{w}|_{D\times\mathbb{S}^2} \\ \boldsymbol{w}|_{\Gamma_-} \end{Bmatrix}, \begin{Bmatrix} \boldsymbol{f} \\ \boldsymbol{g} \end{Bmatrix} \right\rangle_{D\times\mathbb{S}^2\oplus\Gamma_-} = \langle \boldsymbol{w}, \boldsymbol{f} \rangle_{D\times\mathbb{S}^2} + \langle \boldsymbol{w}, \boldsymbol{g} \rangle_{\Gamma_-}. \tag{4.9}$$

Each of the three inner products in Eqs. (4.5) - (4.7) defines a vector space of *square-integrable* functions, for example the internal source vectors, $\boldsymbol{f}$, such that,

$$\|\boldsymbol{f}\|^2_{D\times\mathbb{S}^2} = \langle \boldsymbol{f}, \boldsymbol{f}\rangle_{D\times\mathbb{S}^2} < \infty, \tag{4.10}$$

or the incoming source vectors, $\boldsymbol{g}$, such that,

$$\|\boldsymbol{g}\|^2_{\Gamma_-} = \langle \boldsymbol{g}, \boldsymbol{g}\rangle_{\Gamma_-} < \infty. \tag{4.11}$$

From the operator point of view, the square-integrable functions in Eqs. (4.10) and (4.11) are vectors in a linear space, and linear operators will act in much the same way that matrices do. To guarantee this, we give symbolic representation only to linear operators that are bounded. By this convention, a linear operator with symbol, $\mathcal{L}$, will act on a square-integrable vector, $\boldsymbol{f}$, and return another square-integrable vector, $\mathcal{L}[\boldsymbol{f}]$. This follows from the definition of a bounded operator: the linear operator, $\mathcal{L}$, is *bounded* if there exists a value, C, so that,

$$\| \mathcal{L}[\boldsymbol{f}] \| \leq C \ \| \boldsymbol{f} \|, \tag{4.12}$$

for all square-integrable functions, $\boldsymbol{f}$. The smallest such value, C, is called the *operator norm*, $\| \mathcal{L} \|_{\text{op}}$, and it will be needed in Section 4.4.2 to state the constraints on scattering and reflection that guarantee solve-ability of the 3D VRTE. The adjoint of an operator

is defined in the usual sense, as the operator, $\mathcal{L}^*$, which satisfies the adjoint property:

$$\langle \boldsymbol{p},\ \mathcal{L}\left[\boldsymbol{f}\right]\rangle = \langle \mathcal{L}^*\left[\boldsymbol{p}\right],\ \boldsymbol{f}\rangle\,. \tag{4.13}$$

The adjoint, $\mathcal{L}^*$, gives the alternative rule for evaluating the inner product in Eq. (4.13), so that numerical procedures may use whichever side is more efficient.

In summary, the three distinct subdomains for 3D vector radiative transfer are defined through the utility function, $h(\boldsymbol{x})$: the interior set, $D \times \mathbb{S}^2$; outgoing set, Γ_+; and the incoming set, Γ_-. Each subdomain has an inner product and set of square-integrable functions. As a convention, we reserve operator notation for bounded linear operators to ensure similarity to matrix algebra. Lastly, the adjoint of a linear operator was defined.

4.2.1 Forward and adjoint 3D VRTEs

The purpose of this paper is to formulate an efficient procedure for adjusting unknown parameters as part of an abstract remote sensing problem. The atmosphere and surface properties are described by an unknown parameter vector, $\boldsymbol{a} = (a^n)$ for $0 \leq n < N$, from which physical single-scattering properties are derived: extinction, $\sigma(\boldsymbol{x};\boldsymbol{a})$; scattering kernel, $\boldsymbol{Z}(\boldsymbol{x},\boldsymbol{v},\boldsymbol{v}';\boldsymbol{a})$; and reflection kernel, $\boldsymbol{R}(\boldsymbol{x},\boldsymbol{v}_-,\boldsymbol{v}_+;\boldsymbol{a})$. For a given illumination defined by incoming and internal light sources, the 3D VRTE provides a solution vector $\boldsymbol{u}(\boldsymbol{x},\boldsymbol{v};\boldsymbol{a})$ to be used in modeling each polarimetric measurement as an inner product

over a pair of polarimetric response functions, $\boldsymbol{p}_{\odot}^{m}$ and $\boldsymbol{q}_{\odot}^{m}$:

$$y^m(\boldsymbol{a}) = \left\langle \boldsymbol{p}_{\odot}^{m}, \boldsymbol{u} \right\rangle_{D\times\mathbb{S}^2} + \left\langle \boldsymbol{q}_{\odot}^{m}, \boldsymbol{u} \right\rangle_{\Gamma_+}, \tag{4.14}$$

$$= \left\langle \left\{ \begin{array}{c} \boldsymbol{p}_{\odot}^{m} \\ \\ \boldsymbol{q}_{\odot}^{m} \end{array} \right\}, \left\{ \begin{array}{c} \boldsymbol{u}|_{D\times\mathbb{S}^2} \\ \\ \boldsymbol{u}|_{\Gamma_+} \end{array} \right\} \right\rangle_{D\times\mathbb{S}^2\oplus\Gamma_+}, \tag{4.15}$$

with measurement vector $\boldsymbol{y} = (y^m)$ for $0 \leq m < M$. This motivates the boundary value problem of the 3D VRTE which defines the Stokes vector solution, $\boldsymbol{u}$, for incoming solar energy.

Definition 4.2 (Forward 3D VRTE)**.** For a fixed parameter vector, $\boldsymbol{a}$, and corresponding single-scattering properties, σ, $\boldsymbol{Z}$, and $\boldsymbol{R}$; the forward solution $\boldsymbol{u}(\boldsymbol{x}, \boldsymbol{v}; \boldsymbol{a})$ is defined for square-integrable source vectors, $\boldsymbol{f}_{\odot}$ and $\boldsymbol{g}_{\odot}$, as the unique solution to the integro-differential equations of the forward 3D VRTE:

$$\boldsymbol{v}\cdot\nabla\boldsymbol{u} + \sigma\boldsymbol{u} - \mathcal{Z}[\,\boldsymbol{u}\,] = \boldsymbol{f}_{\odot} \quad \text{on} \quad D\times\mathbb{S}^2, \tag{4.16}$$

$$\boldsymbol{u}|_{\Gamma_-} - \mathcal{R}\big[\,\boldsymbol{u}|_{\Gamma_+}\,\big] = \boldsymbol{g}_{\odot} \quad \text{on} \quad \Gamma_-. \tag{4.17}$$

The integral operator for scattering is defined as,

$$\mathcal{Z}[\,\boldsymbol{u}\,](\boldsymbol{x}, \boldsymbol{v}) = \frac{1}{4\pi}\int_{\mathbb{S}^2} \mathrm{d}S_{\boldsymbol{v}'}\,\boldsymbol{Z}(\boldsymbol{x}, \boldsymbol{v}, \boldsymbol{v}')\cdot\boldsymbol{u}(\boldsymbol{x}, \boldsymbol{v}'), \tag{4.18}$$

for $(\boldsymbol{x}, \boldsymbol{v}) \in D \times \mathbb{S}^2$, and the integral operator for reflection is defined as,

$$\mathcal{R}\big[\, \boldsymbol{u}|_{\Gamma_+} \,\big](\boldsymbol{x}, \boldsymbol{v}_-) = \frac{1}{2\pi} \int_{\boldsymbol{v}_+ \cdot \nabla h(\boldsymbol{x}) > 0} \mathrm{d}S_{\boldsymbol{v}_+} |\boldsymbol{v}_+ \cdot \nabla h(\boldsymbol{x})| \boldsymbol{R}(\boldsymbol{x}, \boldsymbol{v}_-, \boldsymbol{v}_+) \cdot \boldsymbol{u}(\boldsymbol{x}, \boldsymbol{v}_+), \tag{4.19}$$

for $(\boldsymbol{x}, \boldsymbol{v}_-) \in \Gamma_-$. Coupling with boundary conditions is imposed by spatial continuity along outgoing and incoming directions:

$$\boldsymbol{u}|_{\Gamma_+}(\boldsymbol{x}, \boldsymbol{v}_+) = \lim_{t \searrow 0} \boldsymbol{u}|_{D \times \mathbb{S}^2}(\boldsymbol{x} - t\boldsymbol{v}_+, \boldsymbol{v}_+), \tag{4.20}$$

$$\boldsymbol{u}|_{\Gamma_-}(\boldsymbol{x}, \boldsymbol{v}_-) = \lim_{t \searrow 0} \boldsymbol{u}|_{D \times \mathbb{S}^2}(\boldsymbol{x} + t\boldsymbol{v}_-, \boldsymbol{v}_-), \tag{4.21}$$

for $(\boldsymbol{x}, \boldsymbol{v}_+) \in \Gamma_+$ and $(\boldsymbol{x}, \boldsymbol{v}_-) \in \Gamma_-$.

Assuming existence and uniqueness for the moment, we define the solution operator for the boundary value problem of the forward 3D VRTE, $\mathcal{U}_{\boldsymbol{a}}\{\cdot\}$:

$$\begin{Bmatrix} \boldsymbol{u}|_{D \times \mathbb{S}^2} \\ \boldsymbol{u}|_{\Gamma_+} \end{Bmatrix} = \mathcal{U}_{\boldsymbol{a}} \begin{Bmatrix} \boldsymbol{f}_\odot \\ \boldsymbol{g}_\odot \end{Bmatrix}. \tag{4.22}$$

The forward solution operator, $\mathcal{U}_{\boldsymbol{a}}$, is a 2×2 matrix of integral operators which is parametrized by $\boldsymbol{a}$ and acts on internal and incoming source vectors, $\boldsymbol{f}_\odot$ and $\boldsymbol{g}_\odot$, to give the Stokes vector solution on the internal and outgoing sets, $\boldsymbol{u}|_{D \times \mathbb{S}^2}$ and $\boldsymbol{u}|_{\Gamma_+}$. An explicit formula for the forward solution operator is derived in Section 4.4.2.1 and given by Eq. (4.112).

The solution operator, $\mathcal{U}_{\boldsymbol{a}}$, plays the role of a forward solver in the present discussion

of an abstract remote sensing problem — one call to a forward solver is equivalent to evaluating the solution operator, $\mathcal{U}_{\boldsymbol{a}}$, for one pair of source vectors, $\boldsymbol{f}_\odot$ and $\boldsymbol{q}_\odot$. Using this operator we write the model for polarimetric measurements in Eq. (4.15) as the inner product of detector response functions, $\boldsymbol{p}^m_\odot$ and $\boldsymbol{q}^m_\odot$, with the Stokes vector solution for solar illumination:

$$y^m(\boldsymbol{a}) = \left\langle \begin{Bmatrix} \boldsymbol{p}^m_\odot \\ \boldsymbol{q}^m_\odot \end{Bmatrix}, \mathcal{U}_{\boldsymbol{a}} \begin{Bmatrix} \boldsymbol{f}_\odot \\ \boldsymbol{g}_\odot \end{Bmatrix} \right\rangle_{D\times\mathbb{S}^2\oplus\Gamma_+} . \tag{4.23}$$

This expression allows the computation of all measurements with one call to the solution operator, $\mathcal{U}_{\boldsymbol{a}}$, followed by relatively inexpensive integrations over the polarimetric response function for each detector. Therefore, Eq. (4.23) is well suited to the task of evaluating many different measurements for fixed internal and incoming source vectors.

However, in remote sensing applications where unknown atmosphere and surface parameters, $\boldsymbol{a}$, are adjusted to fit data, the computation also requires variation of source functions for computing the components of the gradient of the misfit function, $\partial\Phi/\partial a^n$. We will see in Section 4.3 that the desired quantity has the following form:

$$-\frac{\partial\Phi}{\partial a^n} = \left\langle \begin{Bmatrix} \boldsymbol{\Delta p}_\odot \\ \boldsymbol{\Delta q}_\odot \end{Bmatrix}, \mathcal{U}_{\boldsymbol{a}} \begin{Bmatrix} \boldsymbol{\Delta f}^n_\odot \\ \boldsymbol{\Delta g}^n_\odot \end{Bmatrix} \right\rangle_{D\times\mathbb{S}^2\oplus\Gamma_+} , \tag{4.24}$$

for fixed adjoint source vectors, $\boldsymbol{\Delta p}_\odot$ and $\boldsymbol{\Delta q}_\odot$, and forward source vectors, $\boldsymbol{\Delta f}^n_\odot$ and $\boldsymbol{\Delta g}^n_\odot$, corresponding to derivatives with respect to each parameter, for $0 \leq n < N$. Forward and adjoint source vectors appearing in Eq. (4.24) are defined explicitly by Eqs.

(4.42), (4.43), (4.46), and (4.47). To avoid repeated calls to the solver, $\mathcal{U}_{\boldsymbol{a}}$, we seek the adjoint of the forward solution operator. This adjoint operator, $(\mathcal{U}_{\boldsymbol{a}})^*$, is defined to satisfy the adjoint property:

$$\begin{aligned}\left\langle \begin{Bmatrix} \boldsymbol{\Delta p}_\odot \\ \boldsymbol{\Delta q}_\odot \end{Bmatrix}, \mathcal{U}_{\boldsymbol{a}} \begin{Bmatrix} \boldsymbol{\Delta f}^n_\odot \\ \boldsymbol{\Delta g}^n_\odot \end{Bmatrix} \right\rangle_{D\times\mathbb{S}^2\oplus\Gamma_+} \\ = \left\langle (\mathcal{U}_{\boldsymbol{a}})^* \begin{Bmatrix} \boldsymbol{\Delta p}_\odot \\ \boldsymbol{\Delta q}_\odot \end{Bmatrix}, \begin{Bmatrix} \boldsymbol{\Delta f}^n_\odot \\ \boldsymbol{\Delta g}^n_\odot \end{Bmatrix} \right\rangle_{D\times\mathbb{S}^2\oplus\Gamma_-}\end{aligned} \tag{4.25}$$

Notice that all solver operations now act on the fixed adjoint source vectors, $\boldsymbol{\Delta p}_\odot$ and $\boldsymbol{\Delta q}_\odot$, so that the change in fit can be computed for any unknown parameter by integration. This motivates the definition of the boundary value problem for the adjoint 3D VRTE.

Definition 4.3 (Adjoint 3D VRTE)**.** For fixed parameter, $\boldsymbol{a}$, and single-scattering properties, σ, $\boldsymbol{Z}$, and $\boldsymbol{R}$; we define the adjoint solution, $\boldsymbol{w}$, for square-integrable adjoint source vectors, $\boldsymbol{p}_\odot$ and $\boldsymbol{q}_\odot$, as the unique solution to the adjoint 3D VRTE:

$$-\boldsymbol{v}\cdot\nabla\boldsymbol{w} + \sigma\boldsymbol{w} - \mathcal{Z}^*[\,\boldsymbol{w}\,] = \boldsymbol{p}_\odot \quad \text{on} \quad D\times\mathbb{S}^2, \tag{4.26}$$

$$\boldsymbol{w}|_{\Gamma_+} - \mathcal{R}^*\big[\,\boldsymbol{w}|_{\Gamma_-}\,\big] = \boldsymbol{q}_\odot \quad \text{on} \quad \Gamma_+. \tag{4.27}$$

The adjoint-scattering operator is defined as,

$$\mathcal{Z}^*[\,\boldsymbol{w}\,](\boldsymbol{x},\boldsymbol{v}) = \frac{1}{4\pi}\int_{\mathbb{S}^2} \mathrm{d}S_{\boldsymbol{v}'}\,\boldsymbol{Z}(\boldsymbol{x},\boldsymbol{v}',\boldsymbol{v})^T\cdot\boldsymbol{w}(\boldsymbol{x},\boldsymbol{v}'), \tag{4.28}$$

for $(\boldsymbol{x}, \boldsymbol{v}) \in D \times \mathbb{S}^2$, and the adjoint-reflection operator as,

$$\mathcal{R}^*\big[\,\boldsymbol{w}|_{\Gamma_-}\,\big](\boldsymbol{x}, \boldsymbol{v}_+) = \frac{1}{2\pi} \int_{\boldsymbol{v}_- \cdot \nabla h(\boldsymbol{x}) < 0} \mathrm{d}S_{\boldsymbol{v}_-} |\boldsymbol{v}_- \cdot \nabla h(\boldsymbol{x})| \boldsymbol{R}(\boldsymbol{x}, \boldsymbol{v}_-, \boldsymbol{v}_+)^T \cdot \boldsymbol{w}(\boldsymbol{x}, \boldsymbol{v}_-), \tag{4.29}$$

for $(\boldsymbol{x}, \boldsymbol{v}_+) \in \Gamma_+$. Coupling with boundary conditions is imposed by spatial continuity along outgoing and incoming directions:

$$\boldsymbol{w}|_{\Gamma_+}(\boldsymbol{x}, \boldsymbol{v}_+) = \lim_{t \searrow 0} \boldsymbol{w}|_{D \times \mathbb{S}^2}(\boldsymbol{x} - t\boldsymbol{v}_+, \boldsymbol{v}_+), \tag{4.30}$$

$$\boldsymbol{w}|_{\Gamma_-}(\boldsymbol{x}, \boldsymbol{v}_-) = \lim_{t \searrow 0} \boldsymbol{w}|_{D \times \mathbb{S}^2}(\boldsymbol{x} + t\boldsymbol{v}_-, \boldsymbol{v}_-), \tag{4.31}$$

for $(\boldsymbol{x}, \boldsymbol{v}_+) \in \Gamma_+$ and $(\boldsymbol{x}, \boldsymbol{v}_-) \in \Gamma_-$.

Assuming existence and uniqueness for the moment, we conclude by defining the adjoint solution operator. For each parameter $\boldsymbol{a}$, the adjoint solution operator, $\mathcal{U}_{\boldsymbol{a}}^*$, maps adjoint source vectors, $\boldsymbol{p}_\odot$ and $\boldsymbol{q}_\odot$, to the adjoint Stokes vector on the internal and incoming sets:

$$\begin{Bmatrix} \boldsymbol{w}|_{D \times \mathbb{S}^2} \\ \boldsymbol{w}|_{\Gamma_-} \end{Bmatrix} = \mathcal{U}_{\boldsymbol{a}}^* \begin{Bmatrix} \boldsymbol{p}_\odot \\ \boldsymbol{q}_\odot \end{Bmatrix}. \tag{4.32}$$

The explicit form of this 2×2 matrix of integral operators is derived in Section 4.4.2.2 and given by Eq. (4.119).

Since the boundary value problems for the forward and adjoint 3D VRTE are defined independently, the adjoint property, $(\mathcal{U}_{\boldsymbol{a}})^* = \mathcal{U}_{\boldsymbol{a}}^*$, requires proof, and this is done in Theorem 4.4. In summary the forward 3D VRTE is stated in Definition 4.2 and can be

used to evaluate M radiometric measurements with $\mathcal{O}(L)$ calls to the forward solution operator, $\mathcal{U}_{\boldsymbol{a}}$. We asserted that the adjustment of atmosphere and surface properties would require evaluation of the left hand side of Eq. (4.25), and noted that this would require $\mathcal{O}(LN)$ calls to $\mathcal{U}_{\boldsymbol{a}}$. In section 4.3, we show how the left hand side of Eq. (4.25) arises naturally as the required quantity in an iterative search, and how evaluating with the adjoint alternative on the right-hand side of Eq. (4.25) leads to a scalable procedure for adjusting unknown parameters as part of a remote sensing algorithm. That is, one which requires only $\mathcal{O}(L)$ evaluations of the solution operators at each step, making the number of calls independent of the size of the problem.

4.3 Application to remote sensing

In the context of remote sensing of the Earth's 3D atmosphere and surface, the adjoint method provides a means of adjusting arbitrarily many atmosphere and surface parameters to improve their fit with arbitrarily many polarimetric measurements without changing the number of 3D VRTE simulations needed. To provide a concrete example of this, consider the task of retrieving cloud, aerosol, and surface properties for Yellowstone National Park which has a surface area of ten thousand km^2. For measurements, suppose we have access to a hundred satellite images of the park — taken with a single-spectral channel, from different perspectives, and with 1km resolution. These data provide one million constraints, $M = 1 \times 10^6$. Suppose also that a discretization of the atmosphere and surface is constructed with a total of one-thousand volume and surface elements, and

that the volume single-scattering and surface reflection properties are represented by an average of ten parameters per discrete element. These rough assumptions would result in the use of ten thousand parameters to describe the cloud, aerosol, and surface properties, $N = 1 \times 10^4$.

At each step in the retrieval algorithm we must adjust these ten thousand parameters to decrease the collective misfit with one million measurements. We note that if one were to linearize the measurement operator for this problem then the Jacobian matrix, consisting of elements $\partial y^m / \partial a^n$, would have ten billion entries. One of the key strategies of the method outlined here is to avoid the computation and storage of the Jacobian matrix, working instead with the misfit function and its gradient. Since the misfit function is scalar valued, its gradient in this case has only ten thousand elements. Even in this extreme example, the adjoint method described here provides a procedure for adjusting parameters to improve the collective fit with all data using only two calls to the 3D VRTE solver. For multi-wavelength data the required number of calls is $\mathcal{O}(L)$.

Although this example describes the scalability of the adjoint method using a futuristic application involving a full 3D reconstruction of cloud and aerosol properties, it is worth noting that this fits within a hierarchy of methods that start with retrievals assuming a plane-parallel atmosphere and with each pixel being an independent column [14, 59, 67]. This approach has been extended by Dubovik *et al.* [51] to include statistical modeling of the co-variation of atmospheric and surface properties in different pixels within the framework of a multi-pixel optimal estimation scheme. A natural addition to their usage of a multi-pixel prior probability distribution would be the usage of a

multi-pixel measurement operator, in which the 3D VRTE couples the radiative effects of nearby columns and allows, in the context of clear sky observations, for the proper account of adjacency effects. In this context, the adjoint method would provide a means of adjusting plane-parallel retrievals to correct for 3D, or adjacency effects. Moreover, the scalability result implies that the number of calls to the 3D VRTE solver is independent of the number of columns or pixels so that adjustments can be made to many pixels at once.

The remainder of Section 4.3 will summarize the methodology which makes this scalability possible. Qualitatively the adjoint method accomplishes this by associating the residual misfit between model and measurements with a single source distribution for the adjoint 3D VRTE. The residual for each individual image pixel is defined as the difference between model and observation, and is specific to the location of the instrument, the field of view of the pixel, and the sensitivity of the polarization analyzer. The weighted sum of these localized and directed residuals over all image pixels gives a single distribution of adjoint sources, and the adjoint 3D VRTE is solved to back-propagate this residual through all orders of multiple scattering. Then, simple integrals can be evaluated to determine the change in fit for all possible adjustments to the unknown parameters. This alternative way of thinking provides a rule for computing the misfit gradient with the desired scalability. The subsequent use of the misfit gradient in numerical optimization routines is discussed in Section 4.3.3, where each iterative adjustment to cloud, aerosol, and surface properties is written as a solution to an $N \times N$ system of linear equations.

4.3.1 Model for polarimetric measurements

The chosen setting for these results is the Earth's 3D atmospheric shell bounded between the Earth-atmosphere interface and an arbitrarily large radius out to space. The results extend to any smooth connected sub-region of interest, provided that reasonable horizontal boundary conditions are imposed. In the context of the radiative transfer model of light propagation, incoming solar radiation is scattered in the atmosphere and reflected by the surface, causing measurable radiative effects that vary with location, direction, and polarization.

To setup an abstract remote sensing problem, let $\hat{\boldsymbol{y}} = (\hat{y}^m)$ for $0 \leq m < M$ be a vector of single-wavelength multi-angle/multi-pixel polarimetric data taken by a ground, air, or space borne instrument. Let $\boldsymbol{a} = (a^n)$ for $0 \leq n < N$ be a vector of N unknown parameters which define a three-dimensional distribution of cloud, aerosol, and surface properties. In practice there will be constraints on the parameter vector, $\boldsymbol{a}$, to guarantee a reasonable physical interpretation (e.g. non-negative particle concentrations). Enforcing such constraints by finitely many linear equalities and convex inequalities is ideal, to give a numerically convenient description of the convex set of all possible states of the atmosphere and surface. We now describe in three steps, how the definitions of Section 4.2 lead to a useful model for polarimetric measurements of atmospheric radiation as they depend on cloud, aerosol, and surface properties.

First, the values of the volume-extinction coefficient, $\sigma(\boldsymbol{x}; \boldsymbol{a})$; the volume-scattering matrix, $\boldsymbol{Z}(\boldsymbol{x}, \boldsymbol{v}, \boldsymbol{v}'; \boldsymbol{a})$; and the surface-reflection matrix, $\boldsymbol{R}(\boldsymbol{x}, \boldsymbol{v}_-, \boldsymbol{v}_+; \boldsymbol{a})$, must be written

explicitly as smooth functions of the vector of parameters, $\boldsymbol{a}$. They must be smooth to guarantee the existence of derivatives, $\partial\sigma/\partial a^n$, $\partial\boldsymbol{Z}/\partial a^n$, and $\partial\boldsymbol{R}/\partial a^n$; and also to guarantee that the integral operators defined in Eqs. (4.46) and (4.47) will return square-integrable functions. Furthermore, for all feasible values of the parameter vector, the single-scattering properties must satisfy a solve-ability criteria given in Section 4.4 by Eq. (4.109). The parametrization of single-scattering properties incorporates both spatial and micro-physical variability. Surface reflection at the Earth-atmosphere boundary is characterized by several spatially dependent parameters. Volume-extinction and scattering properties are modeled as a linear combination of contributions from molecular scattering and various *modes* of airborne-particle. For each mode there are parameters that define loading, size distribution, shape, and complex refractive index. For the present discussion, we assume that there is a well-defined functional relationship between parameters and single-scattering properties, that the functions are smooth with respect to parameters, and that the single-scattering properties satisfy the solve-ability criteria.

Second, the 3D VRTE in Definition 4.2 is used to solve for the multiple scattering of incoming solar radiation and determine the Stokes vector solution, $\boldsymbol{u}(\boldsymbol{x},\boldsymbol{v};\boldsymbol{a})$. For each feasible parameter vector, $\boldsymbol{a}$, the method requires a solver, $\mathcal{U}_{\boldsymbol{a}}$, that acts on forward source vectors for solar illumination, $\boldsymbol{f}_\odot$ and $\boldsymbol{g}_\odot$, and returns the Stokes vector solution (restricted to the internal and outgoing sets):

$$\left\{ \begin{array}{c} \boldsymbol{u}|_{D\times\mathbb{S}^2} \\ \\ \boldsymbol{u}|_{\Gamma_+} \end{array} \right\} = \mathcal{U}_{\boldsymbol{a}} \left\{ \begin{array}{c} \boldsymbol{f}_\odot \\ \\ \boldsymbol{g}_\odot \end{array} \right\}. \tag{4.33}$$

The restrictions, $\boldsymbol{u}|_{D\times\mathbb{S}^2}$ and $\boldsymbol{u}|_{\Gamma_+}$, of the full Stokes vector solution, $\boldsymbol{u}$, provide all the information that is necessary to model multi-angle polarimetric measurements.

The third step involves expressing the measurable quantities which correspond to elements of the data vector, $\hat{\boldsymbol{y}}$, as inner products of the solution with detector response functions. Internal measurements are computed as the inner product of the internal Stokes vector, $\boldsymbol{u}|_{D\times\mathbb{S}^2}$, with a polarization analyzer defined on the internal set, $\boldsymbol{p}_{\odot}^{m}(\boldsymbol{x},\boldsymbol{v})$:

$$y^m(\boldsymbol{a}) = \left\langle \boldsymbol{p}_{\odot}^{m}, \boldsymbol{u} \right\rangle_{D\times\mathbb{S}^2} \quad \text{for} \quad 0 \leq m < M_1. \tag{4.34}$$

Outgoing measurements are computed as the inner product of the outgoing Stokes vector, $\boldsymbol{u}|_{\Gamma_+}$, with a polarization analyzer defined on the outgoing set, $\boldsymbol{q}_{\odot}^{m}(\boldsymbol{x},\boldsymbol{v}_+)$:

$$y^m(\boldsymbol{a}) = \left\langle \boldsymbol{q}_{\odot}^{m}, \boldsymbol{u}|_{\Gamma_+} \right\rangle_{\Gamma_+} \quad \text{for} \quad M_1 \leq m < M. \tag{4.35}$$

Given the clear apertures of typical Earth observing instruments we note that the polarization analyzers will be effectively Dirac-delta distributions in the location variable with angular integrations being determined by the field of view of the given sensor or pixel. While Dirac distributions are not square-integrable functions, they may be approximated as such to within discretization error. Aircraft measurements taken inside the domain result in a weight that is localized to a point in space:

$$\boldsymbol{p}_{\odot}^{m}(\boldsymbol{x},\boldsymbol{v}) \propto \delta(\boldsymbol{x}^m - \boldsymbol{x}). \tag{4.36}$$

For ground based instruments, e.g. AERONET [30], a natural route to computing measurements is to localize the position of the instrument to a point on the boundary:

$$\boldsymbol{q}_{\odot}^{m}(\boldsymbol{x}_{+},\boldsymbol{v}_{+}) \propto \frac{\delta(\boldsymbol{x}^{m}-\boldsymbol{x}_{+})}{|\boldsymbol{v}_{+}\cdot\nabla h(\boldsymbol{x}^{m})|}. \tag{4.37}$$

Satellite measurements may be taken at a great distance away from the domain, so in this case we suggest projecting the data to the outgoing boundary. This results in a weighting distribution that is singular in direction:

$$\boldsymbol{q}_{\odot}^{m}(\boldsymbol{x}_{+},\boldsymbol{v}_{+}) \propto \frac{\delta\left(\frac{\boldsymbol{x}^{m}-\boldsymbol{x}_{+}}{|\boldsymbol{x}^{m}-\boldsymbol{x}_{+}|}-\boldsymbol{v}_{+}\right)}{|\boldsymbol{v}_{+}\cdot\nabla h(\boldsymbol{x}_{+})|}. \tag{4.38}$$

Again, this singular distribution can be integrated over an actual instrument field of view in practice, with a scaling by the reciprocal, $|\boldsymbol{v}_{+}\cdot\nabla h(\boldsymbol{x}_{+})|^{-1}$, to counteract the weight that appears in the inner product $\langle\cdot,\cdot\rangle_{\Gamma_{+}}$. Internal measurements require no such scaling. In this way, the formalism used is shown to be consistent with common types of radiometric and polarimetric measurements taken of the atmosphere.

To summarize the process of modeling polarimetric measurements the three steps are as follows: (1) Single-scattering properties are written as smooth functions of N parameters that describe cloud, aerosol, and surface properties. (2) The Stokes vector solving the 3D VRTE is computed as a model for the spatially and directionally dependent field of radiative energy in the atmosphere. (3) Each individual polarimetric measurement is represented as an inner product of the internal or outgoing solution with a polarimetric

response function, defined on the same domain. This procedure provides the theoretical connection between observations and the retrieval target of atmospheric composition.

4.3.2 Data misfit and gradient calculation

In the abstract remote sensing problem, we aim to use multi-angle polarimetric data stored in the M-dimensional vector, $\hat{\boldsymbol{y}}$, to adjust the 3D atmosphere and surface parameters stored in the N-dimensional vector, $\boldsymbol{a}$, and reduce the measurement residual, $\hat{\boldsymbol{y}} - \boldsymbol{y}(\boldsymbol{a})$, to within measurement error. Using the instrument's measurement error covariance matrix, $\boldsymbol{S}_{\boldsymbol{\epsilon}}$, the misfit of model and data is quantified by the value of the *misfit function*:

$$\Phi(\boldsymbol{a}) = \frac{1}{2} \left(\hat{\boldsymbol{y}} - \boldsymbol{y}(\boldsymbol{a})\right)^T \cdot \boldsymbol{S}_{\boldsymbol{\epsilon}}^{-1} \cdot \left(\hat{\boldsymbol{y}} - \boldsymbol{y}(\boldsymbol{a})\right) \ . \tag{4.39}$$

To improve the fit we seek to adjust unknown parameters, $\boldsymbol{a}$, to decrease the value of the misfit function. The steepest decrease in Φ is obtained locally in the direction opposite the gradient, $\nabla\Phi$. The n^{th} element of this N-dimensional vector is given by the following formula:

$$-\frac{\partial \Phi(\boldsymbol{a})}{\partial a^n} = \left(\hat{\boldsymbol{y}} - \boldsymbol{y}(\boldsymbol{a})\right)^T \cdot \left(\boldsymbol{S}_{\boldsymbol{\epsilon}}^{-1}\right) \cdot \frac{\partial \boldsymbol{y}(\boldsymbol{a})}{\partial a^n} \ . \tag{4.40}$$

By differentiating Eqs. (4.34) and (4.35) with respect to parameter a^n and collecting terms into integration kernels for the internal and outgoing data, we write Eq. (4.40) as

a sum of inner products:

$$-\frac{\partial \Phi}{\partial a^n} = \left\langle \boldsymbol{\Delta p}_{\odot},\ \frac{\partial \boldsymbol{u}}{\partial a^n} \right\rangle_{D\times\mathbb{S}^2} + \left\langle \boldsymbol{\Delta q}_{\odot},\ \frac{\partial \boldsymbol{u}}{\partial a^n} \right\rangle_{\Gamma_+}. \tag{4.41}$$

The adjoint source vectors for differentiating the misfit function, $\boldsymbol{\Delta p}_{\odot}$ and $\boldsymbol{\Delta q}_{\odot}$, are obtained by summing over all detector response functions:

$$\boldsymbol{\Delta p}_{\odot}(\boldsymbol{x}, \boldsymbol{v};\ \boldsymbol{a}) = \sum_{0\le m'<M} \sum_{0\le m<M_1} \Big(\hat{y}^{m'} - y^{m'}(\boldsymbol{a})\Big)\ \left(\boldsymbol{S}_{\boldsymbol{\epsilon}}^{-1}\right)_{m'm}\ \boldsymbol{p}_{\odot}^{m}(\boldsymbol{x}, \boldsymbol{v}), \tag{4.42}$$

and,

$$\boldsymbol{\Delta q}_{\odot}(\boldsymbol{x}, \boldsymbol{v}_+;\ \boldsymbol{a}) = \sum_{0\le m'<M} \sum_{M_1\le m<M} \Big(\hat{y}^{m'} - y^{m'}(\boldsymbol{a})\Big)\ \left(\boldsymbol{S}_{\boldsymbol{\epsilon}}^{-1}\right)_{m'm}\ \boldsymbol{q}_{\odot}^{m}(\boldsymbol{x}, \boldsymbol{v}_+). \tag{4.43}$$

These adjoint source vectors, $\boldsymbol{\Delta p}_{\odot}$ and $\boldsymbol{\Delta q}_{\odot}$, may be visualized as collections of many "search lights" emanating from all measurement pixels at once, with the intensity of each search light equal to a weighted sum of the measurement residuals.

The next key step is to evaluate the derivative of the Stokes vector, $\partial \boldsymbol{u}/\partial a^n$. Although this could be accomplished numerically by finite-difference methods, a better way is to solve the 3D VRTE with modified volume-source and incoming-Stokes vectors. To see how this is possible, we differentiate Eqs. (4.16) and (4.17) with respect to parameter a^n

and obtain the following 3D VRTE for $\partial \boldsymbol{u}/\partial a^n$:

$$\boldsymbol{v} \cdot \nabla \frac{\partial \boldsymbol{u}}{\partial a^n} + \sigma \frac{\partial \boldsymbol{u}}{\partial a^n} - \mathcal{Z}\left[\frac{\partial \boldsymbol{u}}{\partial a^n} \right] = \boldsymbol{\Delta f}^n_{\odot}, \tag{4.44}$$

$$\frac{\partial \boldsymbol{u}}{\partial a^n}\Big|_{\Gamma_-} - \mathcal{R}\left[\frac{\partial \boldsymbol{u}}{\partial a^n}\Big|_{\Gamma_+} \right] = \boldsymbol{\Delta g}^n_{\odot}, \tag{4.45}$$

with right-hand sides equal to forward source vectors, $\boldsymbol{\Delta f}^n_{\odot}$ and $\boldsymbol{\Delta g}^n_{\odot}$. The *internal* source vector, $\boldsymbol{\Delta f}^n_{\odot}(\boldsymbol{x}, \boldsymbol{v})$ for $(\boldsymbol{x}, \boldsymbol{v}) \in D \times \mathbb{S}^2$, accounts for the change in extinction and scattering:

$$\boldsymbol{\Delta f}^n_{\odot}(\boldsymbol{x}, \boldsymbol{v};\, \boldsymbol{a}) = -\frac{\partial \sigma}{\partial a^n}(\boldsymbol{x};\boldsymbol{a})\; \boldsymbol{u}(\boldsymbol{x}, \boldsymbol{v};\, \boldsymbol{a}) + \frac{1}{4\pi} \int_{\mathbb{S}^2} \mathrm{d}S_{\boldsymbol{v}'}\; \frac{\partial \boldsymbol{Z}}{\partial a^n}(\boldsymbol{x}, \boldsymbol{v}, \boldsymbol{v}';\boldsymbol{a}) \cdot \boldsymbol{u}(\boldsymbol{x}, \boldsymbol{v}';\, \boldsymbol{a}). \tag{4.46}$$

And, the *incoming* source vector, $\boldsymbol{\Delta g}^n_{\odot}(\boldsymbol{x}, \boldsymbol{v}_-)$ for $(\boldsymbol{x}, \boldsymbol{v}_-) \in \Gamma_-$, accounts for the change in reflection:

$$\boldsymbol{\Delta g}^n_{\odot}(\boldsymbol{x}, \boldsymbol{v}_-;\, \boldsymbol{a}) = \frac{1}{2\pi} \int_{\boldsymbol{v}_+ \cdot \nabla h(\boldsymbol{x}) > 0} \mathrm{d}S_{\boldsymbol{v}_+}\, \left| \boldsymbol{v}_+ \cdot \nabla h(\boldsymbol{x}) \right|\, \frac{\partial \boldsymbol{R}}{\partial a^n}(\boldsymbol{x}, \boldsymbol{v}_-, \boldsymbol{v}_+;\boldsymbol{a}) \cdot \boldsymbol{u}(\boldsymbol{x}, \boldsymbol{v}_+;\, \boldsymbol{a}). \tag{4.47}$$

Comparing with Definition 4.2, we see that the left-hand side of the 3D VRTE for the gradient of the Stokes vector solution, $\partial \boldsymbol{u}/\partial a^n$, is identical to the left-hand side of the 3D VRTE of the solution itself, $\boldsymbol{u}$. Therefore the same existence and uniqueness results are applicable. If the forward source vectors for computing parameter derivatives are square-integrable then the solution operator returns the derivative of the Stokes vector

with respect to the parameter, a^n:

$$\left\{ \begin{array}{c} \frac{\partial \boldsymbol{u}}{\partial a^n}|_{D\times\mathbb{S}^2} \\ \\ \frac{\partial \boldsymbol{u}}{\partial a^n}|_{\Gamma_+} \end{array} \right\} = \mathcal{U}_{\boldsymbol{a}} \left\{ \begin{array}{c} \boldsymbol{\Delta f}^n_{\odot} \\ \\ \boldsymbol{\Delta g}^n_{\odot} \end{array} \right\}. \tag{4.48}$$

Substituting Eq. (4.48) into Eq. (4.41) we can express the equation for the gradient of the misfit function as,

$$-\frac{\partial \Phi}{\partial a^n} = \left\langle \left\{ \begin{array}{c} \boldsymbol{\Delta p}_{\odot} \\ \\ \boldsymbol{\Delta q}_{\odot} \end{array} \right\}, \mathcal{U}_{\boldsymbol{a}} \left\{ \begin{array}{c} \boldsymbol{\Delta f}^n_{\odot} \\ \\ \boldsymbol{\Delta g}^n_{\odot} \end{array} \right\} \right\rangle_{D\times\mathbb{S}^2\oplus\Gamma_+}, \tag{4.49}$$

for each a^n with $0 \leq n < N$. As written in Eq. (4.49), computing all elements of the gradient requires N solutions to a 3D VRTE solver at each step of a multi-step iterative procedure.

However, the alternative rule for computing the gradient with the adjoint 3D VRTE is analytically equivalent to Eq. (4.49), but requires only one additional call to a 3D VRTE simulation, independent of how many parameters are used. The adjoint rule for differentiating the misfit function is as follows:

$$-\frac{\partial \Phi}{\partial a^n} = \left\langle (\mathcal{U}_{\boldsymbol{a}})^* \left\{ \begin{array}{c} \boldsymbol{\Delta p}_{\odot} \\ \\ \boldsymbol{\Delta q}_{\odot} \end{array} \right\}, \left\{ \begin{array}{c} \boldsymbol{\Delta f}^n_{\odot} \\ \\ \boldsymbol{\Delta g}^n_{\odot} \end{array} \right\} \right\rangle_{D\times\mathbb{S}^2\oplus\Gamma_-}. \tag{4.50}$$

Using the fundamental adjoint property, $(\mathcal{U}_{\boldsymbol{a}})^* = \mathcal{U}^*_{\boldsymbol{a}}$, which is proven in Section 4.4.3 as Theorem 4.4, along with Eq. (4.32); the gradient can be written in terms of the adjoint

Stokes vector, $\boldsymbol{w}$, solving the adjoint 3D VRTE with adjoint source vectors, $\boldsymbol{\Delta p}_\odot$ and $\boldsymbol{\Delta q}_\odot$:

$$-\frac{\partial \Phi}{\partial a^n} = \left\langle \mathcal{U}_{\boldsymbol{a}}^* \begin{Bmatrix} \boldsymbol{\Delta p}_\odot \\ \boldsymbol{\Delta q}_\odot \end{Bmatrix}, \begin{Bmatrix} \boldsymbol{\Delta f}_\odot^n \\ \boldsymbol{\Delta g}_\odot^n \end{Bmatrix} \right\rangle_{D\times\mathbb{S}^2\oplus\Gamma_-} , \tag{4.51}$$

$$= \left\langle \boldsymbol{w}, \boldsymbol{\Delta f}_\odot^n \right\rangle_{D\times\mathbb{S}^2} + \left\langle \boldsymbol{w}, \boldsymbol{\Delta g}_\odot^n \right\rangle_{\Gamma_-} . \tag{4.52}$$

The significance of Eqs. (4.51) and (4.52) is that the adjoint solution, $\boldsymbol{w}$, is independent of which a^n appears in the differentiation. Therefore any component of the gradient can be evaluated with the same adjoint solution, $\boldsymbol{w}$, and without further calls to a radiative transfer solver. The procedure involves the comparatively inexpensive operations of weighting the adjoint solution with the source terms from Eqs. (4.46) and (4.47), and integrating over the internal and incoming sets. The computation time of these integrations is (at worst) comparable to a single order-of-scattering computation, and could be much faster if one is careful to use a sparse basis for spatial and directional variability.

Using the adjoint method to compute the gradient of the misfit function shifts all the multiple-scattering computations to the residual distribution which depends only on the current atmospheric state and the misfit between observations and the polarized radiance that is generated by the current atmospheric state. The number of solutions to the 3D VRTE required in evaluating Eqs. (4.51) and (4.52) is $\mathcal{O}(L)$ and independent of the number of parameters, N. Therefore, rules for adjusting cloud, aerosol, and surface parameters based on the adjoint calculation of the misfit gradient are scalable to retrieval

problems with many measurements and unknown parameters.

4.3.3 Iterative parameter adjustment

To discuss how the adjoint computations of the gradient of the misfit function can be incorporated into a scalable retrieval algorithm, we define a regularized misfit function, Φ_{reg}:

$$\Phi_{\text{reg}}(\boldsymbol{a}) = \Phi(\boldsymbol{a}) \; + \; \Phi_{\text{prior}}(\boldsymbol{a}). \tag{4.53}$$

Prior information is introduced by, Φ_{prior}, to give a new maximum-likelihood estimation problem which is less sensitive to measurement noise and to provide a means of imposing additional measurement constraints, for example those from a coordinated LIDAR instrument [26, 60]. The retrieval starts with an initial guess, $\boldsymbol{a}_0$, and makes additive adjustments, $\boldsymbol{b}_k$, so that the updated parameter, $\boldsymbol{a}_{k+1} = \boldsymbol{a}_k + \boldsymbol{b}_k$, converges to a minimizer of the regularized misfit function, Φ_{reg}.

A common starting place for many optimization methods is the second order Taylor approximation for, Φ_{reg}, about any feasible state, $\boldsymbol{a}$:

$$\tilde{\Phi}_{\text{reg}}(\boldsymbol{a}+\boldsymbol{b}) = \Phi_{\text{reg}}(\boldsymbol{a}) \; + \; \nabla\Phi_{\text{reg}}(\boldsymbol{a}) \cdot \boldsymbol{b} \; + \; \frac{1}{2}\, \boldsymbol{b}^T \cdot \nabla\nabla\Phi_{\text{reg}}(\boldsymbol{a}) \cdot \boldsymbol{b}. \tag{4.54}$$

With sufficient prior information the Hessian matrix, $\nabla\nabla\Phi_{\text{reg}}(\boldsymbol{a})$, can be made positive definite. In this case the minimum value of the Taylor approximation can be found by

solving Newton's equation for step, $\boldsymbol{b}$:

$$\left(\nabla\nabla\Phi(\boldsymbol{a}) + \nabla\nabla\Phi_{\text{prior}}(\boldsymbol{a})\right) \cdot \boldsymbol{b} = -\left(\nabla\Phi(\boldsymbol{a}) + \nabla\Phi_{\text{prior}}(\boldsymbol{a})\right). \tag{4.55}$$

A common scenario in setting up Newton's equations, is that the Hessian of the prior function is easy to compute and the Hessian of the measurement misfit function is prohibitively expensive. Quasi-Newton methods substitute an approximate Hessian.

In atmospheric remote sensing applications, methods such as Levenberg-Marquardt use a linearized measurement model to approximate the Hessian in terms of the Jacobian matrix [26, 51, 59]. The Jacobian matrix,

$$\boldsymbol{J}(\boldsymbol{a}_k) = \frac{\partial \boldsymbol{y}(\boldsymbol{a}_k)}{\partial \boldsymbol{a}}, \tag{4.56}$$

is computed at every step, to approximate the Hessian as follows:

$$\nabla\nabla\Phi(\boldsymbol{a}) \approx \boldsymbol{J}(\boldsymbol{a})^T \cdot \boldsymbol{J}(\boldsymbol{a}). \tag{4.57}$$

The Jacobian matrix contains the derivatives of measurements with respect to unknown parameters and is, in general, dense with $\mathcal{O}(MN)$ elements. Using the fundamental adjoint property, the inner product for each element may be written in either of two

forms: one using the forward solver,

$$\frac{\partial y^m}{\partial a^n} = \left\langle \begin{Bmatrix} \boldsymbol{p}_{\odot}^m \\ \boldsymbol{q}_{\odot}^m \end{Bmatrix}, \mathcal{U}_{\boldsymbol{a}} \begin{Bmatrix} \boldsymbol{\Delta f}_{\odot}^n \\ \boldsymbol{\Delta g}_{\odot}^n \end{Bmatrix} \right\rangle_{D \times \mathbb{S}^2 \oplus \Gamma_+}, \tag{4.58}$$

and the other using the adjoint solver,

$$\frac{\partial y^m}{\partial a^n} = \left\langle \mathcal{U}_{\boldsymbol{a}}^* \begin{Bmatrix} \boldsymbol{p}_{\odot}^m \\ \boldsymbol{q}_{\odot}^m \end{Bmatrix}, \begin{Bmatrix} \boldsymbol{\Delta f}_{\odot}^n \\ \boldsymbol{\Delta g}_{\odot}^n \end{Bmatrix} \right\rangle_{D \times \mathbb{S}^2 \oplus \Gamma_-}. \tag{4.59}$$

In Eq. (4.58) the forward solution operator, $\mathcal{U}_{\boldsymbol{a}}$, must be evaluated for each different parameter and wavelength and this results in $\mathcal{O}(LN)$ computations. If the number of parameters is small or the computational solver provides the Green's functions, then Eq. (4.58) can be quite efficient, see for example [70, 73], but codes which currently solve the 3D VRTE do not compute the Green's functions. In the alternative rule given by Eq. (4.59) the adjoint solution operator, $\mathcal{U}_{\boldsymbol{a}}^*$, must be evaluated for each measurement and this results in $\mathcal{O}(M)$ computations. However, it is worth mentioning that alternative approaches use the single-scattering approximation to formulate an approximate, sparse Jacobian matrix. This idea has shown promise for retrieving the volume-scattering coefficient, σ, using the scalar 3D radiative transfer equation with isotropic and weakly scattering media [84].

To handle the large amount of multiple scattering in clouds, we considered another quasi-Newton method which approximates the Hessian of the measurement misfit function

using the gradient of the misfit function, $\nabla\Phi$, at previous iterations. These *gradient-based* methods can take advantage of the scalability of the adjoint rule in Eq. (4.50). The Hessian of the misfit function is approximated using previous parameter estimates, $\boldsymbol{a}_k$, and previous gradients, $\nabla\Phi(\boldsymbol{a}_k)$. The approximate Hessian, $\boldsymbol{H}_k$, is updated and improved upon at each step:

$$\nabla\nabla\Phi(\boldsymbol{a}_k) \approx \boldsymbol{H}_k\left(\boldsymbol{a}_0, \cdots, \boldsymbol{a}_k, \nabla\Phi(\boldsymbol{a}_0), \cdots, \nabla\Phi(\boldsymbol{a}_k)\right). \tag{4.60}$$

The rule usually guarantees symmetry and non-negative definiteness, and this is the case for the Broyden-Fletcher-Goldfarb-and-Shanno method, which is used in the medical imaging applications [20, 65, 66]. With a positive definite prior Hessian matrix $\nabla\nabla\Phi_{\text{prior}}$, the approximate Newton's equation uniquely defines a parameter adjustment, $\boldsymbol{b}_k$, with the following linear system:

$$\left(\boldsymbol{H}_k + \nabla\nabla\Phi_{\text{prior}}(\boldsymbol{a}_k)\right)\cdot\boldsymbol{b} = -\ \left(\nabla\Phi(\boldsymbol{a}_k) + \nabla\Phi_{\text{prior}}(\boldsymbol{a}_k)\right). \tag{4.61}$$

Provided that the problem is well scaled and that the approximate Hessian, $\boldsymbol{H}_k$, is chosen appropriately, the step will result in an improved set of cloud, aerosol and surface properties via the updated parameter $\boldsymbol{a}_{k+1} = \boldsymbol{a}_k + \boldsymbol{b}_k$. Moreover, by using the gradient, $\nabla\Phi$, to set up the local problem, the method can leverage the scalability of the adjoint computation to adjust atmosphere and surface properties with only $\mathcal{O}(L)$ calls to a 3D VRTE solver at each step.

4.3.4 Pseudo-forward problem

This section describes how to solve the adjoint 3D VRTE using a computer simulation for solving the forward 3D VRTE. To do this we must define two *actions*, α and $\boldsymbol{Q}$, which transform vectors according to the following rules. Action by α changes the sign of the direction argument:

$$\alpha \boldsymbol{f}(\boldsymbol{x}, \boldsymbol{v}) = \boldsymbol{f}(\boldsymbol{x}, -\boldsymbol{v}). \tag{4.62}$$

Action by $\boldsymbol{Q}$ flips the orientation of circular polarization:

$$\boldsymbol{Q}\boldsymbol{f}(\boldsymbol{x}, \boldsymbol{v}) = \begin{bmatrix} 1 & & & \\ & 1 & & \\ & & 1 & \\ & & & -1 \end{bmatrix} \cdot \begin{bmatrix} f_I(\boldsymbol{x}, \boldsymbol{v}) \\ f_Q(\boldsymbol{x}, \boldsymbol{v}) \\ f_U(\boldsymbol{x}, \boldsymbol{v}) \\ f_V(\boldsymbol{x}, \boldsymbol{v}) \end{bmatrix}. \tag{4.63}$$

These actions are their own inverses, $\boldsymbol{Q}^2 = \alpha^2 = \text{Identity}$.

For scattering media which obeys the principles of mirror-symmetry and reciprocity, the kernel for the single-scattering operator satisfies the rule,

$$\boldsymbol{Z}^T(\boldsymbol{x}, \boldsymbol{v}', \boldsymbol{v}) = \boldsymbol{Q}\boldsymbol{Z}(\boldsymbol{x}, -\boldsymbol{v}, -\boldsymbol{v}')\boldsymbol{Q}, \tag{4.64}$$

and the kernel for the reflection operator satisfies the rule,

$$\boldsymbol{R}^T(\boldsymbol{x}, \boldsymbol{v}', \boldsymbol{v}) = \boldsymbol{Q}\boldsymbol{R}(\boldsymbol{x}, -\boldsymbol{v}, -\boldsymbol{v}')\boldsymbol{Q}. \tag{4.65}$$

The adjoint scattering operator can be written in terms of the forward scattering operator,

$$\mathcal{Z}^*[\boldsymbol{w}] = \alpha\boldsymbol{Q}\mathcal{Z}[\alpha\boldsymbol{Q}\boldsymbol{w}], \tag{4.66}$$

and the adjoint reflection operator can be written in terms of the forward reflection operator,

$$\mathcal{R}^*[\boldsymbol{w}] = \alpha\boldsymbol{Q}\,\mathcal{R}[\alpha\boldsymbol{Q}\boldsymbol{w}]. \tag{4.67}$$

By plugging Eqs. (4.66) and (4.67) into the adjoint 3D VRTE defined by Eqs. (4.26) and (4.27) and acting on both sides with $\alpha\boldsymbol{Q}$, it is easy to verify that the transformed adjoint Stokes vector, $\alpha\boldsymbol{Q}\boldsymbol{w}$, solves the forward 3D VRTE with pseudo-forward source vectors, $\alpha\boldsymbol{Q}\boldsymbol{p}_\odot$ and $\alpha\boldsymbol{Q}\boldsymbol{q}_\odot$. Therefore, the adjoint solution operator, can be evaluated using the forward solution operator as follows:

$$\mathcal{U}_{\boldsymbol{a}}^* \left\{ \begin{array}{c} \boldsymbol{p}_\odot \\ \\ \boldsymbol{q}_\odot \end{array} \right\} = \alpha\boldsymbol{Q}\mathcal{U}_{\boldsymbol{a}} \left\{ \begin{array}{c} \alpha\boldsymbol{Q}\boldsymbol{p}_\odot \\ \\ \alpha\boldsymbol{Q}\boldsymbol{q}_\odot \end{array} \right\}. \tag{4.68}$$

This means that a computer code that solves the forward problem can be used to solve the adjoint problem. Provided that it is sufficiently general to accept the transformed

source vectors, $\alpha \boldsymbol{Q}\boldsymbol{p}_{\odot}$ and $\alpha \boldsymbol{Q}\boldsymbol{q}_{\odot}$, it will output as a solution the transformed adjoint Stokes vector, $\alpha \boldsymbol{Q}\boldsymbol{w}$. The only additional difficulties in solving for the adjoint solution, $\boldsymbol{w}$, arise in preparing the right-hand side and interpreting the solution.

4.4 Derivation of the fundamental adjoint property

This section defines mathematical tools for proving the fundamental adjoint property with the proof given in Section 4.4.3. The first objective is to define a family of streaming operators. These will enable the formulation of integral equations which are equivalent to the integro-differential equations of 3D VRT, as given by Definitions 4.2 and 4.3 in Section 4.2. The integral equations are presented in Sections 4.4.2.1 and 4.4.2.2, along with series expansions for the solution operators, $\mathcal{U}_{\boldsymbol{a}}$ and $\mathcal{U}_{\boldsymbol{a}}^{*}$. Lastly, in Section 4.4.3 we state and prove the fundamental adjoint property as Theorem 4.4. This theorem shows that the adjoint 3D VRTE given in Definition 4.3 is well defined, that $(\mathcal{U}_{\boldsymbol{a}})^{*} = \mathcal{U}_{\boldsymbol{a}}^{*}$, and justifies the use of this property in deriving a scalable procedure for adjusting 3D atmosphere and surface parameters.

4.4.1 The streaming operators

Streaming refers to propagation of radiative information along special line segments called chords[1]. *Chords* are defined to be the open-ended line segments in D whose endpoints lie on the boundary, ∂D. The streaming operators propagate source vectors along these

[1]also called characteristics

chords: forward streaming operators propagate sources in the positive direction, $\boldsymbol{v}$, and adjoint streaming operators propagate sources in the negative direction, $-\boldsymbol{v}$. In contrast to previous derivations of the ancillary integral equation for 3D radiative transfer, for example that by Davis and Knyazikhin in Chapter 3 of [62], we split the streaming process into four distinct linear operations. This splitting facilitates the treatment of general boundary conditions in both the forward and adjoint 3D VRTE. Moreover, the streaming operators for the adjoint 3D VRTE are, actually, the adjoint operators of the forward streaming operators. A brief summary of the splitting of streaming operators will suffice for readers wishing to move ahead to Section 4.4.2 and the definition of the integral equations for 3D VRTE.

Each streaming operator acts on, and returns, a function which is defined on one of the three subdomains of vector radiative transfer. For instance, the *internal* streaming operator, $\mathcal{T}_{00}$, acts on an internal source vector, $\boldsymbol{f}$, defined on the internal set, $D \times \mathbb{S}^2$, and it returns a Stokes vector restricted to the internal set, $\boldsymbol{u}|_{D\times\mathbb{S}^2}$. Boundary conditions are managed by the other operators. The *incoming-to-internal* streaming operator, $\mathcal{T}_{-0}$, acts on an incoming source vector, $\boldsymbol{g}$, defined on the incoming set, Γ_-, and it returns a Stokes vector on the internal set, $\boldsymbol{u}|_{D\times\mathbb{S}^2}$. The other two forward streaming operators are named according to their behavior in a similar way. The *internal-to-outgoing* streaming operator, $\mathcal{T}_{0+}$, acts on an internal source vector, $\boldsymbol{f}$, and returns an outgoing Stokes vector, $\boldsymbol{u}|_{\Gamma_+}$; and the *incoming-to-outgoing* streaming operator, $\mathcal{T}_{-+}$, acts on an incoming source vector, $\boldsymbol{g}$, and returns an outgoing Stokes vector, $\boldsymbol{u}|_{\Gamma_+}$.

The adjoints of these streaming operators act on adjoint source vectors and return adjoint

Stokes vectors. For instance, the adjoint of the *internal* streaming operator, $\mathcal{T}^*_{00}$, acts on an internal adjoint source vector, $\boldsymbol{p}$, defined on the internal set, $D \times \mathbb{S}^2$, and it returns an adjoint Stokes vector restricted to the internal set, $\boldsymbol{w}|_{D\times\mathbb{S}^2}$. However, the domains of input and output functions are reversed: The adjoint of the *incoming-to-internal* streaming operator, $\mathcal{T}^*_{-0}$, acts on an internal-adjoint source vector, $\boldsymbol{p}$, and returns an incoming-adjoint Stokes vector, $\boldsymbol{w}|_{\Gamma_-}$; the adjoint of the *internal-to-outgoing* streaming operator, $\mathcal{T}^*_{0+}$, acts on an outgoing-adjoint source vector, $\boldsymbol{q}$, and returns an internal-adjoint Stokes vector, $\boldsymbol{w}|_{D\times\mathbb{S}^2}$; and the adjoint of the *incoming-to-outgoing* streaming operator, $\mathcal{T}^*_{-+}$, acts on an outgoing adjoint source vector, $\boldsymbol{q}$, and returns an incoming adjoint Stokes vector, $\boldsymbol{w}|_{\Gamma_-}$.

Adjoint streaming operators are defined to satisfy the following adjoint properties:

$$\Big\langle \boldsymbol{p}, \mathcal{T}_{00}[\,\boldsymbol{f}\,] \Big\rangle_{D\times\mathbb{S}^2} = \Big\langle \mathcal{T}^*_{00}[\,\boldsymbol{p}\,], \boldsymbol{f} \Big\rangle_{D\times\mathbb{S}^2}, \tag{4.69}$$

$$\Big\langle \boldsymbol{q}, \mathcal{T}_{0+}[\,\boldsymbol{f}\,] \Big\rangle_{\Gamma_+} = \Big\langle \mathcal{T}^*_{0+}[\,\boldsymbol{q}\,], \boldsymbol{f} \Big\rangle_{D\times\mathbb{S}^2}, \tag{4.70}$$

$$\Big\langle \boldsymbol{p}, \mathcal{T}_{-0}[\,\boldsymbol{g}\,] \Big\rangle_{D\times\mathbb{S}^2} = \Big\langle \mathcal{T}^*_{-0}[\,\boldsymbol{p}\,], \boldsymbol{g} \Big\rangle_{\Gamma_-}, \tag{4.71}$$

$$\Big\langle \boldsymbol{q}, \mathcal{T}_{-+}[\,\boldsymbol{g}\,] \Big\rangle_{\Gamma_+} = \Big\langle \mathcal{T}^*_{-+}[\,\boldsymbol{q}\,], \boldsymbol{g} \Big\rangle_{\Gamma_-}. \tag{4.72}$$

The remainder of Section 4.4.1 is devoted to parameterizing chords for the purpose of defining explicit rules for evaluating each of the forward and adjoint streaming operators. Forward streaming operators are defined in Eqs. (4.89) - (4.92), and their adjoints in Eqs. (4.93) - (4.96). In B.2 we prove the adjoint properties of the streaming operators.

4.4.1.1 Chords and boundary points

Because streaming operators propagate information along chords, they are most easily defined with a chord parametrization. The signed distance-to-boundary function, $h(\boldsymbol{x})$, is quite useful for this purpose and enables treatment of non-convex atmospheric regions and surface topography. Using this function we define the unique chord for every internal, incoming, and outgoing point.

For internal points, $(\boldsymbol{x}, \boldsymbol{v}) \in D \times \mathbb{S}^2$, we define the chord parameters as follows:

$$t = \boldsymbol{x} \cdot \boldsymbol{v}, \tag{4.73}$$

$$\boldsymbol{x}^{\perp} = \boldsymbol{x} - t\boldsymbol{v}. \tag{4.74}$$

Extreme values of chord parameter, t, are found by looking along the directions, $\boldsymbol{v}$ and $-\boldsymbol{v}$, to the nearest boundary points:

$$t_- = \max\left\{t_- \in \mathbb{R} \,:\, t_- < t \text{ and } h(\boldsymbol{x}^{\perp} + t_-\boldsymbol{v}) = 0 \right\}, \tag{4.75}$$

$$t_+ = \min\left\{t_+ \in \mathbb{R} \,:\, t_+ > t \text{ and } h(\boldsymbol{x}^{\perp} + t_+\boldsymbol{v}) = 0 \right\}. \tag{4.76}$$

For outgoing points, $(\boldsymbol{x}, \boldsymbol{v}_+) \in \Gamma_+$, the chord parameters are defined as follows:

$$t_+ = \boldsymbol{x} \cdot \boldsymbol{v}_+, \tag{4.77}$$

$$\boldsymbol{x}^{\perp} = \boldsymbol{x} - t_+\boldsymbol{v}_+. \tag{4.78}$$

The opposite extreme is found by looking along, $-\boldsymbol{v}_+$, to the nearest boundary point:

$$t_- = \max\left\{t_- \in \mathbb{R} \,:\, t_- < t_+ \text{ and } h(\boldsymbol{x}^\perp + t_-\boldsymbol{v}_+) = 0 \right\}. \tag{4.79}$$

For incoming points, $(\boldsymbol{x}, \boldsymbol{v}_-) \in \Gamma_-$, the chord parameters are defined as follows:

$$t_- = \boldsymbol{x} \cdot \boldsymbol{v}_-, \tag{4.80}$$

$$\boldsymbol{x}^\perp = \boldsymbol{x} - t_-\boldsymbol{v}_-. \tag{4.81}$$

The opposite extreme is found by looking along, $\boldsymbol{v}_-$, to the nearest boundary point:

$$t_+ = \min\left\{t_+ \in \mathbb{R} \,:\, t_+ > t_- \text{ and } h(\boldsymbol{x}^\perp + t_+\boldsymbol{v}_-) = 0 \right\}. \tag{4.82}$$

In each case, the position-direction pair can be associated with the unique non-empty chord,

$$\boldsymbol{x}'(t'; \boldsymbol{x}^\perp, \boldsymbol{v}) = \boldsymbol{x}^\perp + t'\boldsymbol{v} \quad \text{for} \quad t_- < t' < t_+, \tag{4.83}$$

through the interior, with $h(\boldsymbol{x}'(t')) < 0$. The endpoints of the chord correspond to parameters, t_- and t_+,

$$\boldsymbol{x}_- = \boldsymbol{x}^\perp + t_-\boldsymbol{v} \quad \in \partial D, \tag{4.84}$$

$$\boldsymbol{x}_+ = \boldsymbol{x}^\perp + t_+\boldsymbol{v} \quad \in \partial D, \tag{4.85}$$

and are on the boundary, since $h(\boldsymbol{x}_-) = h(\boldsymbol{x}_+) = 0$. This defines the chord representation for all points in the domain of 3D VRTE and provides a useful alternative representations of internal, outgoing, and incoming points:

$$(\boldsymbol{x}, \boldsymbol{v}) = (\boldsymbol{x}^\perp + t\boldsymbol{v}, \boldsymbol{v}), \tag{4.86}$$

$$(\boldsymbol{x}, \boldsymbol{v}_+) = (\boldsymbol{x}^\perp + t_+\boldsymbol{v}_+, \boldsymbol{v}_+), \tag{4.87}$$

$$(\boldsymbol{x}, \boldsymbol{v}_-) = (\boldsymbol{x}^\perp + t_-\boldsymbol{v}_-, \boldsymbol{v}_-). \tag{4.88}$$

Looking toward future work implementing numerical methods, it is worth noting that this procedure can find chords through complex geometries by determining the zeros of a real-valued, single-variable function: $h(\boldsymbol{x}'(\cdot))$.

There is an important caveat. Although the chord is uniquely defined for each case, the endpoints, $\boldsymbol{x}_-$ and $\boldsymbol{x}_+$, do not always correspond to elements in the incoming or outgoing sets. The reason for this is that some chords will be tangent to the boundary at one or both end points. This poses a challenge to defining boundary-streaming operators, because there is not necessarily an incoming or outgoing point that corresponds to a location at which we desire to know the value of the streaming operator. However, the set of such points related to boundary-tangent chords will have measure zero in the integrals of interest and can therefore be neglected. We now focus on defining the streaming operators, noting that certain points that correspond to chords that are tangent to the boundary may require alternate definitions.

4.4.1.2 Rules for evaluating streaming operators

Streaming operators are defined by changing the argument of evaluation from standard representation to chord representation, e.g. from $(\boldsymbol{x}, \boldsymbol{v})$ to $(\boldsymbol{x}^{\perp} + t\boldsymbol{v}, \boldsymbol{v})$. This is done to isolate the direction, $\boldsymbol{v}$, along which source vectors are integrated. The four forward streaming operators are defined as follows:

$$\begin{aligned}\mathcal{T}_{00}[\,\boldsymbol{f}\,](\boldsymbol{x}, \boldsymbol{v}) &= \mathcal{T}_{00}[\,\boldsymbol{f}\,](\boldsymbol{x}^{\perp} + t\boldsymbol{v}, \boldsymbol{v}), \\ &= \int_{t_-}^{t} \mathrm{d}t' \left[\exp\left(- \int_{t'}^{t} \mathrm{d}t'' \sigma(\boldsymbol{x}^{\perp} + t''\boldsymbol{v}) \right) \boldsymbol{f}(\boldsymbol{x}^{\perp} + t'\boldsymbol{v}, \boldsymbol{v}) \right], \end{aligned} \tag{4.89}$$

$$\begin{aligned}\mathcal{T}_{0+}[\,\boldsymbol{f}\,](\boldsymbol{x}_+, \boldsymbol{v}_+) &= \mathcal{T}_{0+}[\,\boldsymbol{f}\,](\boldsymbol{x}^{\perp} + t_+\boldsymbol{v}, \boldsymbol{v}), \\ &= \int_{t_-}^{t_+} \mathrm{d}t' \left[\exp\left(- \int_{t'}^{t_+} \mathrm{d}t'' \sigma(\boldsymbol{x}^{\perp} + t''\boldsymbol{v}) \right) \boldsymbol{f}(\boldsymbol{x}^{\perp} + t'\boldsymbol{v}, \boldsymbol{v}) \right], \end{aligned} \tag{4.90}$$

$$\begin{aligned}\mathcal{T}_{-0}[\,\boldsymbol{g}\,](\boldsymbol{x}, \boldsymbol{v}) &= \mathcal{T}_{-0}[\,\boldsymbol{g}\,](\boldsymbol{x}^{\perp} + t\boldsymbol{v}, \boldsymbol{v}), \\ &= \exp\left(- \int_{t_-}^{t} \mathrm{d}t'' \sigma(\boldsymbol{x}^{\perp} + t''\boldsymbol{v}) \right) \boldsymbol{g}(\boldsymbol{x}^{\perp} + t_-\boldsymbol{v}, \boldsymbol{v}), \end{aligned} \tag{4.91}$$

$$\begin{aligned}\mathcal{T}_{-+}[\,\boldsymbol{g}\,](\boldsymbol{x}_+, \boldsymbol{v}_+) &= \mathcal{T}_{-+}[\,\boldsymbol{g}\,](\boldsymbol{x}^{\perp} + t_+\boldsymbol{v}, \boldsymbol{v}), \\ &= \exp\left(- \int_{t_-}^{t_+} \mathrm{d}t'' \sigma(\boldsymbol{x}^{\perp} + t''\boldsymbol{v}) \right) \boldsymbol{g}(\boldsymbol{x}^{\perp} + t_-\boldsymbol{v}, \boldsymbol{v}). \end{aligned} \tag{4.92}$$

The adjoints of these operators are given by the rules:

$$\begin{aligned}\mathcal{T}^*_{00}[\boldsymbol{p}](\boldsymbol{x},\boldsymbol{v}) &= \mathcal{T}^*_{00}[\boldsymbol{p}](\boldsymbol{x}^\perp + t\boldsymbol{v},\boldsymbol{v}),\\ &= \int_t^{t_+} \mathrm{d}t' \left[\exp\left(-\int_t^{t'} \mathrm{d}t'' \sigma(\boldsymbol{x}^\perp + t''\boldsymbol{v}) \right) \boldsymbol{p}(\boldsymbol{x}^\perp + t'\boldsymbol{v},\boldsymbol{v}) \right], \end{aligned} \tag{4.93}$$

$$\begin{aligned}\mathcal{T}^*_{0+}[\boldsymbol{q}](\boldsymbol{x},\boldsymbol{v}) &= \mathcal{T}^*_{0+}[\boldsymbol{q}](\boldsymbol{x}^\perp + t\boldsymbol{v},\boldsymbol{v}),\\ &= \exp\left(-\int_t^{t_+} \mathrm{d}t'' \sigma(\boldsymbol{x}^\perp + t''\boldsymbol{v}) \right) \boldsymbol{q}(\boldsymbol{x}^\perp + t_+\boldsymbol{v},\boldsymbol{v}), \end{aligned} \tag{4.94}$$

$$\begin{aligned}\mathcal{T}^*_{-0}[\boldsymbol{p}](\boldsymbol{x}_-,\boldsymbol{v}_-) &= \mathcal{T}^*_{-0}[\boldsymbol{p}](\boldsymbol{x}^\perp + t_-\boldsymbol{v},\boldsymbol{v}),\\ &= \int_{t_-}^{t_+} \mathrm{d}t' \left[\exp\left(-\int_{t_-}^{t'} \mathrm{d}t'' \sigma(\boldsymbol{x}^\perp + t''\boldsymbol{v}) \right) \boldsymbol{p}(\boldsymbol{x}^\perp + t'\boldsymbol{v},\boldsymbol{v}) \right], \end{aligned} \tag{4.95}$$

$$\begin{aligned}\mathcal{T}^*_{-+}[\boldsymbol{q}](\boldsymbol{x}_-,\boldsymbol{v}_-) &= \mathcal{T}^*_{-+}[\boldsymbol{q}](\boldsymbol{x}^\perp + t_-\boldsymbol{v},\boldsymbol{v}),\\ &= \exp\left(-\int_{t_-}^{t_+} \mathrm{d}t'' \sigma(\boldsymbol{x}^\perp + t''\boldsymbol{v}) \right) \boldsymbol{q}(\boldsymbol{x}^\perp + t_+\boldsymbol{v},\boldsymbol{v}). \end{aligned} \tag{4.96}$$

The streaming operators in Eqs. (4.89), (4.90), (4.93), and (4.95) act on internal source vectors, $\boldsymbol{f}$ or $\boldsymbol{p}$, and require integration over some or all of the chord associated with the point of evaluation. Alternatively, the streaming operators in Eqs. (4.91), (4.92), (4.94), and (4.96) act on incoming forward source vectors, $\boldsymbol{g}$, or outgoing adjoint source vectors, $\boldsymbol{q}$. These involve only scaling by an attenuation factor. Note that the while the operator $\mathcal{T}_{0+}$ in Eq. (4.90) integrates over a chord from t_- to t_+, the corresponding adjoint-streaming operator $\mathcal{T}^*_{0+}$ in Eq. (4.94) has no such integral. The integral over the chord is subsumed in the inner product in Eq. (4.70).

4.4.1.3 Properties of streaming operators

Streaming operators are defined to help solve the 3D VRTE and its adjoint by transformation to an equivalent system of integral equations. Under the action of the advective derivative, the forward streaming operators behave as follows:

$$(\boldsymbol{v} \cdot \nabla + \sigma)[\, \mathcal{T}_{00}[\, \boldsymbol{f}\,]\,] = \boldsymbol{f}, \tag{4.97}$$

$$(\boldsymbol{v} \cdot \nabla + \sigma)[\, \mathcal{T}_{-0}[\, \boldsymbol{g}\,]\,] = 0. \tag{4.98}$$

Similar properties hold for the adjoint streaming operators:

$$(-\boldsymbol{v} \cdot \nabla + \sigma)[\, \mathcal{T}^*_{00}[\, \boldsymbol{p}\,]\,] = \boldsymbol{p}, \tag{4.99}$$

$$(-\boldsymbol{v} \cdot \nabla + \sigma)\big[\, \mathcal{T}^*_{0+}[\, \boldsymbol{q}\,]\,\big] = 0. \tag{4.100}$$

These are shown in B.1 as Theorem B.1, and they provide the connection between integral and integro-differential forms of the 3D VRTE.

4.4.2 Integral equations for 3D VRTE

The integral operators for scattering and reflection, $\mathcal{Z}$ and $\mathcal{R}$, act on Stokes vectors and return source vectors. The integral operators for streaming, $\mathcal{T}_{00}$, $\mathcal{T}_{0+}$, $\mathcal{T}_{-0}$, and $\mathcal{T}_{-+}$, act on source vectors and return Stokes vectors. In an approximate-numerical setting the Stokes vectors and source vectors will be represented by a finite-dimensional vector

of basis function coefficients. Furthermore, the integral operators will be approximated by linear-matrix transformations acting on these coefficient vectors. With the discrete analogue of matrix algebra in mind, we use a matrix operator notation to keep track of integral operations. As with the solution operators, $\mathcal{U}_a$ and $\mathcal{U}_a^*$, curly brackets are used, $\{::\}$ and $\{:\}$. The objective is to organize the linear integral operations according to the familiar notation of matrix-vector products from linear algebra:

$$\left\{ \begin{array}{cc} \mathcal{Z}\mathcal{T}_{00} & \mathcal{Z}\mathcal{T}_{-0} \\ \mathcal{R}\mathcal{T}_{0+} & \mathcal{R}\mathcal{T}_{-+} \end{array} \right\} \left\{ \begin{array}{c} \boldsymbol{f} \\ \boldsymbol{g} \end{array} \right\} = \left\{ \begin{array}{c} \mathcal{Z}\mathcal{T}_{00}[\,\boldsymbol{f}\,] + \mathcal{Z}\mathcal{T}_{-0}[\,\boldsymbol{g}\,] \\ \mathcal{R}\mathcal{T}_{0+}[\,\boldsymbol{f}\,] + \mathcal{R}\mathcal{T}_{-+}[\,\boldsymbol{g}\,] \end{array} \right\}. \tag{4.101}$$

Normal array operations (such as associativity) behave as expected. For instance, the combined operations of streaming and then scattering can be written in either of the following two ways:

$$\left\{ \begin{array}{cc} \mathcal{Z}\mathcal{T}_{00} & \mathcal{Z}\mathcal{T}_{-0} \\ \mathcal{R}\mathcal{T}_{0+} & \mathcal{R}\mathcal{T}_{-+} \end{array} \right\} = \left\{ \begin{array}{cc} \mathcal{Z} & \\ & \mathcal{R} \end{array} \right\} \left\{ \begin{array}{cc} \mathcal{T}_{00} & \mathcal{T}_{-0} \\ \mathcal{T}_{0+} & \mathcal{T}_{-+} \end{array} \right\}. \tag{4.102}$$

Empty spaces are assumed to represent a null operator. The analogy with matrices extends to the calculation of adjoints:

$$\left\{ \begin{array}{cc} \mathcal{T}_{00} & \mathcal{T}_{-0} \\ \mathcal{T}_{0+} & \mathcal{T}_{-+} \end{array} \right\}^* = \left\{ \begin{array}{cc} \mathcal{T}_{00}^* & \mathcal{T}_{0+}^* \\ \mathcal{T}_{-0}^* & \mathcal{T}_{-+}^* \end{array} \right\}, \tag{4.103}$$

where the adjoint of the 2×2 matrix-operator is defined using the joint inner products from Definition 4.1. This matrix-operator presentation is preferred over the use of indices

which are less easily readable.

4.4.2.1 Forward integral equations

We now present the integral formulation of the 3D VRTE and the so-called successive order of scattering series expansion for its solution. As described in the context of scalar radiative transfer by [76], the Stokes vector, $\boldsymbol{u}$, can be written in terms of the solution vectors, $\boldsymbol{f}$ and $\boldsymbol{g}$, of the forward integral equations:

$$\boldsymbol{u}|_{D\times\mathbb{S}^2} = \mathcal{T}_{00}[\,\boldsymbol{f}\,] + \mathcal{T}_{-0}[\,\boldsymbol{g}\,], \tag{4.104}$$

$$\boldsymbol{u}|_{\Gamma_+} = \mathcal{T}_{0+}[\,\boldsymbol{f}\,] + \mathcal{T}_{-+}[\,\boldsymbol{g}\,], \tag{4.105}$$

$$\boldsymbol{u}|_{\Gamma_-} = \boldsymbol{g}. \tag{4.106}$$

The vectors, $\boldsymbol{f}$ and $\boldsymbol{g}$, are called solutions to the forward integral equations because they solve the integral formulation of the forward 3D VRTE:

$$\begin{Bmatrix} \boldsymbol{f} \\ \boldsymbol{g} \end{Bmatrix} - \begin{Bmatrix} \mathcal{Z}\mathcal{T}_{00} & \mathcal{Z}\mathcal{T}_{-0} \\ \mathcal{R}\mathcal{T}_{0+} & \mathcal{R}\mathcal{T}_{-+} \end{Bmatrix} \begin{Bmatrix} \boldsymbol{f} \\ \boldsymbol{g} \end{Bmatrix} = \begin{Bmatrix} \boldsymbol{f}_\odot \\ \boldsymbol{g}_\odot \end{Bmatrix}. \tag{4.107}$$

This differs from the ancillary integral equations (for diffuse radiation) as they are written in Chapter 3 of [62], in that Eq. (4.107) treats the internal source vector, $\boldsymbol{f}_\odot$, and incoming source vector, $\boldsymbol{g}_\odot$, as separate entities. This allows us to include direct radiation in the solution, causing the source vectors, $\boldsymbol{f}_\odot$ and $\boldsymbol{g}_\odot$, to be identical to those of Definition 4.2.

In B.1, Theorem B.2 we show that the set of Eqs. (4.104) - (4.107) provide a solution to the 3D VRTE that satisfies the integro-differential formulation in Definition 4.2.

Eq. (4.107) is in standard form for a Fredholm integral equations of the second kind. To derive the series expansion for the solution operator, we use a fixed point iteration to obtain the following expression:

$$\begin{Bmatrix} \boldsymbol{f} \\ \boldsymbol{g} \end{Bmatrix} = \begin{Bmatrix} \mathcal{ZT}_{00} & \mathcal{ZT}_{-0} \\ \mathcal{RT}_{0+} & \mathcal{RT}_{-+} \end{Bmatrix}^{K+1} \begin{Bmatrix} \boldsymbol{f} \\ \boldsymbol{g} \end{Bmatrix} + \sum_{k=0}^{K} \begin{Bmatrix} \mathcal{ZT}_{00} & \mathcal{ZT}_{-0} \\ \mathcal{RT}_{0+} & \mathcal{RT}_{-+} \end{Bmatrix}^{k} \begin{Bmatrix} \boldsymbol{f}_{\odot} \\ \boldsymbol{g}_{\odot} \end{Bmatrix}, \tag{4.108}$$

noting that powers, $\{::\}^k$, indicate repeated application of the integral operator. The solve-ability condition on the 3D VRTE must provide that the first term on the right-hand side of Eq. (4.108) will decay to zero. This occurs when σ, $\boldsymbol{Z}$, and $\boldsymbol{R}$ are such that the combined operations of streaming and scattering/reflection give an operator with norm less than unity:

$$\left\| \begin{Bmatrix} \mathcal{ZT}_{00} & \mathcal{ZT}_{-0} \\ \mathcal{RT}_{0+} & \mathcal{RT}_{-+} \end{Bmatrix} \right\|_{\text{op}} < 1. \tag{4.109}$$

If this condition is satisfied, we let $K \to \infty$ in Eq. (4.108) to obtain the successive order of scattering series solution:

$$\begin{Bmatrix} \boldsymbol{f} \\ \boldsymbol{g} \end{Bmatrix} = \sum_{k=0}^{\infty} \begin{Bmatrix} \mathcal{Z}\mathcal{T}_{00} & \mathcal{Z}\mathcal{T}_{-0} \\ \mathcal{R}\mathcal{T}_{0+} & \mathcal{R}\mathcal{T}_{-+} \end{Bmatrix}^k \begin{Bmatrix} \boldsymbol{f}_\odot \\ \boldsymbol{g}_\odot \end{Bmatrix}. \tag{4.110}$$

One may provide a more formal justification, as in [85], using the completeness of the space of square-integrable functions, as defined in Section 4.2.

The series in Eq. (4.110) converges as a square-integrable function and provides the solution vectors, $\boldsymbol{f}$ and $\boldsymbol{g}$, of the forward integral equations and by streaming them according to Eqs. (4.104) and (4.105), they provide the Stokes vector solution to the integro-differential form of 3D VRTE:

$$\begin{Bmatrix} \boldsymbol{u}|_{D\times\mathbb{S}^2} \\ \boldsymbol{u}|_{\Gamma_+} \end{Bmatrix} = \begin{Bmatrix} \mathcal{T}_{00} & \mathcal{T}_{-0} \\ \mathcal{T}_{0+} & \mathcal{T}_{-+} \end{Bmatrix} \begin{Bmatrix} \boldsymbol{f} \\ \boldsymbol{g} \end{Bmatrix}. \tag{4.111}$$

We can thus define the solution operator for the forward 3D VRTE, introduced in Definition 4.2:

$$\mathcal{U}_{\boldsymbol{a}} \begin{Bmatrix} \boldsymbol{f}_\odot \\ \boldsymbol{g}_\odot \end{Bmatrix} = \begin{Bmatrix} \mathcal{T}_{00} & \mathcal{T}_{-0} \\ \mathcal{T}_{0+} & \mathcal{T}_{-+} \end{Bmatrix} \sum_{k=0}^{\infty} \begin{Bmatrix} \mathcal{Z}\mathcal{T}_{00} & \mathcal{Z}\mathcal{T}_{-0} \\ \mathcal{R}\mathcal{T}_{0+} & \mathcal{R}\mathcal{T}_{-+} \end{Bmatrix}^k \begin{Bmatrix} \boldsymbol{f}_\odot \\ \boldsymbol{g}_\odot \end{Bmatrix}. \tag{4.112}$$

4.4.2.2 Adjoint integral equations

The adjoint 3D VRTE has a completely analogous integral formulation to that of the forward model. Using adjoint streaming operations, we write the adjoint Stokes vector, $\boldsymbol{w}$, in terms of the solution vectors, $\boldsymbol{p}$ and $\boldsymbol{q}$, of the adjoint integral equations:

$$\boldsymbol{w}|_{D\times\mathbb{S}^2} = \mathcal{T}^*_{00}[\,\boldsymbol{p}\,] + \mathcal{T}^*_{0+}[\,\boldsymbol{q}\,], \tag{4.113}$$

$$\boldsymbol{w}|_{\Gamma_-} = \mathcal{T}^*_{-0}[\,\boldsymbol{p}\,] + \mathcal{T}^*_{-+}[\,\boldsymbol{q}\,], \tag{4.114}$$

$$\boldsymbol{w}|_{\Gamma_+} = \boldsymbol{q}. \tag{4.115}$$

The vectors, $\boldsymbol{p}$ and $\boldsymbol{q}$, are called solutions to the adjoint integral equations because they solve the integral formulation of the adjoint 3D VRTE:

$$\begin{Bmatrix} \boldsymbol{p} \\ \boldsymbol{q} \end{Bmatrix} - \begin{Bmatrix} \mathcal{Z}^*\mathcal{T}^*_{00} & \mathcal{Z}^*\mathcal{T}^*_{0+} \\ \mathcal{R}^*\mathcal{T}^*_{-0} & \mathcal{R}^*\mathcal{T}^*_{-+} \end{Bmatrix} \begin{Bmatrix} \boldsymbol{p} \\ \boldsymbol{q} \end{Bmatrix} = \begin{Bmatrix} \boldsymbol{p}_\odot \\ \boldsymbol{q}_\odot \end{Bmatrix}. \tag{4.116}$$

The proof that the adjoint Stokes vector, $\boldsymbol{w}$, given by these equations satisfies the adjoint 3D VRTE is given in B.1 as Theorem B.3 .

The vectors, $\boldsymbol{p}$ and $\boldsymbol{q}$, can be expressed as the infinite successive-order of scattering series:

$$\begin{Bmatrix} \boldsymbol{p} \\ \boldsymbol{q} \end{Bmatrix} = \sum_{k=0}^{\infty} \begin{Bmatrix} \mathcal{Z}^*\mathcal{T}^*_{00} & \mathcal{Z}^*\mathcal{T}^*_{0+} \\ \mathcal{R}^*\mathcal{T}^*_{-0} & \mathcal{R}^*\mathcal{T}^*_{-+} \end{Bmatrix}^k \begin{Bmatrix} \boldsymbol{p}_\odot \\ \boldsymbol{q}_\odot \end{Bmatrix}. \tag{4.117}$$

This expression provides the solution vectors, $\boldsymbol{p}$ and $\boldsymbol{q}$, of the adjoint integral equations

and by streaming them according to Eqs. (4.113) and (4.114), they provide the Stokes vector solution to the integro-differential form of the adjoint 3D VRTE:

$$\left\{ \begin{array}{c} \boldsymbol{w}|_{D\times\mathbb{S}^2} \\ \boldsymbol{w}|_{\Gamma_-} \end{array} \right\} = \left\{ \begin{array}{cc} \mathcal{T}^*_{00} & \mathcal{T}^*_{0+} \\ \mathcal{T}^*_{-0} & \mathcal{T}^*_{-+} \end{array} \right\} \left\{ \begin{array}{c} \boldsymbol{p} \\ \boldsymbol{q} \end{array} \right\}. \tag{4.118}$$

The solution operator for the adjoint 3D VRTE, introduced in Definition 4.3, can therefore be written as follows:

$$\mathcal{U}^*_{\boldsymbol{a}} \left\{ \begin{array}{c} \boldsymbol{p}_\odot \\ \boldsymbol{q}_\odot \end{array} \right\} = \left\{ \begin{array}{cc} \mathcal{T}^*_{00} & \mathcal{T}^*_{0+} \\ \mathcal{T}^*_{-0} & \mathcal{T}^*_{-+} \end{array} \right\} \sum_{k=0}^{\infty} \left\{ \begin{array}{cc} \mathcal{Z}^*\mathcal{T}^*_{00} & \mathcal{Z}^*\mathcal{T}^*_{0+} \\ \mathcal{R}^*\mathcal{T}^*_{-0} & \mathcal{R}^*\mathcal{T}^*_{-+} \end{array} \right\}^k \left\{ \begin{array}{c} \boldsymbol{p}_\odot \\ \boldsymbol{q}_\odot \end{array} \right\}. \tag{4.119}$$

4.4.3 Fundamental adjoint property for the 3D VRTE

For the solution operator of the adjoint problem in Definition 4.3, we wrote, "$\mathcal{U}^*_{\boldsymbol{a}}$," anticipating that it would be the adjoint of the solution operator for the forward VRTE, which we denoted by "$(\mathcal{U}_{\boldsymbol{a}})^*$". The notation hints that the equation, $(\mathcal{U}_{\boldsymbol{a}})^* = \mathcal{U}^*_{\boldsymbol{a}}$, holds; that the adjoint of the solution operator for the forward 3D VRTE is the solution operator for the adjoint 3D VRTE. In fact, this relation justifies the name *adjoint* 3D VRTE, and must be proven through verification of the fundamental adjoint property:

$$\left\langle \left\{ \begin{array}{c} \boldsymbol{p}_\odot \\ \boldsymbol{q}_\odot \end{array} \right\}, \mathcal{U}_{\boldsymbol{a}} \left\{ \begin{array}{c} \boldsymbol{f}_\odot \\ \boldsymbol{g}_\odot \end{array} \right\} \right\rangle_{D\times\mathbb{S}^2\oplus\Gamma_+} = \left\langle \mathcal{U}^*_{\boldsymbol{a}} \left\{ \begin{array}{c} \boldsymbol{p}_\odot \\ \boldsymbol{q}_\odot \end{array} \right\}, \left\{ \begin{array}{c} \boldsymbol{f}_\odot \\ \boldsymbol{g}_\odot \end{array} \right\} \right\rangle_{D\times\mathbb{S}^2\oplus\Gamma_-}. \tag{4.120}$$

An equivalent form of this equation is written in terms of the solutions to the integral equations of 3D VRT, and it is this statement that we prove.

Theorem 4.4 (Fundamental adjoint property)**.** *For any feasible parameter, $\boldsymbol{a}$, and the corresponding single-scattering properties, σ, $\boldsymbol{Z}$, and $\boldsymbol{R}$, satisfying the solve-ability constraint in Eq. (4.109); the following fundamental adjoint property holds:*

$$\begin{aligned}\left\langle \begin{Bmatrix} \boldsymbol{p}_\odot \\ \boldsymbol{q}_\odot \end{Bmatrix}, \begin{Bmatrix} \mathcal{T}_{00} & \mathcal{T}_{-0} \\ \mathcal{T}_{0+} & \mathcal{T}_{-+} \end{Bmatrix} \begin{Bmatrix} \boldsymbol{f} \\ \boldsymbol{g} \end{Bmatrix} \right\rangle_{D\times\mathbb{S}^2\oplus\Gamma_+} \\ = \left\langle \begin{Bmatrix} \mathcal{T}^*_{00} & \mathcal{T}^*_{0+} \\ \mathcal{T}^*_{-0} & \mathcal{T}^*_{-+} \end{Bmatrix} \begin{Bmatrix} \boldsymbol{p} \\ \boldsymbol{q} \end{Bmatrix}, \begin{Bmatrix} \boldsymbol{f}_\odot \\ \boldsymbol{g}_\odot \end{Bmatrix} \right\rangle_{D\times\mathbb{S}^2\oplus\Gamma_-},\end{aligned} \tag{4.121}$$

where the vectors, $\boldsymbol{f}$ and $\boldsymbol{g}$, solve the forward integral equations with square-integrable source vector, $\boldsymbol{f}_\odot$ and $\boldsymbol{g}_\odot$; and the vectors, $\boldsymbol{p}$ and $\boldsymbol{q}$, solve the adjoint integral equations with square-integrable adjoint source vectors, $\boldsymbol{p}_\odot$ and $\boldsymbol{q}_\odot$.

Proof. We begin by substituting the adjoint integral equation for $\boldsymbol{p}_\odot$ and $\boldsymbol{q}_\odot$, given by Eq. (4.116), into the left hand side of Eq. (4.121) and proceed through the following

steps:

$$\left\langle \begin{Bmatrix} \boldsymbol{p}_{\odot} \\ \boldsymbol{q}_{\odot} \end{Bmatrix}, \begin{Bmatrix} \mathcal{T}_{00} & \mathcal{T}_{-0} \\ \mathcal{T}_{0+} & \mathcal{T}_{-+} \end{Bmatrix} \begin{Bmatrix} \boldsymbol{f} \\ \boldsymbol{g} \end{Bmatrix} \right\rangle_{D\times\mathbb{S}^2\oplus\Gamma_+} =$$

$$= \left\langle \begin{Bmatrix} \boldsymbol{p} \\ \boldsymbol{q} \end{Bmatrix}, \begin{Bmatrix} \mathcal{T}_{00} & \mathcal{T}_{-0} \\ \mathcal{T}_{0+} & \mathcal{T}_{-+} \end{Bmatrix} \begin{Bmatrix} \boldsymbol{f} \\ \boldsymbol{g} \end{Bmatrix} \right\rangle_{D\times\mathbb{S}^2\oplus\Gamma_+}$$

$$- \left\langle \begin{Bmatrix} \mathcal{Z}^*\mathcal{T}_{00}^* & \mathcal{Z}^*\mathcal{T}_{0+}^* \\ \mathcal{R}^*\mathcal{T}_{-0}^* & \mathcal{R}^*\mathcal{T}_{-+}^* \end{Bmatrix} \begin{Bmatrix} \boldsymbol{p} \\ \boldsymbol{q} \end{Bmatrix}, \right.$$

$$\left. \begin{Bmatrix} \mathcal{T}_{00} & \mathcal{T}_{-0} \\ \mathcal{T}_{0+} & \mathcal{T}_{-+} \end{Bmatrix} \begin{Bmatrix} \boldsymbol{f} \\ \boldsymbol{g} \end{Bmatrix} \right\rangle_{D\times\mathbb{S}^2\oplus\Gamma_+} ; \tag{4.122}$$

$$= \left\langle \begin{Bmatrix} \mathcal{T}_{00}^* & \mathcal{T}_{0+}^* \\ \mathcal{T}_{-0}^* & \mathcal{T}_{-+}^* \end{Bmatrix} \begin{Bmatrix} \boldsymbol{p} \\ \boldsymbol{q} \end{Bmatrix}, \begin{Bmatrix} \boldsymbol{f} \\ \boldsymbol{g} \end{Bmatrix} \right\rangle_{D\times\mathbb{S}^2\oplus\Gamma_-}$$

$$- \left\langle \begin{Bmatrix} \mathcal{T}_{00}^* & \mathcal{T}_{0+}^* \\ \mathcal{T}_{-0}^* & \mathcal{T}_{-+}^* \end{Bmatrix} \begin{Bmatrix} \boldsymbol{p} \\ \boldsymbol{q} \end{Bmatrix}, \right.$$

$$\left. \begin{Bmatrix} \mathcal{Z}\mathcal{T}_{00} & \mathcal{Z}\mathcal{T}_{-0} \\ \mathcal{R}\mathcal{T}_{0+} & \mathcal{R}\mathcal{T}_{-+} \end{Bmatrix} \begin{Bmatrix} \boldsymbol{f} \\ \boldsymbol{g} \end{Bmatrix} \right\rangle_{D\times\mathbb{S}^2\oplus\Gamma_-} ; \tag{4.123}$$

$$= \left\langle \begin{Bmatrix} \mathcal{T}_{00}^* & \mathcal{T}_{0+}^* \\ \mathcal{T}_{-0}^* & \mathcal{T}_{-+}^* \end{Bmatrix} \begin{Bmatrix} \boldsymbol{p} \\ \boldsymbol{q} \end{Bmatrix}, \begin{Bmatrix} \boldsymbol{f}_{\odot} \\ \boldsymbol{g}_{\odot} \end{Bmatrix} \right\rangle_{D\times\mathbb{S}^2\oplus\Gamma_-} . \tag{4.124}$$

These three steps are justified as follows: Eq. (4.122) is obtained by substitution of the integral equations of adjoint 3D VRT; Eq. (4.123) is obtained by using elementary adjoint properties of streaming, scattering and reflection operators; and Eq. (4.124) is obtained

by substitution of the integral equations of forward 3D VRT. The second step can be verified by expanding to a sum of elementary inner products (that is $\langle \cdot, \cdot \rangle_{D \times \mathbb{S}^2}$, $\langle \cdot, \cdot \rangle_{\Gamma_+}$, and $\langle \cdot, \cdot \rangle_{\Gamma_-}$), applying elementary adjoint properties, and collapsing back into the matrix notation. □

4.5 Concluding remarks

Adjoint methods can enable the use of 3D VRTE simulations for adjusting 3D atmospheric properties to fit multi-angle, multi-pixel polarimetric measurements of the Earth's atmosphere. This is shown by focusing on computing the misfit function and its gradient, and doing so with only two calls to a 3D VRTE solver for each wavelength. Scalable methods such as the adjoint method presented here will allow the role of the 3D VRTE to transition from a test bed for verifying plane-parallel retrievals to the core engine for performing large-scale retrievals of atmospheric properties for scenes with strongly heterogeneous cloud cover. The primary benefit is that the 3D spatial dependencies of the sampling volume for remote sensing measurements will be explicitly modeled. The lack of default assumptions on cloud horizontal variability will allow for a more flexible parameterization of cloud structure and a more realistic model for measurements of broken cloud fields and the regions near cloud edges. As a near-term application of the adjoint method, Section 4.3 discussed the use of a multi-pixel measurement operator to correct plane-parallel retrievals that have errors caused by 3D effects, including adjacency effects. Other applications are more ambitious and will require future research into

how to parameterize cloud and aerosol properties in 3D. The adjoint method provides a way to adjust atmosphere and surface parameters that will scale to large problems — a foundation for a new class of retrieval algorithm, which uses a three-dimensional parametrization of atmosphere and surface properties to simultaneously reconstruct both spatial and microphysical variability.

Chapter 5

Summary and outlook

With the underlying goal of using 3D computations to extend cloud and aerosol retrieval capabilities, we identified two projects which would further that goal and also make independent contributions. Our work on the parametrization of single-scattering properties in terms of cloud and aerosol particles is a necessary component of the 3D problem, and it is a valuable tool for fitting the measurements of laboratory and airborne nephelometers. After developing codes for this forward model, we analyzed the stability of the corresponding inverse problem to determine which particle properties can be retrieved, and which measurements provide the required constraints. Then, we considered the large-scale problem of 3D remote sensing. Focusing on the question of how to use existing solvers in the retrieval of clouds and aerosols, we identified the importance of scalability, and derived an adjoint method that can adjust all unknown parameters with only two calls to the 3D VRTE solver for each spectral channel, regardless of the number of retrieval

parameters, measurement view angles or pixels. The scalability of this adjoint method encourages its use in developing a new class of 3D retrieval algorithms with more flexible parameterizations of spatial heterogeneity and better retrievals of cloud and aerosol properties in broken cloud fields. It is also worth noting that retrievals based on single-scattering properties are applicable to the validation of future 3D retrievals, since they will enable us to compare the 3D retrievals with independent retrievals derived from the *in situ* measurements of an airborne nephelometer.

In summary, this thesis contributes a detailed analysis of the sensitivity of single-scattering measurements to the properties of airborne particles, and it describes a solution to the problem of scale that is inherent to doing 3D retrievals of clouds and aerosols in the atmosphere. While these contributions make significant advances toward the long-term goal of retrieving clouds and aerosols in broken cloud fields, there are a number of open issues. The description of these issues provides useful insight into the highly challenging nature of this topic of research and also into the value of the work which we have done. The following two sections summarize the contributions included in this thesis as well as present our general outlook toward future work: single scattering is discussed in Section 5.1, and multiple scattering is discussed in Section 5.2. In each case the results are connected with the long-term goal of retrieving cloud and aerosol properties in broken cloud fields — retrievals which would greatly improve the modeling of cloud-aerosol interactions and the prediction of how these interactions impact weather and climate.

5.1 Outlook for single-scattering

As mentioned in Chapter 3, the work of several groups has demonstrated the ability to obtain laboratory measurements of nearly all single-scattering properties of airborne particles, and at wavelengths corresponding to the full spectrum of visible electro-magnetic radiation. Efforts to extend these laboratory technologies to instruments capable of *in situ* measurements of atmospheric aerosols are in progress [31], but face additional challenges that make the determination of all single-scattering properties impractical or prohibitively expensive. Chapter 3 focused on determining which single-scattering measurements are most useful for resolving the aerosol properties that are of interest to atmospheric modelers. The analysis reveals that a substantial amount of information, for the retrieval of particle properties, is present in the angular profiles of scattering matrix elements, provided that particles are large enough to resonate with the observed wavelengths of visible light. Additional constraints on the volume-scattering and volume-absorption coefficients resolve the concentration of particle volume, mass, and surface area, but fail to resolve the number concentration of particles due to the relatively low scattering efficiency of very-small particles. Consistent with intuition from the Lorenz-Mie calculations in Chapter 2, the scattering matrix elements provide less information on fine-mode particles as profiles of the scattering matrix elements transition toward the Rayleigh regime. One observed consequence is that information on the volume-absorption coefficient is required to constrain estimates of the spectrally dependent imaginary refractive index for fine-mode absorbing particles. By attributing information for specific airborne-particle

properties to the required single-scattering measurements, these results provide a useful guide for determining which types of single-scattering measurements will be most useful for retrieving aerosol properties.

The calculations of Chapter 2 show the well-known results that absorption is proportional to the volume and mass concentrations for particles of all sizes, and that scattering is negligible for particles which are too small to resonate with the observed wavelength of light. This resonance interval aligned with the stability analysis which was presented in Chapter 3, where the size distribution of small particles was unresolved, even by full measurements of all single-scattering properties. Unfortunately, the uncertainty in the size distribution of small particles resulted in poor constraints on the concentration of CCN, even when the minimum radius required for CCN activity is assumed to be an overestimation relative to observations of aerosols in the atmosphere [22]. This leads to the open question of how the concentration of CCN can be resolved, since accurate estimates would be very useful in the study of cloud-aerosol interactions. One idea for future work is to analyze the information content in single-scattering measurements at shorter ultra-violet wavelengths. This study would determine if the extra information from shorter wavelengths is sufficient to resolve the size distribution down to the smallest active CCN.

Another open issue is related to our choice to consider only spherical aerosols in this first study. Eventually, the development of atmospheric retrievals will require a few additional types of aerosols which are non-spherical. These will include ice crystals, desert dust, and soot; and each type of non-spherical aerosol will have parameters which describe their

shape, or distribution of shapes. While there is evidence that it is not possible to constrain shape, size and complex refractive index together [57], this conclusion was drawn based on an incomplete set of scattering measurements. Therefore a stability analysis similar to that of Chapter 3 would provide a more conclusive assessment of the parameters which can be resolved by single-scattering measurements and the specific measurements needed to do so. Such a study would also provide an opportunity to identify, in a more general way, the particle-size-related limitations that are associated with visible light-scattering measurements.

5.2 Outlook for 3D retrievals

As we mentioned in Chapter 1, the development of new retrieval algorithms goes beyond the scope of this dissertation. In Chapter 4, the presentation of the adjoint method was restricted to a discussion of the scale the atmospheric retrieval problem and to a precise mathematical formulation for adjusting unknown parameters as efficiently as possible. The benefits may be summarized by considering that at each iteration the 3D retrieval algorithm must adjust thousands of unknown parameters to improve their fit with millions of polarimetric measurements. Conventional approaches used in remote sensing of the atmosphere are ill-suited to such large-scale problems: The finite-difference methods used to compute the required derivatives would need ten-thousand calls to a solver, and the most commonly used derivative would have ten-billion elements and require eighty-billion

bytes of memory. In contrast, the adjoint method requires only two calls to a solver and computes a derivative with only ten-thousand elements.

There are few recent studies which use 3D radiative transfer to prototype methods for retrieving cloud properties [15, 16, 84], but our paper was the first to discuss adjoint methods as a means of reducing the computational cost of adjusting unknowns with the full 3D VRTE [21]. This is not too surprising given that a suitable computational solver was developed only very recently by Evans [81]. The primary open issue regarding the use of adjoint methods in 3D retrievals is that the computational tools are less well developed than those for retrieving clouds and aerosols with plane-parallel or spherical symmetry. Recognizing this, we have contacted Frank Evans, Adrian Doicu and other colleagues who are actively developing tools for solving the 3D VRTE [80], and have begun making plans to collaborate on the required extensions to their codes. Also, we are scheduled to give a short talk on the adjoint method at the American Meteorological Society meeting on atmospheric radiation, and hope to stimulate some additional interest in this line of research.

Through the research presented in Chapter 4 and these collaborative efforts, we hope to develop new tools that will take full advantage of the next generation of remote sensing technology. In our view, the instrument platforms with the greatest potential will combine passive and active techniques to constrain both the spatial and microphysical variability of clouds and aerosols. For instance, NASA's Aerosol and Cloud Ecosystem mission (ACE) will combine passive polarimetric measurements with cloud RADAR and high spectral resolution LIDAR (HSRL). The cloud RADAR penetrates clouds and will provide a

structural outline of deep convection and precipitation, and a multi-beam cross-track HSRL will provide a structural outline of smaller aerosol particles. The passive multi-pixel polarimetric measurements considered in Chapter 4 add many more independent constraints on the angular dependence of scattering and may permit the retrieval of particle size and refractive index. With a rough outline of clouds and aerosols provided by the active-sounding instruments, the passive-imaging instrument will fill in microphysical details one iterative adjustment at a time to retrieve the full 3D distribution.

Following the development numerical tools for solving the 3D VRTE and computing derivatives with the adjoint method, we will test the retrieval capabilities of various sensors. Synthetic test cases of aerosol laden cloud fields will be created using large eddy simulations as in [15]. Using an ideal set of simulated full measurements, we will retrieve the profiles of cloud and aerosol properties as required by the ACE mission. These include aerosol loading, size, shape, and complex refractive index; and cloud loading, size, and phase. In addition to ideal measurements, we plan to investigate how the results of retrievals degrade when only incomplete information is available. As in Chapter 3, our strategy will be to analyze the information content in various subsets of complete data and then to compare the performance of each design option for the purpose of retrieving cloud and aerosol properties. The results may help guide the development of new sensors and determine which combination of active and passive instruments will give the best retrievals in broken cloud fields.

Bibliography

[1] Susan Solomon, Intergovernmental Panel on Climate Change, and Intergovernmental Panel on Climate Change. *Climate Change 2007: The Physical Science Basis: Contribution of Working Group I to the Fourth Assessment Report of the Intergovernmental Panel on Climate Change*. Cambridge University Press, Cambridge ; New York, 2007. ISBN 9780521880091.

[2] O. Boucher, D. Randall, P. Artaxo, C. Bretherton, G. Feingold, P. Forster, V.-M. Kerminen, Y. Kondo, H. Liao, U. Lohmann, P. Rasch, S.K. Satheesh, S. Sherwood, B. Stevens, and X.Y. Zhang. Clouds and aerosols. In *Climate Change 2013: The Physical Science Basis. Contribution of Working Group I to the Fifth Assessment Report of the Intergovernmental Panel on Climate Change*. Cambridge University Press, Cambridge, United Kingdom and New York, NY, USA, 2013.

[3] U. Lohmann and J. Feichter. Global indirect aerosol effects: a review. *Atmospheric Chemistry and Physics*, 5:715–737, March 2005. ISSN 1680-7324.

[4] Mark Z. Jacobson. Analysis of aerosol interactions with numerical techniques for solving coagulation, nucleation, condensation, dissolution, and reversible chemistry among multiple size distributions. *Journal of Geophysical Research*, 107:23 PP., October 2002. doi: 200210.1029/2001JD002044. URL http://www.agu.org.ezproxy.cul.columbia.edu/pubs/crossref/2002/2001JD002044.shtml.

[5] Steven J. Ghan and Stephen E. Schwartz. Aerosol properties and processes - a path from field and laboratory measurements to global climate models RID c-2729-2008. *Bulletin of the American Meteorological Society*, 88(7):1059–+, July 2007. ISSN 0003-0007. doi: 10.1175/BAMS-88-7-1059. WOS:000248565600019.

[6] M. I. Mishchenko, B. Cairns, J. E. Hansen, L. D. Travis, R. Burg, Y. J. Kaufman, J. V. Martins, and E. P. Shettle. Monitoring of aerosol forcing of climate from space: analysis of measurement requirements. *Journal of Quantitative Spectroscopy & Radiative Transfer*, 88(1-3):149–161, 2004. ISSN 0022-4073.

[7] Committee on Earth Science NRC, Applications from Space: A Community Assessment, and National Research Council Strategy for the Future. *Earth Science and Applications from Space: National Imperatives for the Next Decade and Beyond*. The National Academies Press, 2007.

[8] Kirk Knobelspiesse, Brian Cairns, Michael Mishchenko, Jacek Chowdhary, Kostas Tsigaridis, Bastiaan van Diedenhoven, William Martin, Matteo Ottaviani, and Mikhail Alexandrov. Analysis of fine-mode aerosol retrieval capabilities by different passive remote sensing instrument designs. *Optics Express*, 20(19):21457–21484, 2012. ISSN 1094-4087.

[9] F. Waquet, J. Riedi, L. C. Labonnote, P. Goloub, B. Cairns, J-L. Deuzé, and D. Tanré. Aerosol remote sensing over clouds using A-train observations. *Journal of the Atmospheric Sciences*, pages 2468–2480, 2009.

[10] WilliamB. Rossow and Brian Cairns. Monitoring changes of clouds. *Climatic Change*, 31(2-4):305–347, 1995. ISSN 0165-0009. doi: 10.1007/BF01095151. URL http://dx.doi.org/10.1007/BF01095151.

[11] Zhibo Zhang, Andrew S. Ackerman, Graham Feingold, Steven Platnick, Robert Pincus, and Huiwen Xue. Effects of cloud horizontal inhomogeneity and drizzle on remote sensing of cloud droplet effective radius: Case studies based on large-eddy simulations. *Journal of Geophysical Research-Atmospheres*, 117:D19208, 2012. ISSN 2169-897X.

[12] Tamas Varnai and Alexander Marshak. Global CALIPSO observations of aerosol changes near clouds. *IEEE Geoscience and Remote Sensing Letters*, 8(1):19–23, 2011. ISSN 1545-598X.

[13] Á. Horváth and R. Davies. Anisotropy of water cloud reflectance: A comparison of measurements and. *Geophysical Research Letters*, 31(1):L01102, 2004. ISSN 0094-8276.

[14] L. A. Remer, Y. J. Kaufman, D. Tanre, S. Mattoo, D. A. Chu, J. V. Martins, R. R. Li, C. Ichoku, R. C. Levy, R. G. Kleidman, T. F. Eck, E. Vermote, and B. N. Holben. The MODIS aerosol algorithm, products, and validation. *Journal of the Atmospheric Sciences*, 62(4):947–973, 2005. ISSN 0022-4928.

[15] K. Franklin Evans, Alexander Marshak, and Tamas Varnai. The potential for improved boundary layer cloud optical depth retrievals from the multiple directions of MISR. *Journal of the Atmospheric Sciences*, 65(10):3179–3196, 2008. ISSN 0022-4928.

[16] David J. Diner, Bobby H. Braswell, Roger Davies, Nadine Gobron, Jiannan Hu, Yufang Jin, Ralph A. Kahn, Yuri Knyazikhin, Norman Loeb, Jan-Peter Muller, Anne W. Nolin, Bernard Pinty, Crystal B. Schaaf, Gabriela Seiz, and Julienne Stroeve. The value of multiangle measurements for retrieving structurally and radiatively consistent properties of clouds, aerosols, and surfaces. *Remote Sensing of Environment*, 97(4):495–518, 2005. ISSN 0034-4257.

[17] Johnathan W. Hair, Chris A. Hostetler, Anthony L. Cook, David B. Harper, Richard A. Ferrare, Terry L. Mack, Wayne Welch, Luis Ramos Izquierdo, and

Floyd E. Hovis. Airborne high spectral resolution lidar for profiling aerosol optical properties. *Applied Optics*, 47(36):6734–6752, 2008. ISSN 1559-128X.

[18] Dong Huang, Yangang Liu, and Warren Wiscombe. Determination of cloud liquid water distribution using 3D cloud tomography. *Journal of Geophysical Research-Atmospheres*, 113(D13):D13201, 2008. ISSN 2169-897X.

[19] Dong Huang, Yangang Liu, and Warren Wiscombe. Cloud tomography: Role of constraints and a new algorithm. *Journal of Geophysical Research-Atmospheres*, 113:D23203, 2008. ISSN 2169-897X.

[20] Kui Ren, Guillaume Bal, and Andreas H. Hielscher. Frequency domain optical tomography based on the equation of radiative transfer. *SIAM Journal on Scientific Computing*, 28(4):1463–1489, 2006. ISSN 1064-8275, 1095-7197.

[21] William Martin, Brian Cairns, and Guillaume Bal. Adjoint methods for adjusting three-dimensional atmosphere and surface properties to fit multi-angle/multi-pixel polarimetric measurements. *Journal of Quantitative Spectroscopy and Radiative Transfer*, 144:68–85, 2014. ISSN 0022-4073. doi: 10.1016/j.jqsrt.2014.03.030. URL http://www.sciencedirect.com/science/article/pii/S002240731400154X.

[22] U. Dusek, G. P. Frank, L. Hildebrandt, J. Curtius, J. Schneider, S. Walter, D. Chand, F. Drewnick, S. Hings, D. Jung, S. Borrmann, and M. O. Andreae. Size matters more than chemistry for cloud-nucleating ability of aerosol particles. *Science*, 312(5778):1375–1378, June 2006. ISSN 0036-8075. doi: 10.1126/science.1125261. WOS:000237961600054.

[23] P. K. Quinn, T. S. Bates, D. J. Coffman, and D. S. Covert. Influence of particle size and chemistry on the cloud nucleating properties of aerosols. *Atmospheric Chemistry and Physics*, 8(4):1029–1042, 2008. ISSN 1680-7316. doi: 10.5194/acp-8-1029-2008.

[24] Drew Shindell, Johan C. I. Kuylenstierna, Elisabetta Vignati, Rita van Dingenen, Markus Amann, Zbigniew Klimont, Susan C. Anenberg, Nicholas Muller, Greet Janssens-Maenhout, Frank Raes, Joel Schwartz, Greg Faluvegi, Luca Pozzoli, Kaarle Kupiainen, Lena Hoeglund-Isaksson, Lisa Emberson, David Streets, V. Ramanathan, Kevin Hicks, N. T. Kim Oanh, George Milly, Martin Williams, Volodymyr Demkine, and David Fowler. Simultaneously mitigating Near-Term climate change and improving human health and food security. *Science*, 335(6065):183–189, January 2012. ISSN 0036-8075. doi: 10.1126/science.1210026. WOS:000299033100044.

[25] William Martin, Brian Cairns, Kirk Knobelspiesse, Michael Mishchenko, Jacek Chowdhary, Bastiaan van Diedenhoven, Matteo Ottaviani, and Mikhail Alexandrov. Aerosol retrievals from single-scattering measurements in the visible spectrum: resolved microphysical properties, fundamental limitations, and the benefits of polarization. *Applied Optics*, 201X. (in preparation for Applied Optics).

[26] Clive D. Rodgers. *Inverse methods for atmospheric sounding*, volume 2 of *Series on Atmospheric, Oceanic and Planetary Physics*. World Scientific Publishing Co. Inc., River Edge, NJ, 2000. ISBN 981-02-2740-X. Theory and practice.

[27] O. Muñoz and J. W. Hovenier. Laboratory measurements of single light scattering by ensembles of randomly oriented small irregular particles in air: A review. *Journal of Quantitative Spectroscopy & Radiative Transfer*, 112(11):1646–1657, July 2011. ISSN 0022-4073. doi: 10.1016/j.jqsrt.2011.02.005. WOS:000292533900003.

[28] H Volten, O Muñoz, E Rol, JF de Haan, W Vassen, JW Hovenier, K Muinonen, and T Nousiainen. Scattering matrices of mineral aerosol particles at 441.6 nm and 632.8 nm RID a-7982-2008. *Journal of Geophysical Research-Atmospheres*, 106 (D15):17375–17401, August 2001. ISSN 0747-7309. doi: 10.1029/2001JD900068. WOS:000170457200022.

[29] G. W. Grams, I. H. Blifford, D. A. Gillette, and P. B. Russell. Complex index of refraction of airborne soil particles. *Journal of Applied Meteorology*, 13(4):459–471, June 1974. ISSN 0021-8952. doi: 10.1175/1520-0450(1974)013⟨0459:CIOROA⟩2.0.CO;2.

[30] Oleg Dubovik, Brent Holben, Thomas F. Eck, Alexander Smirnov, Yoram J. Kaufman, Michael D. King, Didier Tanré, and Ilya Slutsker. Variability of absorption and optical properties of key aerosol types observed in worldwide locations. *Journal of the Atmospheric Sciences*, 59(3):590–608, February 2002. ISSN 0022-4928, 1520-0469. doi: 10.1175/1520-0469(2002)059⟨0590:VOAAOP⟩2.0.CO;2.

[31] Gergely Dolgos, J. Vanderlei Martins, Lorraine A Remer, Alexandre L Correia, Manfredo Tabacniks, and Adriana R Lima. Characterization of aerosol scattering and spectral absorption by unique methods: a polar/imaging nephelometer and spectral reflectance measurements of aerosol samples collected on filters. *Proceedings of SPIE*, 7588(1):75880E–75880E–12, February 2010. ISSN 0277786X. doi: doi:10.1117/12.842069.

[32] S. Chandrasekhar. *Radiative Transfer*. Dover Publications, New York, 1960.

[33] Michael I. Mishchenko, Larry D. Travis, and Andrew A. Lacis. *Multiple scattering of light by particles: radiative transfer and coherent backscattering*. Cambridge University Press, 2006. ISBN 9780521834902.

[34] H. C. van de Hulst. *Light Scattering by Small Particles*. Structure of matter series. Wiley, New York, 1957.

[35] Michael I. Mishchenko and Larry D. Travis. Electromagnetic scattering by particles and surfaces. http://www.giss.nasa.gov/staff/mmishchenko/, 2014. Accessed: May 12th 2014.

[36] O. Dubovik and M. D King. A flexible inversion algorithm for retrieval of aerosol optical properties from sun and sky radiance measurements. *Journal of Geophysical Research*, 105(D16):20676, 2000.

[37] A. Marshak, A. Davis, W. Wiscombe, and R. Cahalan. Radiative smoothing in fractal clouds. *Journal of Geophysical Research-Atmospheres*, 100(D12):26247–26261, December 1995. ISSN 0148-0227. doi: 10.1029/95JD02895.

[38] Guillaume Bal. Inverse transport theory and applications. *Inverse Problems*, 25(5): 053001, May 2009. ISSN 0266-5611. doi: 10.1088/0266-5611/25/5/053001.

[39] H. Moosmüller, R.K. Chakrabarty, and W.P. Arnott. Aerosol light absorption and its measurement: A review. *Journal of Quantitative Spectroscopy and Radiative Transfer*, 110(11):844–878, July 2009. ISSN 0022-4073. doi: 10.1016/j.jqsrt.2009.02.035. URL http://www.sciencedirect.com/science/article/pii/S0022407309000879.

[40] V. V. Veretennikov, V. S. Kozlov, I. E. Naats, and V. Ya. Fadeev. Optical studies of smoke aerosols: an inversion method and its applications. *Optics Letters*, 4(12): 411–413, December 1979. doi: 10.1364/OL.4.000411.

[41] M. Z. Hansen. Atmospheric particulate analysis using angular light scattering. *Applied Optics*, 19(20):3441–3448, October 1980. doi: 10.1364/AO.19.003441.

[42] J. Heintzenberg and R. M. Welch. Retrieval of aerosol size distribution from angular scattering functions: effects of particle composition and shape. *Applied Optics*, 21 (5):822–830, March 1982. doi: 10.1364/AO.21.000822.

[43] Masayuki Tanaka, Teruyuki Nakajima, and Tamio Takamura. Simultaneous determination of complex refractive index and size distribution of airborne and water-suspended particles from light scattering measurements. *Journal of Meteorological Society of Japan. Ser.II*, 60(6):1259–1272, December 1982. ISSN 00261165.

[44] Xiaodong Zhang, Michael Twardowski, and Marlon Lewis. Retrieving composition and sizes of oceanic particle subpopulations from the volume scattering function. *Applied Optics*, 50(9):1240–1259, March 2011. doi: 10.1364/AO.50.001240. URL http://ao.osa.org/abstract.cfm?URI=ao-50-9-1240.

[45] Brian Barkey, Suzanne E. Paulson, and Albert Chung. Genetic algorithm inversion of dual polarization polar nephelometer data to determine aerosol refractive index. *Aerosol Science and Technology*, 41(8):751–760, 2007. ISSN 0278-6826. doi: 10.1080/02786820701432640. WOS:000248575900003.

[46] Kristin Lewis, William P. Arnott, Hans Moosmüller, and Cyle E. Wold. Strong spectral variation of biomass smoke light absorption and single scattering albedo observed with a novel dual-wavelength photoacoustic instrument. *Journal of Geophysical Research*, 113(D16), August 2008. ISSN 0148-0227. doi: 10.1029/2007JD009699.

[47] R. K. Chakrabarty, H. Moosmüller, L. -W. A. Chen, K. Lewis, W. P. Arnott, C. Mazzoleni, M. K. Dubey, C. E. Wold, W. M. Hao, and S. M. Kreidenweis. Brown carbon in tar balls from smoldering biomass combustion. *Atmospheric Chemistry and Physics*, 10(13):6363–6370, 2010. ISSN 1680-7316. doi: 10.5194/acp-10-6363-2010.

[48] O. Muñoz, F. Moreno, D. Guirado, J.L. Ramos, A. López, F. Girela, J.M. Jerónimo, L.P. Costillo, and I. Bustamante. Experimental determination of scattering matrices of dust particles at visible wavelengths: The IAA light scattering apparatus. *Journal of Quantitative Spectroscopy and Radiative Transfer*, 111(1):187–196, January 2010. ISSN 0022-4073. doi: 10.1016/j.jqsrt.2009.06.011.

[49] yvind Svensen, Jakob J. Stamnes, Morten Kildemo, Lars Martin Sandvik Aas, Svein Rune Erga, and yvind Frette. Mueller matrix measurements of algae with different shape and size distributions. *Applied Optics*, 50(26):5149–5157, 2011. doi: 10.1364/AO.50.005149.

[50] O. P. Hasekamp. Capability of multi-viewing-angle photo-polarimetric measurements for the simultaneous retrieval of aerosol and cloud properties. *Atmospheric Measurement Techniques*, 3(4):839–851, 2010. ISSN 1867-1381. doi: 10.5194/amt-3-839-2010. WOS:000281432100003.

[51] O. Dubovik, M. Herman, A. Holdak, T. Lapyonok, D. Tanré, J. L. Deuzé, F. Ducos, A. Sinyuk, and A. Lopatin. Statistically optimized inversion algorithm for enhanced retrieval of aerosol properties from spectral multi-angle polarimetric satellite observations. *Atmospheric Measurement Techniques*, 4(5):975–1018, May 2011. ISSN 1867-8548. doi: 10.5194/amt-4-975-2011.

[52] D. Tanre, M. Herman, and Y. J. Kaufman. Information on aerosol size distribution contained in solar reflected spectral radiances. *Journal of Geophysical Research-Atmospheres*, 101(D14):19043–19060, August 1996. ISSN 0148-0227. doi: 10.1029/96JD00333.

[53] Clive D. Rodgers. Intercomparison of remote sounding instruments. *Journal of Geophysical Research*, 108(D3), 2003. ISSN 0148-0227. doi: 10.1029/2002JD002299.

[54] Mihály Pósfai, Renáta Simonics, Jia Li, Peter V. Hobbs, and Peter R. Buseck. Individual aerosol particles from biomass burning in southern africa: 1. compositions and size distributions of carbonaceous particles. *Journal of Geophysical Research*, 108:13 PP., March 2003. doi: 200310.1029/2002JD002291. URL http://www.agu.org.ezproxy.cul.columbia.edu/pubs/crossref/2003/2002JD002291.shtml.

[55] M Posfai, A Gelencser, R Simonics, K Arato, J Li, PV Hobbs, and PR Buseck. Atmospheric tar balls: Particles from biomass and biofuel burning. *Journal of Geophysical Research-Atmospheres*, 109(D6), March 2004. ISSN 0148-0227. doi: 10.1029/2003JD004169. WOS:000220622900003.

[56] TC Bond and RW Bergstrom. Light absorption by carbonaceous particles: An investigative review. *Aerosol Science and Technology*, 40(1):27–67, January 2006. ISSN 0278-6826. doi: 10.1080/02786820500421521. WOS:000233906000001.

[57] Oleg Dubovik, Alexander Sinyuk, Tatyana Lapyonok, Brent N. Holben, Michael Mishchenko, Ping Yang, Tom F. Eck, Hester Volten, Olga Muñoz, Ben Veihelmann, Wim J. van der Zande, Jean-Francois Leon, Michael Sorokin, and Ilya Slutsker. Application of spheroid models to account for aerosol particle nonsphericity in remote sensing of desert dust. *Journal of Geophysical Research*, 111(D11), 2006. ISSN 0148-0227. doi: 10.1029/2005JD006619.

[58] K. Knobelspiesse, B. Cairns, J. Redemann, R. W. Bergstrom, and A. Stohl. Simultaneous retrieval of aerosol and cloud properties during the MILAGRO field campaign RID a-7535-2008. *Atmospheric Chemistry and Physics*, 11(13):6245–6263, 2011. ISSN 1680-7316.

[59] Otto P. Hasekamp, Pavel Litvinov, and André Butz. Aerosol properties over the ocean from PARASOL multiangle photopolarimetric measurements. *Journal of Geophysical Research: Atmospheres*, 116(D14):D14204, 2011. ISSN 2156-2202.

[60] Albert Tarantola. *Inverse problem theory and methods for model parameter estimation*. Society for Industrial and Applied Mathematics (SIAM), Philadelphia, PA, 2005. ISBN 0-89871-572-5.

[61] Database of aerosol spectral refractive indices.

[62] Alexander Marshak and Anthony Davis, editors. *3D Radiative Transfer in Cloudy Atmospheres*. Springer, 2005. ISBN 9783540285199.

[63] Michael A. Box. Radiative perturbation theory: a review. *Environmental Modelling & Software*, 17(1):95–106, 2002. ISSN 1364-8152.

[64] Vladimir V. Rozanov and Alexei V. Rozanov. Relationship between different approaches to derive weighting functions related to atmospheric remote sensing problems. *Journal of Quantitative Spectroscopy & Radiative Transfer*, 105(2):217–242, 2007. ISSN 0022-4073.

[65] O. Balima, Y. Favennec, J. Boulanger, and A. Charette. Optical tomography with the discontinuous Galerkin formulation of the radiative transfer equation in frequency domain. *Journal of Quantitative Spectroscopy & Radiative Transfer*, 113(10):805–814, 2012. ISSN 0022-4073.

[66] T. Saratoon, T. Tarvainen, B. T. Cox, and S. R. Arridge. A gradient-based method for quantitative photoacoustic tomography using the radiative transfer equation. *Inverse Problems*, 29(7):075006 (19pp), 2013. ISSN 0266-5611.

[67] OP Hasekamp and J Landgraf. Linearization of vector radiative transfer with respect to aerosol properties and its use in satellite remote sensing. *Journal of Geophysical Research-Atmospheres*, 110(D4):D04203, February 2005. ISSN 0148-0227.

[68] S. A. Ukhinov and D. I. Yurkov. Computation of the parametric derivatives of polarized radiation and the solution of inverse atmospheric optics problems. *Russian Journal of Numerical Analysis and Mathematical Modelling*, 17(3):283–303, 2002. ISSN 0927-6467.

[69] O. V. Postylyakov. Linearized vector radiative transfer model MCC++ for a spherical atmosphere. *Journal of Quantitative Spectroscopy & Radiative Transfer*, 88(1-3): 297–317, 2004. ISSN 0022-4073.

[70] R. J. D. Spurr, T. P. Kurosu, and K. V. Chance. A linearized discrete ordinate radiative transfer model for atmospheric remote-sensing retrieval. *Journal of Quantitative Spectroscopy & Radiative Transfer*, 68(6):689–735, 2001. ISSN 0022-4073.

[71] A. Doicu and T. Trautmann. Adjoint problem of radiative transfer for a pseudo-spherical atmosphere and general viewing geometries. *Journal of Quantitative Spectroscopy and Radiative Transfer*, 110(8):464–476, May 2009. ISSN 0022-4073.

[72] Holger H. Walter and Jochen Landgraf. Linearization of radiative transfer in spherical geometry: an application of the forward-adjoint perturbation theory. In Alexander A. Kokhanovsky, editor, *Light Scattering Reviews 5*, Springer Praxis Books, pages 105–145. Springer Berlin Heidelberg, January 2010. ISBN 978-3-642-10335-3, 978-3-642-10336-0.

[73] R. J. D. Spurr. Simultaneous derivation of intensities and weighting functions in a general pseudo-spherical discrete ordinate radiative transfer treatment. *Journal of Quantitative Spectroscopy & Radiative Transfer*, 75(2):129–175, 2002. ISSN 0022-4073.

[74] Igor N. Polonsky, Michael A. Box, and Anthony B. Davis. Radiative transfer through inhomogeneous turbid media: implementation of the adjoint perturbation approach at the first order. *Journal of Quantitative Spectroscopy and Radiative Transfer*, 78 (1):85–98, 2003. ISSN 0022-4073.

[75] Michael A. Box, Igor N. Polonsky, and Anthony B. Davis. Higher order perturbation theory applied to radiative transfer in non-plane-parallel media. *Journal of Quantitative Spectroscopy and Radiative Transfer*, 78(1):105–118, April 2003. ISSN 0022-4073.

[76] K. Franklin Evans. The spherical harmonics discrete ordinate method for three-dimensional atmospheric radiative transfer. *Journal of the Atmospheric Sciences*, 55 (3):429–446, February 1998. ISSN 0022-4928, 1520-0469.

[77] Robert Pincus and K. Franklin Evans. Computational cost and accuracy in calculating three-dimensional radiative transfer: Results for new implementations of monte carlo and SHDOM. *Journal of the Atmospheric Sciences*, 66(10):3131–3146, 2009. ISSN 0022-4928, 1520-0469.

[78] C. Emde, R. Buras, B. Mayer, and M. Blumthaler. The impact of aerosols on polarized sky radiance: model development, validation, and applications. *Atmospheric Chemistry & Physics*, 10(2):383–396, January 2010. ISSN 16807316.

[79] C. Cornet, L. C-Labonnote, and F. Szczap. Three-dimensional polarized monte carlo atmospheric radiative transfer model (3DMCPOL): 3D effects on polarized visible reflectances of a cirrus cloud. *Journal of Quantitative Spectroscopy & Radiative Transfer*, 111(1):174–186, January 2010. ISSN 0022-4073.

[80] Adrian Doicu, Dmitry Efremenko, and Thomas Trautmann. A multi-dimensional vector spherical harmonics discrete ordinate method for atmospheric radiative transfer. *Journal of Quantitative Spectroscopy and Radiative Transfer*, 118:121–131, March 2013. ISSN 0022-4073.

[81] K. Franklin Evans. Spherical harmonic discrete ordinate method for atmospheric radiative transfer. http://nit.colorado.edu/shdom.html, 2014. Accessed: March 7th 2014.

[82] Alexander Marshak, Steven Platnick, Tamás Várnai, Guoyong Wen, and Robert F. Cahalan. Impact of three-dimensional radiative effects on satellite retrievals of cloud droplet sizes. *Journal of Geophysical Research: Atmospheres*, 111(D9):D09207, 2006. ISSN 2156-2202.

[83] Zhibo Zhang and Steven Platnick. An assessment of differences between cloud effective particle radius retrievals for marine water clouds from three MODIS spectral bands. *Journal of Geophysical Research: Atmospheres*, 116(D20):D20215, 2011. ISSN 2156-2202.

[84] Amit Aides, Yoav Y. Schechner, Vadim Holodovsky, Michael J. Garay, and Anthony B. Davis. Multi sky-view 3D aerosol distribution recovery. *Optics Express*, 21 (22):25820–25833, 2013. ISSN 1094-4087.

[85] Ronald B. Guenther and John W. Lee. *Partial differential equations of mathematical physics and integral equations*. Dover Publications, New York, 1996. ISBN 0486688895. See Chapters 7-3 and 7-4, and Theorem 4-2.

[86] L Liu, MI Mishchenko, JW Hovenier, H Volten, and O Muñoz. Scattering matrix of quartz aerosols: comparison and synthesis of laboratory and Lorenz-Mie results RID b-4396-2010. *Journal of Quantitative Spectroscopy & Radiative Transfer*, 79: 911–920, September 2003. ISSN 0022-4073. doi: 10.1016/S0022-4073(02)00328-X. WOS:000182647500028.

[87] Li Liu and Michael I. Mishchenko. Scattering and radiative properties of complex soot and soot-containing aggregate particles. *Journal of Quantitative Spectroscopy and Radiative Transfer*, 106(1–3):262–273, July 2007. ISSN 0022-4073. doi: 10.1016/j.jqsrt.2007.01.020. URL http://www.sciencedirect.com/science/article/pii/S0022407307000350.

[88] Michael Kahnert, Timo Nousiainen, and Päivi Mauno. On the impact of nonsphericity and small-scale surface roughness on the optical properties of hematite aerosols. *Journal of Quantitative Spectroscopy and Radiative Transfer*, 112(11): 1815–1824, July 2011. ISSN 0022-4073. doi: 10.1016/j.jqsrt.2011.01.022.

[89] Charles A. Hall and W. Weston Meyer. Optimal error bounds for cubic spline interpolation. *Journal of Approximation Theory*, 16(2):105–122, 1976. ISSN 0021-9045. URL http://www.ams.org/mathscinet-getitem?mr=0397247.

[90] Peter Deuflhard and Andreas Hohmann. *Numerical analysis in modern scientific computing*, volume 43 of *Texts in Applied Mathematics*. Springer-Verlag, New York, second edition, 2003. ISBN 0-387-95410-4. An introduction.

[91] Michael I. Mishchenko, Larry D. Travis, and Andrew A. Lacis. *Scattering, Absorption, and Emission of Light by Small Particles*. Cambridge University Press, 2002. ISBN 9780521782524.

[92] MI Mishchenko and LD Travis. Capabilities and limitations of a current FORTRAN implementation of the t-matrix method for randomly oriented, rotationally symmetric scatterers RID b-4396-2010. *Journal of Quantitative Spectroscopy & Radiative Transfer*, 60(3):309–324, September 1998. ISSN 0022-4073. doi: 10.1016/S0022-4073(98)00008-9. WOS:000075518500003.

[93] David L. Phillips. A technique for the numerical solution of certain integral equations of the first kind. *Journal of the Association for Computing Machinery*, 9:84–97, 1962. ISSN 0004-5411.

[94] S. Twomey. On the numerical solution of fredholm integral equations of the first kind by the inversion of the linear system produced by quadrature. *Journal of the ACM*, 10(1):97–101, January 1963. ISSN 00045411. doi: 10.1145/321150.321157.

[95] Jorge J. Moré. The Levenberg-Marquardt algorithm: implementation and theory. In *Numerical analysis (Proc. 7th Biennial Conf., Univ. Dundee, Dundee, 1977)*, pages 105–116. Lecture Notes in Math., Vol. 630. Springer, Berlin, 1978.

[96] Jorge Nocedal and Stephen J Wright. *Numerical Optimization*. Springer series in operations research. Springer, New York, 2nd ed edition, 2006. ISBN 0387303030.

[97] P Romanov, NT O'Neill, A Royer, and BLJ McArthur. Simultaneous retrieval of aerosol refractive index and particle size distribution from ground-based measurements of direct and scattered solar radiation RID f-5622-2010. *Applied Optics*,

38(36):7305–7320, December 1999. ISSN 0003-6935. doi: 10.1364/AO.38.007305. WOS:000084484400001.

[98] Wilfred Kaplan. *Advanced calculus*. Addison-Wesley Publishing Company Advanced Book Program, Reading, MA, third edition, 1984. ISBN 0-201-11680-4.

Appendix A

Appendix single-scattering calculations

This Appendix develops the theoretical tools for characterizing spherical particles using multi-spectral polarimetric single-scattering measurements. The methods presented here permit the use of combined measurement sets and the retrieval of multiple modes of polydisperse and externally mixed spherical particles. Notwithstanding the significance of non-spherical particles like soot aggregates [86–88] and desert dust [57], here we restrict our attention to homogeneously mixed spherical particles — considering liquid water droplets, sea spray, sulfate aerosols and tar-balls. We do allow for particles with complex and wavelength dependent refractive indices, so long as the dependence is uniform over the particle volume. The scattering properties of a single spherical particle are computed as functions of the microphysical state variable, $\boldsymbol{\xi} = [r, a(\lambda), b(\lambda)]$, where r is particle radius and $m = a\,(\lambda) + \mathrm{i}b\,(\lambda)$ is the complex refractive index at wavelength λ using Lorenz-Mie theory. They are written as $C_\sigma\,(\lambda;\, \boldsymbol{\xi})$ and $\boldsymbol{F}_{\mathrm{mono}}\,(\lambda, \theta;\, \boldsymbol{\xi})$ to separate particle variables $\boldsymbol{\xi}$ from measurement variables λ and θ. The form of scattering matrix is simplified

in Lorenz-Mie scattering and requires only four linearly independent functions of the scattering angle θ [34],

$$\boldsymbol{F}_{\text{mono}}(\lambda,\theta;\boldsymbol{\xi}) = \begin{bmatrix} F_{11}(\lambda,\theta;\boldsymbol{\xi}) & F_{12}(\lambda,\theta;\boldsymbol{\xi}) & & \\ F_{12}(\lambda,\theta;\boldsymbol{\xi}) & F_{11}(\lambda,\theta;\boldsymbol{\xi}) & & \\ & & F_{33}(\lambda,\theta;\boldsymbol{\xi}) & F_{34}(\lambda,\theta;\boldsymbol{\xi}) \\ & & -F_{34}(\lambda,\theta;\boldsymbol{\xi}) & F_{33}(\lambda,\theta;\boldsymbol{\xi}) \end{bmatrix}. \tag{A.1}$$

Poly-disperse populations consisting of particles with different sizes and refractive indices are represented by a measure, $\mathrm{d}N(\boldsymbol{\xi})$, over the continuum of states, $\boldsymbol{\xi} \in \boldsymbol{\Xi}$. This differential form is defined explicitly in section A.2 and can be integrated over subsets of state space to obtain the number concentration of such particles. In particular, integrating over the entire state space gives the total number concentration.

$$N_0 = \int_{\boldsymbol{\Xi}} \mathrm{d}N(\boldsymbol{\xi}) \qquad \text{units of} \quad \left[\frac{\text{particles}}{\mathsf{cm}^3}\right] \tag{A.2}$$

The scattering of such poly-disperse populations is computed by solving macroscopic Maxwell's equations for one particle at a time and evaluating the integral over the measure, $\mathrm{d}N(\boldsymbol{\xi})$, numerically:

$$\sigma(\lambda) = \int_{\boldsymbol{\Xi}} \sigma_{\text{mono}}(\lambda;\boldsymbol{\xi})\,\mathrm{d}N(\boldsymbol{\xi}), \tag{A.3}$$

$$\boldsymbol{F}(\lambda,\theta) = \int_{\boldsymbol{\Xi}} \boldsymbol{F}_{\text{mono}}(\lambda,\theta;\boldsymbol{\xi})\,\mathrm{d}N(\boldsymbol{\xi}). \tag{A.4}$$

These equations are strictly valid for the average scattering of infinitely many particles for which measurements are made one particle at a time. However, single-scattering measurements are taken of widely separated particles by necessity, and this condition justifies the use of Eqs. (A.3) and (A.4) as valid approximations to what is observed by

in situ nephelometers [33].

Measurable quantities include the volume-scattering and volume-absorption coefficients,

$$\sigma_{\mathrm{sca}}(\lambda) = \frac{1}{2}\int_0^{\pi} F_{11}(\lambda,\theta)\sin(\theta)\,\mathrm{d}\theta, \tag{A.5}$$

$$\sigma_{\mathrm{abs}}(\lambda) = \beta_{\sigma}(\lambda) - \beta_{\mathrm{sca}}(\lambda), \tag{A.6}$$

and the following functions of the angularly sampled elements of the scattering matrix:

$$\log\left(\frac{F_{11}(\lambda,\theta)}{F_{11}(\lambda,30^{\circ})}\right), \qquad \frac{F_{33}(\lambda,\theta)}{F_{11}(\lambda,\theta)}, \qquad \frac{F_{12}(\lambda,\theta)}{F_{11}(\lambda,\theta)}, \qquad \frac{F_{34}(\lambda,\theta)}{F_{11}(\lambda,\theta)}. \tag{A.7}$$

The microphysical state density measure $\mathrm{d}N(\boldsymbol{\xi})$ is parametrized by the state vector $\boldsymbol{x} \in \mathbb{R}^N$, and a given subset of the single-scattering properties in Eqs. (A.5) - (A.7) that constitute a measurement set are represented by the measurement vector $\boldsymbol{y} \in \mathbb{R}^M$. Accounting for additive Gaussian random noise $\boldsymbol{\epsilon} \sim \mathrm{Normal}(\mathbf{0}, \boldsymbol{S}_{\boldsymbol{\epsilon}})$, the forward model $\boldsymbol{f} : \mathbb{R}^N \longrightarrow \mathbb{R}^M$ is what defines the relationship between the state vector $\boldsymbol{x}$ and the measurement vector $\boldsymbol{y}$:

$$\boldsymbol{y} = \boldsymbol{f}(\boldsymbol{x}) + \boldsymbol{\epsilon} \tag{A.8}$$

The definitions of various measurement sets are covered in Section A.1, and the definition of the state vector $\boldsymbol{x}$ is explained in Section A.2. The averaging of scattering properties over poly-disperse ensembles of airborne particles and completion of the forward model is contained in Section A.3. This includes the computation of the derivatives of measurable quantities with respect to particle parameters. The inversion methods and stability

analysis tools introduced in Section A.4 complete the discussion of methods used in this paper.

Notation. Scalar quantities will be written as upper or lowercase letters in non-bold font. Bold typesetting is reserved for vectors (lowercase) and matrices (uppercase). Derivatives are written as $\frac{\partial a}{\partial b}$, $\frac{\partial a}{\partial \boldsymbol{b}}$, $\frac{\partial \boldsymbol{a}}{\partial b}$, and $\frac{\partial \boldsymbol{a}}{\partial \boldsymbol{b}}$ — denoting scalar, vector, vector, and matrix quantities. Indices are used to denote one element in a set of scalars (non-bold), vectors (bold lowercase), or matrices (bold uppercase).

A.1 Light scattering measurables

We consider observation systems based on two different types of instruments for measuring polarized single scattering of visible light by airborne particles: photoacoustic-integrating nephelometers measure the quantities in Eqs. (A.5) and (A.6), and polar-angle-scattering nephelometers measure some, or all, of the quantities in Eq. (A.7). Photoacoustic-integrating nephelometers provide absolute measurements of optical cross-sections and will be denoted CS [39, 46, 47]. Polar-angle-scattering nephelometers provide relative angular profiles of scattering matrix elements and will be denoted by $\mathrm{SM}_{\mathrm{phase}}$, $\mathrm{SM}_{\mathrm{linear}}$, and $\mathrm{SM}_{\mathrm{full}}$ in order of increasing polarimetric completeness, or by SM in reference to all three [28, 31, 48]. The measurements are assumed to be made at the visible wavelengths 405 nm, 532 nm, and 780 nm. The angular sampling for polar-angle-scattering measurements (denoted SM in reference to all three) consists of 51 angles spanning the range 3° - 177° with 1° resolution in forward and backward scattering directions and 5° resolution in side scattering directions. The angles are identical to those reported for the water droplet test case in [48].

The measurement sets considered are outlined in Table A.1 showing the number of constraints imposed by each data set. For each, the measurement vector is a simple concate-

TABLE A.1: Measurement constraints for the six subsets of complete single-scattering properties

	M	σ_{sca}	σ_{abs}	$\log\left(\frac{F_{11}(\boldsymbol{\theta})}{F_{11}(30^\circ)}\right)$	$\frac{F_{33}(\boldsymbol{\theta})}{F_{11}(\boldsymbol{\theta})}$	$\frac{F_{12}(\boldsymbol{\theta})}{F_{11}(\boldsymbol{\theta})}$	$\frac{F_{34}(\boldsymbol{\theta})}{F_{11}(\boldsymbol{\theta})}$
SM_{phase}	153			$3_\lambda \times 51_{\boldsymbol{\theta}}$			
+ CS	159	3_λ	3_λ	$3_\lambda \times 51_{\boldsymbol{\theta}}$			
$\text{SM}_{\text{linear}}$	306			$3_\lambda \times 51_{\boldsymbol{\theta}}$		$3_\lambda \times 51_{\boldsymbol{\theta}}$	
+ CS	312	3_λ	3_λ	$3_\lambda \times 51_{\boldsymbol{\theta}}$		$3_\lambda \times 51_{\boldsymbol{\theta}}$	
SM_{full}	612			$3_\lambda \times 51_{\boldsymbol{\theta}}$	$3_\lambda \times 51_{\boldsymbol{\theta}}$	$3_\lambda \times 51_{\boldsymbol{\theta}}$	$3_\lambda \times 51_{\boldsymbol{\theta}}$
+ CS	618	3_λ	3_λ	$3_\lambda \times 51_{\boldsymbol{\theta}}$	$3_\lambda \times 51_{\boldsymbol{\theta}}$	$3_\lambda \times 51_{\boldsymbol{\theta}}$	$3_\lambda \times 51_{\boldsymbol{\theta}}$

nation of light scattering data from one or more included subsets, indexed by $i : 0 \leq i < I$ through the total number of subsets I,

$$\boldsymbol{y} = \left[\begin{array}{ccccccc} \boldsymbol{y}_0 & \boldsymbol{y}_1 & \cdots & \boldsymbol{y}_i & \cdots & \boldsymbol{y}_{I-1} \end{array} \right]. \tag{A.9}$$

The measurement subset vector is denoted, $\boldsymbol{y}_i = (y_i^{m'})$ for $0 \leq m' < M_i$, and the complete measurement vector is denoted, $\boldsymbol{y} = (y^m)$ for $0 \leq m < M$.

The inter-comparison of instrument design capabilities requires realistic measurement error covariance matrices for each measurement set. Error is modeled using a multivariate Gaussian model. For the i^{th} data subset, the error is modeled as $\boldsymbol{\epsilon}_i \sim \text{Normal}\,(\mathbf{0}, \boldsymbol{S}_{\boldsymbol{\epsilon}_i})$. The measurement error for combined data sets is $\boldsymbol{\epsilon} \sim \text{Normal}\,(\mathbf{0}, \boldsymbol{S}_{\boldsymbol{\epsilon}})$,

$$\boldsymbol{\epsilon} = \left[\begin{array}{ccccccc} \boldsymbol{\epsilon}_0 & \boldsymbol{\epsilon}_1 & \cdots & \boldsymbol{\epsilon}_i & \cdots & \boldsymbol{\epsilon}_{I-1} \end{array} \right]. \tag{A.10}$$

The relative measurement errors for optical cross sections CS are found in [46], and the measurement errors for normalized scattering matrix elements SM are derived from the results presented in [48]. Specifically, the diagonal measurement error covariance matrix

elements for a water droplet test case were used to determine an empirical rule for error as a function of signal. The off-diagonal elements of the corresponding covariance matrices are therefore not considered in the current theoretical exercise since correlations between measurements can either increase or decrease the information content of the measurement set depending on the strength of the correlations [50, 58].

A.2 Particle microphysical parametrization

The population of particles within an observed scattering volume is assumed to result from an external mixture of homogeneous spherical particles grouped into one or more *modes*, according to the characteristic spectral signature of complex refractive index. Particles with internally heterogeneous refractive index is not considered here. Nevertheless, the treatment of external mixing permits us to retrieve microphysical properties for similarly sized particle populations based on distinct signatures in spectrally dependent refractive index. Previous treatments have assumed that only a single spectrally dependent refractive index is present [36, 57] or that particle refractive index is a function of size, and make allowance for coarse and fine mode aerosols with distinct refractive indices [50, 58].

Table A.2: Microphysical parameterizations under consideration and prior information. Spectral averages are shown for refractive index prior information.

Population	N	N_ς	$N_{\boldsymbol{p}}$	$N_{\boldsymbol{a}}$	$N_{\boldsymbol{b}}$	radius [nm]	$\langle a \rangle$; $\langle \sigma_a \rangle$	$\langle b \rangle$; $\langle \sigma_b \rangle$
Water	28	1	21	3	3	0.01-16	1.33; 1e-5	5e-8; 2e-9
Sea spray	28	1	21	3	3	0.01-16	1.41; 0.02	1e-7; 4e-8
Sulfate	26	1	19	3	3	0.006-1.75	1.44; 0.02	8e-8; 4e-11
Tar-balls	26	1	19	3	3	0.006-1.75	1.78; 0.1	0.005; 0.002
Tar-balls + sulfate	52	2	38	6	6			
Tar-balls + sea spray	54	2	40	6	6			

External mixtures of more than one type of particle are stored in a single vector of N unknowns, composed by the concatenation of mode parameter vectors $\boldsymbol{x}_j$ for $0 \leq j < J$:

$$\boldsymbol{x} = \left[\begin{array}{ccccccc} \boldsymbol{x}_0 & \boldsymbol{x}_1 & \cdots & \boldsymbol{x}_j & \cdots & \boldsymbol{x}_{J-1} \end{array} \right]. \tag{A.11}$$

Microphysical parameters for each mode are stored in $\boldsymbol{x}_j$ as the elements x_j^n for $0 \leq n < N_j$ and the entire set of microphysical parameters $\boldsymbol{x}$ has elements x^n for $0 \leq n < N$. The number of unknown parameters for a given microphysical state space is N. Each mode's parameter vector is written as the concatenation of loading, size distribution, and refractive index:

$$\boldsymbol{x}_j = \left[\begin{array}{ccc} \varsigma_j & \boldsymbol{p}_j & \boldsymbol{q}_j \end{array} \right]. \tag{A.12}$$

The loading of particles is described by the scalar ς_j with units $[\mu\mathrm{m}^2\mathrm{cm}^{-3}]$. The size distribution is expanded in a basis of smooth compactly supported polynomials with coefficients p_j^k stored in the vector $\boldsymbol{p}_j$ for each mode $0 \leq j < J$:

$$\boldsymbol{p}_j = \left[\begin{array}{ccccccc} p_j^0 & p_j^1 & \cdots & p_j^k & \cdots & p_j^{K_j-1} \end{array} \right]. \tag{A.13}$$

The refractive indices at various wavelengths are stored in the vector $\boldsymbol{q}_j$. Writing the real and imaginary parts of the refractive index, $m(\lambda) = a(\lambda) + \mathrm{i}b(\lambda)$, these values are stored in $\boldsymbol{q}$ at the wavelengths needed for all the measurements:

$$\boldsymbol{q}_j = \left[\begin{array}{ccccccccc} a_j(\lambda_0) & b_j(\lambda_0) & \ldots & a_j(\lambda_\ell) & b_j(\lambda_\ell) & \ldots & a_j(\lambda_{L-1}) & b_j(\lambda_{L-1}) \end{array} \right]. \tag{A.14}$$

The whole purpose is to numerically represent the measure of particle state number

density per unit volume, $\mathrm{d}N\left(\boldsymbol{\xi}\right)$, which is constructed from the microphysical parameters introduced in Eqs. (A.11) - (A.14) as follows,

$$\mathrm{d}N\left(\boldsymbol{\xi}\right) = \sum_{j=0}^{J-1} \delta\left(a - a_j(\lambda)\right)\ \delta\left(b - b_j(\lambda)\right)\ \mathrm{d}a\ \mathrm{d}b\ \mathrm{d}N_j\left(r\right). \tag{A.15}$$

The size distribution $\mathrm{d}N_j\left(r\right)$ is expanded in a basis of cubic b-splines[1][89, 90] as,

$$\mathrm{d}N_j\left(r\right) = \varsigma_j \sum_{k=0}^{K_j-1} p_j^k\ \varphi_{jk}\left(r\right)\mathrm{d}r, \tag{A.16}$$

where the basis functions $\varphi_{jk}(r)$ are normalized so that,

$$1 = \int_0^\infty \pi r^2 \varphi_{jk}(r)\ \mathrm{d}r. \tag{A.17}$$

The coefficients are also normalized such that $1 = \sum_{k=0}^{K_j-1} p_j^k$, which means that the particle geometric cross-section density is determined by the loading parameter ς_j for each mode $j : 0 \leq j < J$,

$$\varsigma_j = \int_0^\infty \pi r^2 \mathrm{d}N_j\left(r\right). \tag{A.18}$$

The stability analysis requires linearization about a mean prior state, and the definition of variability about the mean — against which the posterior variability is compared. Smoothness and normalization are controlled by additional constraints that are imposed by pseudo-measurement methods as described in [26, 36]. In addition, each mode's characteristic refractive index (mean and variance) is chosen to be representative of a specific class of spherical particle in the atmosphere. Pseudo-measurement functions

[1]polynomials which are piecewise-smooth, compactly supported, and mostly non-overlapping.

$\boldsymbol{h}_l : \mathbb{R}^{N_j} \longrightarrow \mathbb{R}^{\tilde{M}_l}$ are non-linear functions of each mode's microphysical parameters, whose values are imposed as Gaussian random vectors, $\boldsymbol{h}_l\left(\boldsymbol{x}_j\right) \sim \text{Normal}\big(\tilde{\boldsymbol{\mu}}_{lj}, \tilde{\boldsymbol{S}}_{lj}\big)$. There are five such pseudo-measurements used in this study. The first pseudo-measurement enforces positivity of loading parameters:

$$\boldsymbol{h}_0\left(\boldsymbol{x}_j\right) = \log\left(\varsigma_j\right). \tag{A.19}$$

The next three pseudo-measurements constrain the coefficients of the size distribution by enforcing positivity,

$$\boldsymbol{h}_1\left(\boldsymbol{x}_j\right) = \left[\begin{array}{ccccccc} \log\left(p_j^0\right) & \cdots & \log\left(p_j^k\right) & \cdots & \log\left(p_j^{K_j-1}\right) \end{array}\right], \tag{A.20}$$

normalization,

$$\boldsymbol{h}_2\left(\boldsymbol{x}_j\right) = \sum_{k=0}^{K_j-1} p_j^k\,, \tag{A.21}$$

and smoothness,

$$\boldsymbol{h}_3\left(\boldsymbol{x}_j\right) = \left(\sum_{k=0}^{K_j-1}\sum_{k'=0}^{K_j-1} H_{jk'k}\; p_j^k\; p_j^{k'}\right)^{\frac{1}{2}}, \tag{A.22}$$

where the weighting $H_{jkk'}$ imposes prior constraints on the smoothness of the volume (or mass) probability density function as a function of $\log(r)$:

$$H_{jkk'} = \int_{\mathbb{R}} \frac{\partial\left(\frac{4}{3}\pi r^3 \varphi_{jk}\right)}{\partial \log r} \frac{\partial\left(\frac{4}{3}\pi r^3 \varphi_{jk'}\right)}{\partial \log r} \mathrm{d}\log r\,. \tag{A.23}$$

The last pseudo-measurement constraint requires that the real refractive index is greater than one and that the imaginary refractive index is positive:

$$\boldsymbol{h}_4\left(\boldsymbol{x}_j\right) = \log\Big(\ \boldsymbol{q}_j - \begin{bmatrix} 1 & 0 & 1 & 0 & \cdots & 1 & 0 \end{bmatrix}\ \Big). \tag{A.24}$$

Analogous to the treatment for true measurements, we define the prior objective function, $\Phi_{\text{prior}}\left(\boldsymbol{x}\right)$, as follows:

$$\Phi_{\text{prior}}\left(\boldsymbol{x}\right) = \frac{1}{2}\sum_{l=0}^{4}\sum_{j=0}^{J-1}\left(\boldsymbol{h}_l\left(\boldsymbol{x}_j(\boldsymbol{x})\right) - \tilde{\boldsymbol{\mu}}_{lj}\right)^{\mathrm{T}}\ \tilde{\boldsymbol{S}}_{lj}^{-1}\ \left(\boldsymbol{h}_l\left(\boldsymbol{x}_j(\boldsymbol{x})\right) - \tilde{\boldsymbol{\mu}}_{lj}\right)\ . \tag{A.25}$$

This expression is simplified by concatenating the pseudo-measurement functions after subtracting by the mean:

$$\boldsymbol{h}(\boldsymbol{x}) = \begin{bmatrix} \boldsymbol{h}_0\left(\boldsymbol{x}_0(\boldsymbol{x})\right) - \tilde{\boldsymbol{\mu}}_{00} \\ \boldsymbol{h}_1\left(\boldsymbol{x}_0(\boldsymbol{x})\right) - \tilde{\boldsymbol{\mu}}_{10} \\ \vdots \\ \boldsymbol{h}_4\left(\boldsymbol{x}_0(\boldsymbol{x})\right) - \tilde{\boldsymbol{\mu}}_{40} \\ \boldsymbol{h}_0\left(\boldsymbol{x}_1(\boldsymbol{x})\right) - \tilde{\boldsymbol{\mu}}_{01} \\ \vdots \\ \boldsymbol{h}_l\left(\boldsymbol{x}_j(\boldsymbol{x})\right) - \tilde{\boldsymbol{\mu}}_{lj} \\ \vdots \\ \boldsymbol{h}_4\left(\boldsymbol{x}_{J-1}(\boldsymbol{x})\right) - \tilde{\boldsymbol{\mu}}_{4(J-1)} \end{bmatrix}. \tag{A.26}$$

The covariance matrix, $\boldsymbol{S}_{\boldsymbol{h}}$, of this pseudo-measurement vector, $\boldsymbol{h}$, is the block-diagonal matrix for which the following expression is equivalent to Eq. (A.25):

$$\Phi_{\text{prior}}\left(\boldsymbol{x}\right) = \frac{1}{2}\boldsymbol{h}(\boldsymbol{x})^{\mathrm{T}}\ \boldsymbol{S}_{\boldsymbol{h}}^{-1}\ \boldsymbol{h}(\boldsymbol{x}). \tag{A.27}$$

The prior state is selected by minimizing the objective function in Eq. (A.27),

$$\boldsymbol{x}_{\text{prior}} = \arg\min_{\boldsymbol{x}} \left(\Phi_{\text{prior}}\left(\boldsymbol{x}\right) \right), \tag{A.28}$$

and this prior state has a covariance matrix, $\boldsymbol{S}_{\text{prior}}(\boldsymbol{x}_{\text{prior}})$, that can be calculated by linearization as follows:

$$\boldsymbol{S}^{-1}_{\text{prior}}(\boldsymbol{x}_{\text{prior}}) = \frac{\partial \boldsymbol{h}(\boldsymbol{x}_{\text{prior}})}{\partial \boldsymbol{x}}^{\text{T}} \boldsymbol{S}^{-1}_{\boldsymbol{h}} \frac{\partial \boldsymbol{h}(\boldsymbol{x}_{\text{prior}})}{\partial \boldsymbol{x}}. \tag{A.29}$$

Beyond the assumptions that particles are spherical and have a smooth, compactly supported size distribution on the intervals specified in Table A.2, this mean microphysical state and covariance matrix quantify all of the prior information that is used for a given external mixture of particle modes.

A.3 Physics and forward modeling

This section describes the methods for computing the measurable quantities of scattered light defined in Section A.1 from the microphysical parameterization of spherical particles given in Section A.2. The following formalism is used to model the measurement vector $\boldsymbol{y}$ using the forward model function $\boldsymbol{f} : \mathbb{R}^N \longrightarrow \mathbb{R}^M$ and the vector of particle microphysical parameters $\boldsymbol{x}$. We focus on evaluating the measurement operator $\boldsymbol{f}\left(\boldsymbol{x}\right)$ and its derivative $\frac{\partial \boldsymbol{f}}{\partial \boldsymbol{x}}\left(\boldsymbol{x}\right)$ in order to retrieve particle properties and characterize uncertainty,

$$\boldsymbol{f}\left(\boldsymbol{x}\right) = \left[\begin{array}{ccccccc} \boldsymbol{f}_0\left(\boldsymbol{g}(\boldsymbol{x})\right) & \boldsymbol{f}_1\left(\boldsymbol{g}(\boldsymbol{x})\right) & \cdots & \boldsymbol{f}_i\left(\boldsymbol{g}(\boldsymbol{x})\right) & \cdots & \boldsymbol{f}_{I-1}\left(\boldsymbol{g}(\boldsymbol{x})\right) \end{array} \right]. \tag{A.30}$$

The model for the specific measurement set $\boldsymbol{y}_i$ is written as $\boldsymbol{f}_i(\boldsymbol{g}(\boldsymbol{x}))$ where $\boldsymbol{g}$ is an intermediate representation of the single-scattering properties stored as the basis-function coefficients of generalized spherical functions (GSF) [33]. The explicit dependence on the intermediate representation increases flexibility, since it permits the computation of any single-scattering measurement from the vector of coefficients, $\boldsymbol{g}$.

The scattering behavior for the distribution of sizes is computed as the average of the individual particles. The forward model uses Lorenz-Mie codes developed by Mishchenko [91] in conjunction with the work of [92] to compute the scattering due to mono-disperse spheres. The resulting output includes the extinction and scattering cross-sections $C_\sigma(\lambda, r, a, b)$, $C_{\text{sca}}(\lambda, r, a, b)$, and the GSF representation of the normalized scattering matrix. Using the notation of [92], these GSF coefficients are written $\alpha_1^{s'}(\lambda, r, a, b)$, $\alpha_2^{s'}(\lambda, r, a, b)$, $\alpha_3^{s'}(\lambda, r, a, b)$, $\alpha_4^{s'}(\lambda, r, a, b)$, $\beta_1^{s'}(\lambda, r, a, b)$, and $\beta_2^{s'}(\lambda, r, a, b)$ for non-negligible orders $0 \leq s' < S'$. To scale the scattering output to units of cross-section per particle and facilitate the computation of average scattering we define the array of mono-disperse single scattering properties as follows:

$$\boldsymbol{g}_{\text{mono}}(\lambda; r, a, b) = C_{\text{sca}}(\lambda, r, a, b) \begin{bmatrix} \alpha_1^0 & & \cdots & & \alpha_1^{s'} & \cdots & \alpha_1^{S'-1} \\ 0 & 0 & \alpha_2^2 & \cdots & \alpha_2^{s'} & \cdots & \alpha_2^{S'-1} \\ 0 & 0 & \alpha_3^2 & \cdots & \alpha_3^{s'} & \cdots & \alpha_3^{S'-1} \\ \alpha_4^0 & & \cdots & & \alpha_4^{s'} & \cdots & \alpha_4^{S'-1} \\ 0 & 0 & \beta_1^2 & \cdots & \beta_1^{s'} & \cdots & \beta_1^{S'-1} \\ \frac{C_\sigma(\lambda,r,a,b)}{C_{\text{sca}}(\lambda,r,a,b)} & 0 & \beta_2^2 & \cdots & \beta_2^{s'} & \cdots & \beta_2^{S'-1} \end{bmatrix}. \quad \text{(A.31)}$$

Although written as a matrix in Eq. (A.31) and discussed with elements conveniently denoted $g_{\text{mono}}^{t's'}$, the presentation of derivative calculations requires that $\boldsymbol{g}_{\text{mono}}$ be the vector

constructed by concatenating the rows of the matrix, and for this reason we use the lowercase symbol $\boldsymbol{g}$.

Averaging the mono-disperse scattering array $\boldsymbol{g}_{\text{mono}}(\lambda;\boldsymbol{\xi})$ over the microphysical state density measure $\mathrm{d}N\left(\boldsymbol{\xi}\right)$ and tabulating on a grid of refractive indices generates a database for interpolation with scattering stored in terms of the generalized spherical functions [33]. The scattering vector for an external mixture is written for each wavelength λ^{ℓ} using the definition of $\mathrm{d}N\left(\boldsymbol{\xi}\right)$ in Eqs. (A.15) and (A.16),

$$\boldsymbol{g}^{\ell}\left(\boldsymbol{x}\right) = \int_{\boldsymbol{\Xi}} \boldsymbol{g}_{\text{mono}}\left(\lambda^{\ell};r,a,b\right)\mathrm{d}N\left(\boldsymbol{\xi}\right) \tag{A.32}$$

$$= \sum_{j=0}^{J-1}\int_{r_{\min}}^{r_{\max}}\int_{0}^{\infty}\int_{1}^{\infty}\boldsymbol{g}_{\text{mono}}\left(\lambda^{\ell};r,a,b\right)\ \delta\left(a-a_{j}(\lambda^{\ell})\right)\ \delta\left(b-b_{j}(\lambda^{\ell})\right)\ \mathrm{d}a\,\mathrm{d}b\,\mathrm{d}N_{j}\left(r\right) \tag{A.33}$$

$$= \sum_{j=0}^{J-1}\int_{r_{\min}}^{r_{\max}}\boldsymbol{g}_{\text{mono}}\left(\lambda^{\ell};r,a(\lambda^{\ell}),b(\lambda^{\ell})\right)\ \left(\varsigma^{j}\sum_{k=0}^{K_{j}-1}p_{j}^{k}\varphi_{jk}\left(r\right)\right)\ \mathrm{d}r, \tag{A.34}$$

and simplified using linearity to a weighted sum of scattering kernels:

$$\boldsymbol{g}^{\ell}\left(\boldsymbol{x}\right) = \sum_{j=0}^{J-1}\varsigma^{j}\sum_{k=0}^{K_{j}-1}p_{j}^{k}\int_{r_{\min}}^{r_{\max}}\boldsymbol{g}_{\text{mono}}\left(\lambda^{\ell};r,a(\lambda^{\ell}),b(\lambda^{\ell})\right)\ \varphi_{jk}\left(r\right)\ \mathrm{d}r. \tag{A.35}$$

These scattering kernels are precomputed for each wavelength of light $\lambda^{\ell}:0\leq\ell<3$ and for each basis function φ_{jk}:

$$\boldsymbol{g}_{jk}^{\ell}\left(\boldsymbol{q}_{j}\right) = \int_{0}^{\infty}\boldsymbol{g}_{\text{mono}}\left(\lambda^{\ell};r,a^{\ell}(\boldsymbol{q}_{j}),b^{\ell}(\boldsymbol{q}_{j})\right)\ \varphi_{jk}\left(r\right)\ \mathrm{d}r\,. \tag{A.36}$$

They are tabulated on a grid of refractive indices and correspond each mode, j for $0\leq j<J$, and each polynomial b-spline basis function, k for $0\leq k<K_{j}$. Concatenating all wavelengths together allows us to write the scattering kernels as vector valued functions

of refractive index,

$$\boldsymbol{g}_{jk}(\boldsymbol{q}_j) = \left[\begin{array}{ccc} \boldsymbol{g}^0_{jk}(\boldsymbol{q}_j) & \boldsymbol{g}^1_{jk}(\boldsymbol{q}_j) & \boldsymbol{g}^2_{jk}(\boldsymbol{q}_j) \end{array} \right]. \tag{A.37}$$

This permits the computation of the complete set of intermediate single-scattering properties in the GSF representation through evaluation of $\boldsymbol{g}(\boldsymbol{x})$ for any state vector $\boldsymbol{x}$:

$$\boldsymbol{g}(\boldsymbol{x}) = \sum_{j=0}^{J-1} \varsigma^j(\boldsymbol{x}) \sum_{k=0}^{K_j-1} p_j^k(\boldsymbol{x})\, \boldsymbol{g}_{jk}(\boldsymbol{q}_j(\boldsymbol{x})). \tag{A.38}$$

The mode-specific information in $\boldsymbol{x}$ is unwrapped by functions $\varsigma^j(\boldsymbol{x})$, $p_j^k(\boldsymbol{x})$ and $\boldsymbol{q}_j(\boldsymbol{x})$; the scattering kernels are approximated by interpolation on a grid of refractive indices, $\boldsymbol{g}_{jk}(\boldsymbol{q}_j)$; and these are weighted and summed to yield the single-scattering properties, $\boldsymbol{g}(\boldsymbol{x})$. The elements of this vector of GSF coefficients will be written as $g^{\ell t' s'}(\boldsymbol{x})$ for the wavelength λ^ℓ specified by $\ell : 0 \leq \ell < 3$, the type of GSF function specified by $t' : 0 \leq t' < 6$ and the order of GSF function specified by $s' : 0 \leq s' < S' - 1$.

Thus, the first part of the forward model from Eq. (A.30) is defined by $\boldsymbol{g}(\boldsymbol{x})$ in Eq. (A.38). The next task is to write single-scattering measurements as functions of the coefficients of the GSF, $\boldsymbol{g}$. The volume-scattering coefficient is,

$$\sigma^\ell_{\text{sca}}(\boldsymbol{x}) = g^{\ell 00}(\boldsymbol{x}), \tag{A.39}$$

and the volume-absorption coefficient is,

$$\sigma^\ell_{\text{abs}}(\boldsymbol{x}) = g^{\ell 50}(\boldsymbol{x}) - g^{\ell 00}(\boldsymbol{x}). \tag{A.40}$$

Evaluating the scattering matrix elements at the angles of measurements requires calculating the GSF at those angles, $\boldsymbol{\theta} = (\theta^s)$ for $0 \leq s < S$. The GSF values at these angles are then used to construct an array that acts linearly on the coefficient vector, $\boldsymbol{g}$, to calculate the angularly-dependent scattering matrix elements. The required array is expressed as the product of three matrices:

$$A\left(\boldsymbol{\theta}\right)^{ts}_{t's'} = \begin{pmatrix} 1 & & & & & & \\ & \frac{1}{2} & \frac{1}{2} & & & & \\ & \frac{1}{2} & -\frac{1}{2} & & & & \\ & & & 1 & & & \\ & & & & 1 & & \\ & & & & & 1 & \end{pmatrix}^{t}_{t''} \begin{pmatrix} P^{s'}_{00}(\theta^s) & & & & & & \\ & P^{s'}_{22}(\theta^s) & & & & & \\ & & P^{s'}_{2-2}(\theta^s) & & & & \\ & & & P^{s'}_{00}(\theta^s) & & & \\ & & & & P^{s'}_{02}(\theta^s) & & \\ & & & & & P^{s'}_{02}(\theta^s) & \end{pmatrix}^{t''s}_{t'''s'} \begin{pmatrix} 1 & & & & & & \\ & 1 & 1 & & & & \\ & 1 & -1 & & & & \\ & & & 1 & & & \\ & & & & 1 & & \\ & & & & & 1 & \end{pmatrix}^{t'''}_{t'}, \tag{A.41}$$

where matrix multiplication implies summation over the indices t'' and t'''. These coefficients determine the weight of the $(t's')^{\text{th}}$ generalized spherical function coefficient when summing to calculate the t^{th} scattering matrix element (ordered $0 \leq t < 6$ for the elements F_{11}, F_{22},F_{33}, F_{44},F_{12}, and F_{34}), evaluated at the s^{th} scattering angle. The measurables for this study are computed with the following expressions:

$$\log\left(\frac{F_{11}\left(\lambda^\ell, \theta^s\right)}{F_{11}\left(\lambda^\ell, \theta{=}30^\circ\right)}\right) = \log\left(\frac{\sum_{t'=0}^{5}\sum_{s'=0}^{S'-1} A(\boldsymbol{\theta})^{0\,s}_{t's'} g^{\ell t's'}}{\sum_{t'=0}^{5}\sum_{s'=0}^{S'-1} A(30^\circ)^{0\,0}_{t's'} g^{\ell t's'}}\right), \tag{A.42}$$

$$\frac{F_{33}\left(\lambda^\ell, \theta^s\right)}{F_{11}\left(\lambda^\ell, \theta^s\right)} = \frac{\sum_{t'=0}^{5}\sum_{s'=0}^{S'-1} A(\boldsymbol{\theta})^{2\,s}_{t's'} g^{\ell t's'}}{\sum_{t'=0}^{5}\sum_{s'=0}^{S'-1} A(\boldsymbol{\theta})^{0\,s}_{t's'} g^{\ell t's'}}, \tag{A.43}$$

$$\frac{F_{12}\left(\lambda^\ell, \theta^s\right)}{F_{11}\left(\lambda^\ell, \theta^s\right)} = \frac{\sum_{t'=0}^{5}\sum_{s'=0}^{S'-1} A(\boldsymbol{\theta})^{4\,s}_{t's'} g^{\ell t's'}}{\sum_{t'=0}^{5}\sum_{s'=0}^{S'-1} A(\boldsymbol{\theta})^{0\,s}_{t's'} g^{\ell t's'}}, \tag{A.44}$$

$$\frac{F_{34}\left(\lambda^\ell, \theta^s\right)}{F_{11}\left(\lambda^\ell, \theta^s\right)} = \frac{\sum_{t'=0}^{5}\sum_{s'=0}^{S'-1} A(\boldsymbol{\theta})^{5\,s}_{t's'} g^{\ell t's'}}{\sum_{t'=0}^{5}\sum_{s'=0}^{S'-1} A(\boldsymbol{\theta})^{0\,s}_{t's'} g^{\ell t's'}}. \tag{A.45}$$

When a measurement set includes such measurements as those given by Eqs. (A.39) - (A.45), the output arrays are shaped into the vector valued functions $\boldsymbol{f}_i : \boldsymbol{g} \mapsto \boldsymbol{y}_i$ so as to construct the forward model $\boldsymbol{f} : \boldsymbol{x} \mapsto \boldsymbol{y}$ as in Eq. (A.30) with intermediate GSF representation given by Eq. (A.38):

$$\boldsymbol{f}(\boldsymbol{x}) = \left[\begin{array}{cccccc} \boldsymbol{f}_0\big(\boldsymbol{g}(\boldsymbol{x})\big) & \boldsymbol{f}_1\big(\boldsymbol{g}(\boldsymbol{x})\big) & \cdots & \boldsymbol{f}_i\big(\boldsymbol{g}(\boldsymbol{x})\big) & \cdots & \boldsymbol{f}_{I-1}\big(\boldsymbol{g}(\boldsymbol{x})\big) \end{array} \right], \tag{A.46}$$

$$\boldsymbol{g}(\boldsymbol{x}) = \sum_{j=0}^{J-1} \varsigma^j(\boldsymbol{x}) \sum_{k=0}^{K_j-1} p_j^k(\boldsymbol{x}) \boldsymbol{g}_{jk}\left(\boldsymbol{q}_j(\boldsymbol{x})\right). \tag{A.47}$$

These equations are repeated to facilitate comparison with the derivative of the forward model with respect to microphysical state, $\frac{\partial \boldsymbol{f}(\boldsymbol{x})}{\partial \boldsymbol{x}}$. This $M \times N$ matrix specifies how small perturbations in particle microphysics will affect the predicted measurements, and it is computed using chain rule:

$$\frac{\partial \boldsymbol{f}(\boldsymbol{x})}{\partial \boldsymbol{x}} = \sum_{i=0}^{I-1} \frac{\partial \boldsymbol{f}}{\partial \boldsymbol{f}_i} \frac{\partial \boldsymbol{f}_i}{\partial \boldsymbol{g}} \sum_{j=0}^{J-1} \Bigg[\left(\sum_{k=0}^{K_j-1} p_j^k(\boldsymbol{x}) \boldsymbol{g}_{jk}\left(\boldsymbol{q}_j(\boldsymbol{x})\right) \right) \otimes \frac{\partial \varsigma^j(\boldsymbol{x})}{\partial \boldsymbol{x}} + \cdots \tag{A.48}$$

$$+ \varsigma^j(\boldsymbol{x}) \left(\sum_{k=0}^{K_j-1} \boldsymbol{g}_{jk}\left(\boldsymbol{q}_j(\boldsymbol{x})\right) \otimes \frac{\partial p_j^k(\boldsymbol{x})}{\partial \boldsymbol{x}} \right) + \cdots \tag{A.49}$$

$$+ \varsigma^j(\boldsymbol{x}) \left(\sum_{k=0}^{K_j-1} p_j^k(\boldsymbol{x}) \frac{\partial \boldsymbol{g}_{jk}}{\partial \boldsymbol{q}_j} \right) \frac{\partial \boldsymbol{q}_j(\boldsymbol{x})}{\partial \boldsymbol{x}} \Bigg]. \tag{A.50}$$

The symbol $\otimes$ denotes the *outer product* of vectors and is defined as $(\boldsymbol{a} \otimes \boldsymbol{b})^{ij} = a^i b^j$. These tools enable the computation of any type of optical measurement, and the derivatives of those measurements with respect to the microphysical parameters.

A.4 Inverse problem and numerical optimization

Numerical optimization routines are used to fit microphysical parameters to data by minimizing the objective function. These routines require that the objective function be properly scaled and that any constraints on parameters be explicitly defined [93–96]. The objective function and its derivative are written out as follows:

$$\Phi\left(\boldsymbol{x}\right) = \Phi_{\text{data}}\left(\boldsymbol{x}\right) + \Phi_{\text{prior}}\left(\boldsymbol{x}\right), \tag{A.51}$$

$$= \frac{1}{2}\left(\left(\boldsymbol{f}\left(\boldsymbol{x}\right) - \boldsymbol{y}\right)^{\mathrm{T}} \boldsymbol{S}_{\boldsymbol{\epsilon}}^{-1}\left(\boldsymbol{f}\left(\boldsymbol{x}\right) - \boldsymbol{y}\right) + \boldsymbol{h}(\boldsymbol{x})^{\mathrm{T}}\ \boldsymbol{S}_{\boldsymbol{h}}^{-1}\ \boldsymbol{h}(\boldsymbol{x})\right), \tag{A.52}$$

$$\frac{\partial \Phi(\boldsymbol{x})}{\partial \boldsymbol{x}} = \left(\boldsymbol{f}\left(\boldsymbol{x}\right) - \boldsymbol{y}\right)^{\mathrm{T}} \boldsymbol{S}_{\boldsymbol{\epsilon}}^{-1} \frac{\partial \boldsymbol{f}(\boldsymbol{x})}{\partial \boldsymbol{x}}\ +\ \boldsymbol{h}(\boldsymbol{x})^{\mathrm{T}} \boldsymbol{S}_{\boldsymbol{h}}^{-1} \frac{\partial \boldsymbol{h}(\boldsymbol{x})}{\partial \boldsymbol{x}}. \tag{A.53}$$

With the goal of scaling this forward model so that the numerical optimization is well-conditioned, we choose a preconditioner which strikes a compromise between the Levenberg-Marquardt preconditioning as described by Moré [95], and the pre-whitening type pre-conditioning as described by Rodgers [26]. The effect is that steps that are small in euclidean 2-norm will have reasonable prior probability and will result in measurement perturbations that are comparable to measurement error. The prior mean state $\boldsymbol{x}_{\text{prior}}$ is used as the initial guess, and a preconditioner is derived from the posterior covariance evaluated at the prior mean state:

$$\boldsymbol{S}_{\text{post}}^{-1}(\boldsymbol{x}_{\text{prior}}) = \frac{\partial \boldsymbol{f}(\boldsymbol{x}_{\text{prior}})}{\partial \boldsymbol{x}}^{\mathrm{T}} \boldsymbol{S}_{\boldsymbol{\epsilon}}^{-1} \frac{\partial \boldsymbol{f}(\boldsymbol{x}_{\text{prior}})}{\partial \boldsymbol{x}}\ +\ \frac{\partial \boldsymbol{h}(\boldsymbol{x}_{\text{prior}})}{\partial \boldsymbol{x}}^{\mathrm{T}} \boldsymbol{S}_{\boldsymbol{h}}^{-1} \frac{\partial \boldsymbol{h}(\boldsymbol{x}_{\text{prior}})}{\partial \boldsymbol{x}}. \tag{A.54}$$

Since a covariance matrix is always symmetric and positive semi-definite, it admits an

eigen-decomposition with non-negative eigen-values and an orthonormal set of eigen-vectors. These are used to define the following square-root matrix:

$$\boldsymbol{B} = \left(\boldsymbol{S}_{\text{post}}^{-1}(\boldsymbol{x}_{\text{prior}})\right)^{1/2} . \tag{A.55}$$

The forward model is rescaled by replacing $\boldsymbol{x}$ with a new optimization parameter $\mathring{\boldsymbol{x}}$ defined by the following relations:

$$\mathring{\boldsymbol{x}} = c\,\boldsymbol{B}\;\left(\boldsymbol{x} - \boldsymbol{x}_{\text{prior}}\right) , \tag{A.56}$$

$$\boldsymbol{x} = \boldsymbol{x}_{\text{prior}} + \frac{1}{c}\boldsymbol{B}^{-1}\mathring{\boldsymbol{x}} , \tag{A.57}$$

$$c = \frac{1}{N}\sum_{n=0}^{N-1}\sum_{m=0}^{M-1}\left\|\left(\boldsymbol{S}_{\boldsymbol{\epsilon}}^{-1/2}\frac{\partial \boldsymbol{f}(\boldsymbol{x}_{\text{prior}})}{\partial \boldsymbol{x}}\boldsymbol{B}^{-1}\right)_{n}^{m}\right\| . \tag{A.58}$$

The scaled cost functional for passing to the numerical optimization routine is defined as follows:

$$\mathring{\Phi}\left(\mathring{\boldsymbol{x}}\right) = \Phi\left(\boldsymbol{x}_{\text{prior}} + \frac{1}{c}\boldsymbol{B}^{-1}\mathring{\boldsymbol{x}}\right) , \tag{A.59}$$

$$\frac{\partial\mathring{\Phi}(\mathring{\boldsymbol{x}})}{\partial\mathring{\boldsymbol{x}}} = \frac{1}{c}\frac{\partial\Phi(\boldsymbol{x})}{\partial\boldsymbol{x}}\boldsymbol{B}^{-1} . \tag{A.60}$$

Although prior constraints are already built in to this functional, some additional constraints help the numerical optimization routine to avoid non-physical steps and stay within the bounds of our refractive index look-up tables. Inequality constraints ensure positivity of the crossection density and basis function coefficients, and they also prevent refractive indices from wandering outside of the look-up table. For each mode of particles

$0 \leq j < J$ the following are constrained to hold during the optimization:

$$0 \leq c_{0j}(\mathring{\boldsymbol{x}}) = \varsigma^j\left(\boldsymbol{x}(\mathring{\boldsymbol{x}})\right) \qquad \text{with} \qquad \frac{\partial c_{0j}}{\partial \mathring{\boldsymbol{x}}} = \frac{1}{c}\frac{\partial \varsigma^j}{\partial \boldsymbol{x}}\boldsymbol{B}^{-1}\,, \tag{A.61}$$

$$0 \leq \boldsymbol{c}_{1j}(\mathring{\boldsymbol{x}}) = \boldsymbol{p}_j\left(\boldsymbol{x}(\mathring{\boldsymbol{x}})\right) \qquad \text{with} \qquad \frac{\partial \boldsymbol{c}_{1j}}{\partial \mathring{\boldsymbol{x}}} = \frac{1}{c}\frac{\partial \boldsymbol{p}_j}{\partial \boldsymbol{x}}\boldsymbol{B}^{-1}\,, \tag{A.62}$$

$$0 \leq \boldsymbol{c}_{2j}(\mathring{\boldsymbol{x}}) = \boldsymbol{q}_j\left(\boldsymbol{x}(\mathring{\boldsymbol{x}})\right) - \boldsymbol{q}_{\min} \qquad \text{with} \qquad \frac{\partial \boldsymbol{c}_{2j}}{\partial \mathring{\boldsymbol{x}}} = \frac{1}{c}\frac{\partial \boldsymbol{q}_j}{\partial \boldsymbol{x}}\boldsymbol{B}^{-1}\,, \tag{A.63}$$

$$0 \leq \boldsymbol{c}_{3j}(\mathring{\boldsymbol{x}}) = \boldsymbol{q}_{\max} - \boldsymbol{q}_j\left(\boldsymbol{x}(\mathring{\boldsymbol{x}})\right) \qquad \text{with} \qquad \frac{\partial \boldsymbol{c}_{3j}}{\partial \mathring{\boldsymbol{x}}} = -\frac{1}{c}\frac{\partial \boldsymbol{q}_j}{\partial \boldsymbol{x}}\boldsymbol{B}^{-1}\,. \tag{A.64}$$

Specifying the derivatives of these constraints enables faster convergence, and so these quantities are provided also. Upon convergence, the optimization returns $\mathring{\boldsymbol{x}}_{\text{post}}$ which is used to compute the estimate $\boldsymbol{x}_{\text{post}}$ for particle microphysical properties:

$$\boldsymbol{x}_{\text{post}} = \boldsymbol{x}_{\text{prior}} + \frac{1}{c}\boldsymbol{B}^{-1}\mathring{\boldsymbol{x}}_{\text{post}}\,. \tag{A.65}$$

The quantified sources of uncertainty result in a posterior covariance matrix defined via its inverse as follows:

$$\boldsymbol{S}^{-1}_{\text{post}}(\boldsymbol{x}_{\text{post}}) = \frac{\partial \boldsymbol{f}(\boldsymbol{x}_{\text{post}})}{\partial \boldsymbol{x}}^{\mathrm{T}} \boldsymbol{S}^{-1}_{\boldsymbol{\epsilon}} \frac{\partial \boldsymbol{f}(\boldsymbol{x}_{\text{post}})}{\partial \boldsymbol{x}} \;+\; \frac{\partial \boldsymbol{h}(\boldsymbol{x}_{\text{post}})}{\partial \boldsymbol{x}}^{\mathrm{T}} \boldsymbol{S}^{-1}_{\boldsymbol{h}} \frac{\partial \boldsymbol{h}(\boldsymbol{x}_{\text{post}})}{\partial \boldsymbol{x}}\,. \tag{A.66}$$

The arrays $\boldsymbol{S}_{\text{post}}(\boldsymbol{x}_{\text{prior}})$ and $\boldsymbol{S}_{\text{post}}(\boldsymbol{x}_{\text{post}})$ are used to characterize error, specifically in calculations of the standard deviation of retrieval parameters and the principle components of uncertainty, and also in computing the information content of each measurement set and the number of degrees of freedom resolved by measurements vs. that resolved by the prior. They are also used to estimate the uncertainty in derived microphysical parameters such as the total number concentration of particles and the number concentration of active CCN (taken as particles with radius above a certain cutoff), and the effective radius and effective variance of the size distribution.

A.5 Uncertainty analysis and retrievals

Some microphysical properties are retrieved indirectly, including the CCN concentration, volume concentration, and the effective radius and effective variance, which characterize the size distribution. These derived parameters are written as functions of the microphysical parameters, $\boldsymbol{x}$, in the form of a vector valued function, $\boldsymbol{z}(\boldsymbol{x})$. The covariance matrix for the vector of derived parameters can be computed to first order using quadratic propagation as in [26]:

$$\boldsymbol{S}_{\boldsymbol{z}}(\boldsymbol{x}) = \frac{\partial \boldsymbol{z}(\boldsymbol{x})}{\partial \boldsymbol{x}} \, \boldsymbol{S}_{\boldsymbol{x}}(\boldsymbol{x}) \, \frac{\partial \boldsymbol{z}(\boldsymbol{x})}{\partial \boldsymbol{x}}^{T} . \tag{A.67}$$

Estimating the concentration of CCN requires assumptions about the activity of particles in the population. For the purposes of this study, CCN activity is assumed to be a function of size, and only particles with radius larger than a fixed cutoff are considered active CCN. The cutoffs used are as follows:

$$r = 31\text{nm}, \qquad r = 37\text{nm}, \quad \text{and} \qquad r = 43\text{nm}. \tag{A.68}$$

They are computed from the measured cutoff diameters of four fine mode atmospheric aerosols, taken at .4% supersaturation [22], as the sample mean plus-or-minus two standard deviations.

The goal in linear stability analysis is to draw useful information from the parameter uncertainty covariance matricies: $\boldsymbol{S}_{\text{prior}}$, $\boldsymbol{S}_{\text{post}}$, $\boldsymbol{S}_{\boldsymbol{z},\text{prior}}$, and $\boldsymbol{S}_{\boldsymbol{z},\text{post}}$. Similar techniques are applied to other observation systems for particle characterization [8, 50, 51, 53, 97], and a general description of these methods can be found in the following books [26, 60].

Rules for computing the plotted and tabulated results from prior, posterior, and derived covariance matricies are enumerated here, as a reference for interpreting figures.

For reference in the interpretation of the results of Chapter 3, the following itemization describes calculations of the plotted and tabulated values, such as the relative uncertainty in concentration, the error patterns for each linear stability analysis, the degrees of freedom resolved by measurements and prior, and the information content:

- The standard deviations for marginal distributions of individual parameters are visualized as error bars. These are computed as square roots of diagonal covariance matrix elements. Relative uncertainty in a scale parameter is computed as 100 times the ratio of a parameter's marginal standard deviation to parameter's value ($100 \times \frac{\sigma_z}{z}$).

- Error patterns are eigen-vectors of the posterior covariance matrix scaled by the square root of the eigen-values. For a given $\boldsymbol{S}_{\text{post}}$, the error patterns $\boldsymbol{v}_n$ have the property $\boldsymbol{v}_n^T \, \boldsymbol{S}_{\text{post}}^{-1} \, \boldsymbol{v}_{n'} = \delta_{nn'}$. This guarantees that posterior distribution about the mean state can be written as a linear combination of error patterns with independent standard normal coefficients. That is, the sum over error patterns with random, independent identically distributed coefficients $X_n \sim \text{Normal}(0, 1)$ is a sample of the posterior distribution about the mean,

$$\boldsymbol{x}|_{\boldsymbol{y}} - \boldsymbol{x}_{\text{prior}} = \sum_n X_n \boldsymbol{v}_n. \tag{A.69}$$

  These error patterns $\{\boldsymbol{v}_n\}$ can also be thought of as the semi-axes of the N dimentional ellipse with length measuring one standard deviation away from the mean.

- The number of *degrees of freedom* constrained by signal $\mathrm{d_{signal}}$ and prior $\mathrm{d_{prior}}$ are computed to show how many of the microphysical parameters are resolved beyond prior constraints due to measurements. These quantities are computed with the following formulae:

$$\mathrm{d_{signal}} = \mathrm{trace}\left(\left[\frac{\partial \boldsymbol{f}}{\partial \boldsymbol{x}}^T \boldsymbol{S}_{\boldsymbol{\epsilon}}^{-1} \frac{\partial \boldsymbol{f}}{\partial \boldsymbol{x}} + \frac{\partial \boldsymbol{h}}{\partial \boldsymbol{x}}^T \boldsymbol{S}_{\boldsymbol{h}}^{-1} \frac{\partial \boldsymbol{h}}{\partial \boldsymbol{x}}\right]^{-1} \frac{\partial \boldsymbol{f}}{\partial \boldsymbol{x}}^T \boldsymbol{S}_{\boldsymbol{\epsilon}}^{-1} \frac{\partial \boldsymbol{f}}{\partial \boldsymbol{x}}\right), \tag{A.70}$$

$$\mathrm{d_{prior}} = \mathrm{trace}\left(\left[\frac{\partial \boldsymbol{f}}{\partial \boldsymbol{x}}^T \boldsymbol{S}_{\boldsymbol{\epsilon}}^{-1} \frac{\partial \boldsymbol{f}}{\partial \boldsymbol{x}} + \frac{\partial \boldsymbol{h}}{\partial \boldsymbol{x}}^T \boldsymbol{S}_{\boldsymbol{h}}^{-1} \frac{\partial \boldsymbol{h}}{\partial \boldsymbol{x}}\right]^{-1} \frac{\partial \boldsymbol{h}}{\partial \boldsymbol{x}}^T \boldsymbol{S}_{\boldsymbol{h}}^{-1} \frac{\partial \boldsymbol{h}}{\partial \boldsymbol{x}}\right). \tag{A.71}$$

  By summing the two together one may varify that $\mathrm{d_{signal}} + \mathrm{d_{prior}} = N$, where N is the number of microphysical parameters for the given spherical particle of interest.

- Shannon information content is computed for the microphysical parameter space as a whole, and separately for subspaces which include loading parameters, size distribution parameters, real refractive indices, and imaginary refractive indices. Given two covariance matrices $\boldsymbol{S}_0$ and $\boldsymbol{S}_1$ the extra information in $\boldsymbol{S}_1$ is defined in by the following expression:

$$H = \log_2\left(\frac{\det(\boldsymbol{S}_0)}{\det(\boldsymbol{S}_1)}\right). \tag{A.72}$$

  Each unit of information coresponds to a reduction in the volume of the parallelpiped defined by the column vectors of $\boldsymbol{S}_1$ relative to that defined by the column vectors of $\boldsymbol{S}_0$. Smaller volumes imply more finely resolved parameters. Shannon information content is specific to the parameter subspace for which it is computed.

Following the results of each linear stability analysis, we used a synthetic retrieval study to demonstrate the procedure for numerical inversions. Also, this allowed us to check that the spread of retrievals due to random noise in the data is comparable to the uncertainty

predicted by the linear stability analysis. The synthetic retrievals are performed according to the following proceedure:

1. From the prior distribution, we draw a random realization and take this to be the true microphysical state $\boldsymbol{x}$:

$$\boldsymbol{x} \sim \text{Normal}\left(\boldsymbol{x}_{\text{prior}}, \boldsymbol{S}_{\text{prior}}(\boldsymbol{x}_{\text{prior}})\right). \tag{A.73}$$

2. Perfect measurements are computed using the foward model:

$$\boldsymbol{y} = \boldsymbol{f}(\boldsymbol{x}). \tag{A.74}$$

3. Several realizations of measurement error are sampled from the measurement error distribution, to generate synthetic data $\hat{\boldsymbol{y}}$:

$$\hat{\boldsymbol{y}} \sim \text{Normal}(\boldsymbol{y}, \boldsymbol{S}_{\boldsymbol{\epsilon}}(\boldsymbol{y})). \tag{A.75}$$

4. Each of these noisy data vectors is used to select a retrieval $\boldsymbol{x}_{\text{post}}$, which agrees best with the data and prior:

$$\boldsymbol{x}_{\text{post}} = \underset{\boldsymbol{x}}{\text{argmin}}\left(\Phi_{\text{data}}(\boldsymbol{x}) + \Phi_{\text{prior}}(\boldsymbol{x})\right). \tag{A.76}$$

5. A prediction for true measurements is made by evaluating the forward model at the retrieved microphysical state,

$$\boldsymbol{y}_{\text{post}} = \boldsymbol{f}(\boldsymbol{x}_{\text{post}}) \tag{A.77}$$

6. Errors are defined for the microphysical state and for the measurement prediction as $\Delta\boldsymbol{x}_{\text{post}}$ and $\Delta\boldsymbol{y}_{\text{post}}$:

$$\Delta\boldsymbol{x}_{\text{post}} = \boldsymbol{x}_{\text{post}} - \boldsymbol{x}, \tag{A.78}$$

$$\Delta\boldsymbol{y}_{\text{post}} = \boldsymbol{y}_{\text{post}} - \boldsymbol{y}. \tag{A.79}$$

The retrievals of loading, size distribution, and spectrally dependent complex refractive index are computed for visualization along with those of the true microphysical particle population. The error in microphysical parameters is computed to enable comparison with error patters assosiated with the linear stability analysis. Measurement prediction error is computed but not shown, and in each case falls within the levels of instrument noise.

Appendix B

Technical results for adjoint methods

This appendix contains several important theorems which were used throughout Chapter 5. Section B.1 shows the equivalence of integral and integro-differential forms of 3D VRTE, and Section B.2 shows the elementary adjoint properties for the streaming operators and the operators of scattering and reflection.

B.1 Equivalence of Integral and differential equations of 3D VRT

Integral and differential forms of 3D VRT were used interchangeably in the main text of the paper. This appendix justifies such use by showing that both the forward and adjoint system of integral equations provide a solution to the corresponding differential 3D VRTE. The first theorem states and proves properties from Eqs. (4.97) - (4.100). Then these properties will be used in the two theorems that follow: one for forward equivalence and another for adjoint equivalence.

Theorem B.1 (Streaming properties)**.** *The advective derivative acts on streaming operator output functions according to the following rules:*

$$(\boldsymbol{v}\cdot\nabla+\sigma)[\,\mathcal{T}_{-0}[\boldsymbol{g}]\,]=0, \tag{B.1}$$

$$(\boldsymbol{v}\cdot\nabla+\sigma)[\,\mathcal{T}_{00}[\boldsymbol{f}]\,]=\boldsymbol{f}, \tag{B.2}$$

$$(-\boldsymbol{v}\cdot\nabla+\sigma)\big[\,\mathcal{T}^{*}_{0+}[\boldsymbol{q}]\,\big]=0, \tag{B.3}$$

$$(-\boldsymbol{v}\cdot\nabla+\sigma)[\,\mathcal{T}^{*}_{00}[\boldsymbol{p}]\,]=\boldsymbol{p}. \tag{B.4}$$

Proof. We begin with Eq. (B.1):

$$\begin{aligned}\boldsymbol{v}\cdot\nabla\mathcal{T}_{-0}[\,\boldsymbol{g}\,](\boldsymbol{x},\boldsymbol{v}) &= \frac{\partial}{\partial t}\exp\left(-\int_{t_-}^{t}\mathrm{d}t''\sigma(\boldsymbol{x}^{\perp}+t''\boldsymbol{v})\right)\boldsymbol{g}(\boldsymbol{x}^{\perp}+t_-\boldsymbol{v},\boldsymbol{v}),\\ &= -\sigma(\boldsymbol{x})\;\mathcal{T}_{-0}[\,\boldsymbol{g}\,](\boldsymbol{x},\boldsymbol{v}).\end{aligned}$$

Next we show Eq. (B.2) using an extension of the Leibniz rule to non-constant limits of integration [98]:

$$\begin{aligned}\boldsymbol{v}\cdot\nabla\mathcal{T}_{00}[\,\boldsymbol{f}\,](\boldsymbol{x},\boldsymbol{v}) &= \frac{\partial}{\partial t}\int_{t_-}^{t}\mathrm{d}t'\;\exp\left(-\int_{t'}^{t}\mathrm{d}t''\sigma(\boldsymbol{x}^{\perp}+t''\boldsymbol{v})\right)\boldsymbol{f}(\boldsymbol{x}^{\perp}+t'\boldsymbol{v},\boldsymbol{v}),\\ &= \exp(0)\boldsymbol{f}(\boldsymbol{x}^{\perp}+t\boldsymbol{v},\boldsymbol{v})\\ &\qquad -\sigma(\boldsymbol{x}^{\perp}+t\boldsymbol{v})\int_{t_-}^{t}\mathrm{d}t'\exp\left(-\int_{t'}^{t}\mathrm{d}t''\sigma(\boldsymbol{x}^{\perp}+t''\boldsymbol{v})\right)\boldsymbol{f}(\boldsymbol{x}^{\perp}+t'\boldsymbol{v},\boldsymbol{v}),\\ &= \boldsymbol{f}(\boldsymbol{x},\boldsymbol{v})-\sigma(\boldsymbol{x})\;\mathcal{T}_{00}[\,\boldsymbol{f}\,](\boldsymbol{x},\boldsymbol{v}).\end{aligned}$$

For Eq. (B.3) we have the following:

$$\begin{aligned}-\boldsymbol{v}\cdot\nabla\mathcal{T}^*_{0+}[\,\boldsymbol{q}\,](\boldsymbol{x},\boldsymbol{v}) &= -\frac{\partial}{\partial t}\exp\left(-\int_t^{t_+}\mathrm{d}t''\sigma(\boldsymbol{x}^\perp+t''\boldsymbol{v})\right)\boldsymbol{q}(\boldsymbol{x}^\perp+t_+\boldsymbol{v},\boldsymbol{v}),\\ &= -\sigma(\boldsymbol{x})\;\mathcal{T}^*_{0+}[\,\boldsymbol{q}\,](\boldsymbol{x},\boldsymbol{v}).\end{aligned}$$

Lastly, we show Eq. (B.4):

$$\begin{aligned}-\boldsymbol{v}\cdot\nabla\mathcal{T}^*_{00}[\,\boldsymbol{p}\,](\boldsymbol{x},\boldsymbol{v}) &= -\frac{\partial}{\partial t}\int_t^{t_+}\mathrm{d}t'\;\exp\left(-\int_t^{t'}\mathrm{d}t''\sigma(\boldsymbol{x}^\perp+t''\boldsymbol{v})\right)\boldsymbol{p}(\boldsymbol{x}^\perp+t'\boldsymbol{v},\boldsymbol{v}),\\ &= \exp(0)\boldsymbol{p}(\boldsymbol{x}^\perp+t\boldsymbol{v},\boldsymbol{v})\\ &\qquad -\sigma(\boldsymbol{x}^\perp+t\boldsymbol{v})\int_t^{t_+}\mathrm{d}t'\exp\left(-\int_t^{t'}\mathrm{d}t''\sigma(\boldsymbol{x}^\perp+t''\boldsymbol{v})\right)\boldsymbol{p}(\boldsymbol{x}^\perp+t'\boldsymbol{v},\boldsymbol{v}),\\ &= \boldsymbol{p}(\boldsymbol{x},\boldsymbol{v})-\sigma(\boldsymbol{x})\;\mathcal{T}^*_{00}[\,\boldsymbol{p}\,](\boldsymbol{x},\boldsymbol{v}).\end{aligned}$$

The four properties are thus verified. □

Theorem B.2 (Forward 3D VRTE equivalence)**.** *The Stokes vector* $\boldsymbol{u}$ *given by the integral formulation of 3D VRT in Eqs. (4.104) - (4.107) solves the integro-differential 3D VRTE from Definition 4.2.*

Proof. First, we note that the functions $\boldsymbol{u}|_{\Gamma_+}$ and $\boldsymbol{u}|_{\Gamma_-}$ agree with the limits of $\boldsymbol{u}|_{D\times\mathbb{S}^2}$ along lines approaching the boundary. The boundary conditions are verified by substituting Eqs. (4.105) and (4.106) into the left hand side of Eq. (4.17) and applying Eq.

(4.107) to show equality with the right-hand side:

$$\begin{aligned}\boldsymbol{u}|_{\Gamma_-} - \mathcal{R}\big[\,\boldsymbol{u}|_{\Gamma_+}\,\big] &= \boldsymbol{g} - \mathcal{R}[\,\mathcal{T}_{0+}[\boldsymbol{f}] + \mathcal{T}_{-+}[\boldsymbol{g}]\,],\\ &= \boldsymbol{g} - \mathcal{R}\mathcal{T}_{0+}[\boldsymbol{f}] + \mathcal{R}\mathcal{T}_{-+}[\boldsymbol{g}],\\ &= \boldsymbol{g}_{\odot}.\end{aligned}$$

The solution on internal points is verified by substituting Eq. (4.104) into the left hand side of Eq. (4.16) and applying Theorem B.1 and Eq. (4.107) to show equality with the right-hand side:

$$\begin{aligned}\boldsymbol{v}\cdot\nabla\boldsymbol{u} + \sigma\boldsymbol{u} - \mathcal{Z}[\,\boldsymbol{u}\,] &= (\boldsymbol{v}\cdot\nabla+\sigma)[\,\mathcal{T}_{00}[\boldsymbol{f}] + \mathcal{T}_{-0}[\boldsymbol{g}]\,] - \mathcal{Z}[\,\mathcal{T}_{00}[\boldsymbol{f}] + \mathcal{T}_{-0}[\boldsymbol{g}]\,],\\ &= \boldsymbol{f} - \mathcal{Z}\mathcal{T}_{00}[\boldsymbol{f}] + \mathcal{Z}\mathcal{T}_{-0}[\boldsymbol{g}],\\ &= \boldsymbol{f}_{\odot}.\end{aligned}$$

Thus, the Stokes vector $\boldsymbol{u}$ constructed from solutions $\boldsymbol{f}$ and $\boldsymbol{g}$ of the integral equations solves the differential 3D VRTE. □

Theorem B.3 (Adjoint 3D VRTE equivalence)**.** *The adjoint Stokes vector, $\boldsymbol{w}$, given by the integral formulation of the adjoint 3D VRTE in Eqs. (4.113) - (4.116) solves the integro-differential form of the adjoint 3D VRTE from Definition 4.3.*

Proof. First, we note that functions $\boldsymbol{w}|_{\Gamma_-}$ and $\boldsymbol{w}|_{\Gamma_+}$ agree with the limits of $\boldsymbol{w}|_{D\times\mathbb{S}^2}$ along lines approaching the boundary. The boundary conditions are verified by substituting Eqs. (4.114) and (4.115) into the left hand side of Eq. (4.27) and applying Eq. (4.116)

to show equality with the expected right-hand side:

$$\begin{aligned}\boldsymbol{w}|_{\Gamma_+} - \mathcal{R}^*\big[\,\boldsymbol{w}|_{\Gamma_-}\,\big] &= \boldsymbol{q} - \mathcal{R}^*\big[\,\mathcal{T}^*_{-0}[\boldsymbol{p}] + \mathcal{T}^*_{-+}[\boldsymbol{q}]\,\big],\\ &= \boldsymbol{q} - \mathcal{R}^*\mathcal{T}^*_{-0}[\boldsymbol{p}] + \mathcal{R}^*\mathcal{T}^*_{-+}[\boldsymbol{q}],\\ &= \boldsymbol{q}_\odot.\end{aligned}$$

The solution on internal points is verified by substituting Eq. (4.113) into the left hand side of Eq. (4.26) and applying Theorem B.1 and Eq. (4.116) to show equality with the right-hand side:

$$\begin{aligned}-\boldsymbol{v}\cdot\nabla\boldsymbol{w} + \sigma\boldsymbol{w} - \mathcal{Z}^*[\,\boldsymbol{w}\,] &= (-\boldsymbol{v}\cdot\nabla+\sigma)\big[\,\mathcal{T}^*_{00}[\boldsymbol{p}] + \mathcal{T}^*_{0+}[\boldsymbol{q}]\,\big] - \mathcal{Z}^*\big[\,\mathcal{T}^*_{00}[\boldsymbol{p}] + \mathcal{T}^*_{0+}[\boldsymbol{q}]\,\big],\\ &= \boldsymbol{p} - \mathcal{Z}^*\mathcal{T}^*_{00}[\boldsymbol{p}] + \mathcal{Z}^*\mathcal{T}^*_{0+}[\boldsymbol{q}],\\ &= \boldsymbol{p}_\odot.\end{aligned}$$

Thus, the adjoint Stokes vector $\boldsymbol{w}$ constructed from the solutions $\boldsymbol{p}$ and $\boldsymbol{q}$ of the integral equations solves the differential 3D VRTE. □

B.2 Elementary adjoint property results

Proof of the adjoint properties for streaming operators will require us to equate certain multi-variable integrals, and this is facilitated by changing co-ordinates to integrate along chords. After summarizing these coordinate transformations, we will prove the four elementary adjoint properties for streaming operators stated in Eqs. (4.69) - (4.72). Following this, we will show the adjoint properties of scattering and reflection operators.

The natural basis to use for streaming integration proofs depends on the direction $\boldsymbol{v} \in \mathbb{S}^2$, and without loss of generality we take the standard basis for $\boldsymbol{v}$ in terms of angles ϑ and φ. This gives the following orthonormal basis for $\mathbb{R}^3$:

$$\begin{aligned}
\boldsymbol{v} &= \begin{bmatrix} \sin\vartheta\cos\varphi & \sin\vartheta\sin\varphi & \cos\vartheta \end{bmatrix}^T, \\
\boldsymbol{\vartheta} &= \begin{bmatrix} \cos\vartheta\cos\varphi & \cos\vartheta\sin\varphi & -\sin\vartheta \end{bmatrix}^T, \\
\boldsymbol{\varphi} &= \begin{bmatrix} -\sin\varphi & \cos\varphi & 0 \end{bmatrix}^T.
\end{aligned}$$

The coordinate transformation for the internal set $D \times \mathbb{S}^2$ is given by the following rules:

$$\begin{aligned}
t &= \boldsymbol{v} \cdot \boldsymbol{x}, \\
y^1 &= \boldsymbol{\vartheta} \cdot \boldsymbol{x}, \\
y^2 &= \boldsymbol{\varphi} \cdot \boldsymbol{x}, \\
\vartheta &= \vartheta, \\
\varphi &= \varphi.
\end{aligned}$$

The rules change coordinates so that the chord parameter, t, controls the projection of $\boldsymbol{x}$ along $\boldsymbol{v}$, while variables y^1 and y^2 control location in the 2-dimensional plane orthogonal to $\boldsymbol{v}$. We note that the perpendicular component used in the body of the paper, $\boldsymbol{x}^\perp$, is related to y^1 and y^2:

$$\boldsymbol{x}^\perp = \boldsymbol{\vartheta} y^1 + \boldsymbol{\varphi} y^2.$$

The associated surface element $\mathrm{d}y^1\mathrm{d}y^2$ is written more compactly as $\mathrm{d}S_{\boldsymbol{x}^\perp}$. For evaluating integrals over the internal set, there is no change in weight associated with the chord

transformation and,

$$\mathrm{d}S_{\boldsymbol{v}}\mathrm{d}S_{\boldsymbol{x}^\perp}\mathrm{d}t = \mathrm{d}S_{\boldsymbol{v}}\mathrm{d}x^1\mathrm{d}x^2\mathrm{d}x^3. \tag{B.5}$$

For position direction pairs on the outgoing and incoming sets, the change of weight is exactly the cosine of the angle of incidence. For coordinate transformation from the perpendicular component of a chord, $\boldsymbol{x}^\perp$, to the outgoing position, $\boldsymbol{x}_+$, we write,

$$\mathrm{d}S_{\boldsymbol{v}}\mathrm{d}S_{\boldsymbol{x}^\perp} = \mathrm{d}S_{\boldsymbol{x}_+}\mathrm{d}S_{\boldsymbol{v}_+}|\boldsymbol{v}_+ \cdot \nabla h(\boldsymbol{x}_+)|, \tag{B.6}$$

and for coordinate transformations to the incoming position, $\boldsymbol{x}_-$, we write,

$$\mathrm{d}S_{\boldsymbol{v}}\mathrm{d}S_{\boldsymbol{x}^\perp} = \mathrm{d}S_{\boldsymbol{x}_-}\mathrm{d}S_{\boldsymbol{v}_-}|\boldsymbol{v}_- \cdot \nabla h(\boldsymbol{x}_-)|. \tag{B.7}$$

These transformations are helpful in proving the four elementary adjoint properties for streaming operators.

Theorem B.4 (Internal streaming adjoint property)**.** *The internal streaming operators $\mathcal{T}_{00}$ and $\mathcal{T}_{00}^*$, defined by Eqs. (4.89) and (4.93), satisfy the adjoint property:*

$$\Big\langle \boldsymbol{p},\ \mathcal{T}_{00}[\,\boldsymbol{f}\,] \Big\rangle_{D\times\mathbb{S}^2} = \Big\langle \mathcal{T}_{00}^*[\,\boldsymbol{p}\,],\ \boldsymbol{f}\ \Big\rangle_{D\times\mathbb{S}^2} \tag{B.8}$$

Proof. Beginning with the left hand side of Eq. (B.8), the equality is demonstrated in the following steps:

$$
\begin{aligned}
&\int_D \mathrm{d}V_{\boldsymbol{x}} \int_{\mathbb{S}^2} \mathrm{d}S_{\boldsymbol{v}}\ \boldsymbol{p}(\boldsymbol{x},\boldsymbol{v})^T \cdot \mathcal{T}_{00}[\,\boldsymbol{f}\,](\boldsymbol{x},\boldsymbol{v}) = \\
&\quad = \int_{\mathbb{S}^2} \mathrm{d}S_{\boldsymbol{v}} \int_{\boldsymbol{x}^\perp(D)} \mathrm{d}S_{\boldsymbol{x}^\perp} \sum_{(t_-,t_+)} \int_{t_-}^{t_+} \mathrm{d}t \int_{t_-}^{t} \mathrm{d}t' \Big[\\
&\qquad\qquad \boldsymbol{p}(\boldsymbol{x}^\perp + t\boldsymbol{v},\boldsymbol{v})^T \cdot \exp\left(- \int_{t'}^{t} \sigma(\boldsymbol{x}^\perp + t''\boldsymbol{v})\mathrm{d}t'' \right) \boldsymbol{f}(\boldsymbol{x}^\perp + t'\boldsymbol{v},\boldsymbol{v}) \Big], \\
&\quad = \int_{\mathbb{S}^2} \mathrm{d}S_{\boldsymbol{v}} \int_{\boldsymbol{x}^\perp(D)} \mathrm{d}S_{\boldsymbol{x}^\perp} \sum_{(t_-,t_+)} \int_{t_-}^{t_+} \mathrm{d}t' \int_{t'}^{t_+} \mathrm{d}t \Big[\\
&\qquad\qquad \exp\left(- \int_{t'}^{t} \sigma(\boldsymbol{x}^\perp + t''\boldsymbol{v})\mathrm{d}t'' \right) \boldsymbol{p}(\boldsymbol{x}^\perp + t\boldsymbol{v},\boldsymbol{v})^T \cdot \boldsymbol{f}(\boldsymbol{x}^\perp + t'\boldsymbol{v},\boldsymbol{v}) \Big], \\
&\quad = \int_{\mathbb{S}^2} \mathrm{d}S_{\boldsymbol{v}} \int_{\boldsymbol{x}^\perp(D)} \mathrm{d}S_{\boldsymbol{x}^\perp} \sum_{(t_-,t_+)} \int_{t_-}^{t_+} \mathrm{d}t' \mathcal{T}^*_{00}[\,\boldsymbol{p}\,](\boldsymbol{x}^\perp + t'\boldsymbol{v},\boldsymbol{v})^T \cdot \boldsymbol{f}(\boldsymbol{x}^\perp + t'\boldsymbol{v},\boldsymbol{v}), \\
&\quad = \int_D \mathrm{d}V_{\boldsymbol{x}} \int_{\mathbb{S}^2} \mathrm{d}S_{\boldsymbol{v}}\ \mathcal{T}^*_{00}[\,\boldsymbol{p}\,](\boldsymbol{x},\boldsymbol{v})^T \cdot \boldsymbol{f}(\boldsymbol{x},\boldsymbol{v}).
\end{aligned}
$$

This is the right-hand side of Eq. (B.8). We note two key steps. First, we rewrote the integral over space as an integral over chords:

$$
\int_D \mathrm{d}V_x \approx \int_{\boldsymbol{x}^\perp(D)} \mathrm{d}S_{\boldsymbol{x}^\perp} \sum_{(t_-,t_+)} \int_{t_-}^{t_+} \mathrm{d}t.
$$

Second, we exchanged the order of integration of dt and $\mathrm{d}t'$:

$$
\int_{t_-}^{t_+} \mathrm{d}t \int_{t_-}^{t} \mathrm{d}t' \approx \int_{t_-}^{t_+} \mathrm{d}t' \int_{t'}^{t_+} \mathrm{d}t.
$$

Then, changing back to the original coordinates completed the proof. □

Theorem B.5 (Internal source to outgoing Stokes vector streaming adjoint property)**.** *The streaming operator $\mathcal{T}_{0+}$ defined by Eq. (4.90) has adjoint $\mathcal{T}_{0+}^*$ defined by Eq. (4.94):*

$$\Big\langle \boldsymbol{q}, \mathcal{T}_{0+}[\,\boldsymbol{f}\,] \Big\rangle_{\Gamma_+} = \Big\langle \mathcal{T}_{0+}^*[\,\boldsymbol{q}\,], \boldsymbol{f} \Big\rangle_{D\times\mathbb{S}^2}. \tag{B.9}$$

Proof. Beginning with the definition of the left hand side of Eq. (B.9) we proceed through the following steps:

$$\begin{aligned}
&\int_{\partial D} \mathrm{d}S_{\boldsymbol{x}_+} \int_{\boldsymbol{v}_+\cdot\nabla h>0} \mathrm{d}S_{\boldsymbol{v}_+} \,|\boldsymbol{v}_+\nabla h(\boldsymbol{x}_+)|\boldsymbol{q}(\boldsymbol{x}_+,\boldsymbol{v}_+)^T\cdot\mathcal{T}_{0+}[\,\boldsymbol{f}\,](\boldsymbol{x}_+,\boldsymbol{v}_+) = \\
&\qquad = \int_{\mathbb{S}^2} \mathrm{d}S_{\boldsymbol{v}} \int_{\boldsymbol{x}^\perp(D)} \mathrm{d}S_{\boldsymbol{x}^\perp} \sum_{t_+} \Big[\\
&\qquad\qquad \boldsymbol{q}(\boldsymbol{x}^\perp + t_+\boldsymbol{v},\boldsymbol{v})^T \cdot \int_{t_-}^{t_+} \mathrm{d}t\, \exp\left(-\int_t^{t_+} \sigma(\boldsymbol{x}^\perp + t''\boldsymbol{v})\mathrm{d}t''\right) \boldsymbol{f}(\boldsymbol{x}^\perp + t\boldsymbol{v},\boldsymbol{v})\Big], \\
&\qquad = \int_{\mathbb{S}^2} \mathrm{d}S_{\boldsymbol{v}} \int_{\boldsymbol{x}^\perp(D)} \mathrm{d}S_{\boldsymbol{x}^\perp} \sum_{t_+} \Big[\\
&\qquad\qquad \int_{t_-}^{t_+} \mathrm{d}t\, \left(\exp\left(-\int_t^{t_+} \sigma(\boldsymbol{x}^\perp + t''\boldsymbol{v})\mathrm{d}t''\right) \boldsymbol{q}(\boldsymbol{x}^\perp + t_+\boldsymbol{v},\boldsymbol{v})\right)^T \cdot \boldsymbol{f}(\boldsymbol{x}^\perp + t\boldsymbol{v},\boldsymbol{v})\Big], \\
&\qquad = \int_D \mathrm{d}V_{\boldsymbol{x}} \int_{\mathbb{S}^2} \mathrm{d}S_{\boldsymbol{v}}\, \mathcal{T}_{0+}^*[\,\boldsymbol{q}\,](\boldsymbol{x},\boldsymbol{v})^T\cdot\boldsymbol{f}(\boldsymbol{x},\boldsymbol{v}).
\end{aligned}$$

These steps show the equality. The key was writing each outgoing position $\boldsymbol{x}_+$ as the endpoint $\boldsymbol{x}_+ = \boldsymbol{x}^\perp + t_+\boldsymbol{v}$ of a chord through the domain. Recognizing the definition of $\mathcal{T}_{0+}^*$ and changing to standard coordinates completes the proof. □

Theorem B.6 (Incoming to internal Stokes vector streaming adjoint property)**.** *The streaming operators $\mathcal{T}_{-0}$ and $\mathcal{T}^*_{-0}$ defined by Eqs. (4.91) and (4.95) are adjoint:*

$$\Big\langle \boldsymbol{p}, \mathcal{T}_{-0}[\,\boldsymbol{g}\,] \Big\rangle_{D\times\mathbb{S}^2} = \Big\langle \mathcal{T}^*_{-0}[\,\boldsymbol{p}\,], \boldsymbol{g} \Big\rangle_{\Gamma_-}. \tag{B.10}$$

Proof. We begin with the definition of the left hand side of Eq. (B.10) and show the equality with the following steps:

$$\begin{aligned}
&\int_D \mathrm{d}V_{\boldsymbol{x}} \int_{\mathbb{S}^2} \mathrm{d}S_{\boldsymbol{v}}\, \boldsymbol{p}(\boldsymbol{x},\boldsymbol{v})^T \cdot \mathcal{T}_{-0}[\,\boldsymbol{g}\,](\boldsymbol{x},\boldsymbol{v}) = \\
&\quad = \int_{\mathbb{S}^2} \mathrm{d}S_{\boldsymbol{v}} \int_{\boldsymbol{x}^\perp(D)} \mathrm{d}S_{\boldsymbol{x}^\perp} \sum_{t_-} \Big[\\
&\qquad \int_{t_-}^{t_+} \mathrm{d}t\; \boldsymbol{p}(\boldsymbol{x}^\perp + t\boldsymbol{v},\boldsymbol{v})^T \cdot \exp\left(-\int_{t_-}^{t} \sigma(\boldsymbol{x}^\perp + t''\boldsymbol{v})\mathrm{d}t'' \right) \boldsymbol{g}(\boldsymbol{x}^\perp + t_-\boldsymbol{v},\boldsymbol{v}) \Big], \\
&\quad = \int_{\mathbb{S}^2} \mathrm{d}S_{\boldsymbol{v}} \int_{\boldsymbol{x}^\perp(D)} \mathrm{d}S_{\boldsymbol{x}^\perp} \sum_{t_-} \Big[\\
&\qquad \left(\int_{t_-}^{t_+} \mathrm{d}t\; \exp\left(-\int_{t_-}^{t} \sigma(\boldsymbol{x}^\perp + t''\boldsymbol{v})\mathrm{d}t'' \right) \boldsymbol{p}(\boldsymbol{x}^\perp + t\boldsymbol{v},\boldsymbol{v}) \right)^T \cdot \boldsymbol{g}(\boldsymbol{x}^\perp + t_-\boldsymbol{v},\boldsymbol{v}) \Big], \\
&\quad = \int_{\partial D} \mathrm{d}S_{\boldsymbol{x}_-} \int_{\boldsymbol{v}_-\cdot\nabla h<0} \mathrm{d}S_{\boldsymbol{v}_-}\; |\boldsymbol{v}_-\cdot\nabla h(\boldsymbol{x}_-)|\; \mathcal{T}^*_{-0}[\,\boldsymbol{p}\,](\boldsymbol{x}_-,\boldsymbol{v}_-)^T \cdot \boldsymbol{g}(\boldsymbol{x}_-,\boldsymbol{v}_-).
\end{aligned}$$

□

Theorem B.7 (Incoming to outgoing Stokes vector streaming adjoint property)**.** *The streaming operators $\mathcal{T}_{-+}$ and $\mathcal{T}^*_{-+}$ defined by Eqs. (4.92) and (4.96) are adjoint:*

$$\Big\langle \boldsymbol{q}, \mathcal{T}_{-+}[\,\boldsymbol{g}\,] \Big\rangle_{\Gamma_+} = \Big\langle \mathcal{T}^*_{-+}[\,\boldsymbol{q}\,], \boldsymbol{g} \Big\rangle_{\Gamma_-}. \tag{B.11}$$

Proof. We begin with the definition of the left hand side of Eq. (B.11) and show the equality with the following steps:

$$\begin{aligned}
&\int_{\partial D} \mathrm{d}S_{\boldsymbol{x}_+} \int_{\boldsymbol{v}_+\cdot\nabla h>0} \mathrm{d}S_{\boldsymbol{v}_+} \, |\boldsymbol{v}_+ \cdot \nabla h(\boldsymbol{x}_+)| \; \boldsymbol{q}(\boldsymbol{x}_+, \boldsymbol{v}_+)^T \cdot \mathcal{T}_{-+}[\,\boldsymbol{g}\,](\boldsymbol{x}_+, \boldsymbol{v}_+), \\
&\qquad = \int_{\mathbb{S}^2} \mathrm{d}S_{\boldsymbol{v}} \int_{\boldsymbol{x}^\perp(D)} \mathrm{d}S_{\boldsymbol{x}^\perp} \sum_{t_+} \Big[\\
&\qquad\qquad \boldsymbol{q}(\boldsymbol{x}^\perp + t_+\boldsymbol{v}, \boldsymbol{v})^T \cdot \exp\left(- \int_{t_-}^{t_+} \sigma(\boldsymbol{x}^\perp + t''\boldsymbol{v}) \mathrm{d}t'' \right) \boldsymbol{g}(\boldsymbol{x}^\perp + t_-\boldsymbol{v}, \boldsymbol{v}) \Big], \\
&\qquad = \int_{\mathbb{S}^2} \mathrm{d}S_{\boldsymbol{v}} \int_{\boldsymbol{x}^\perp(D)} \mathrm{d}S_{\boldsymbol{x}^\perp} \sum_{t_-} \Big[\\
&\qquad\qquad \left(\exp\left(- \int_{t_-}^{t_+} \sigma(\boldsymbol{x}^\perp + t''\boldsymbol{v}) \mathrm{d}t'' \right) \boldsymbol{q}(\boldsymbol{x}^\perp + t_+\boldsymbol{v}, \boldsymbol{v}) \right)^T \cdot \boldsymbol{g}(\boldsymbol{x}^\perp + t_-\boldsymbol{v}, \boldsymbol{v}) \Big], \\
&\qquad = \int_{\partial D} \mathrm{d}S_{\boldsymbol{x}_-} \int_{\boldsymbol{v}_-\cdot\nabla h<0} \mathrm{d}S_{\boldsymbol{v}_-} \, |\boldsymbol{v}_- \cdot \nabla h(\boldsymbol{x}_-)| \; \mathcal{T}^*_{-+}[\,\boldsymbol{q}\,](\boldsymbol{x}_-, \boldsymbol{v}_-)^T \cdot \boldsymbol{g}(\boldsymbol{x}_-, \boldsymbol{v}_-).
\end{aligned}$$

□

Theorem B.8 (Scattering operator adjoint property)**.** *Scattering operations $\mathcal{Z}$ and $\mathcal{Z}^*$ are adjoint with respect to the internal inner product:*

$$\Big\langle \boldsymbol{p}, \mathcal{Z}[\,\boldsymbol{u}\,] \Big\rangle_{D\times\mathbb{S}^2} = \Big\langle \mathcal{Z}^*[\,\boldsymbol{p}\,], \boldsymbol{u} \Big\rangle_{D\times\mathbb{S}^2}. \tag{B.12}$$

Proof. The left hand side Eq. (B.12) is shown to equal the right-hand side by interchanging the order of integration over $\mathbb{S}^2$:

$$\begin{aligned}
\Big\langle \boldsymbol{p}, \mathcal{Z}[\,\boldsymbol{u}\,] \Big\rangle_{D\times\mathbb{S}^2} &= \int_D \mathrm{d}V_{\boldsymbol{x}} \int_{\mathbb{S}^2} \mathrm{d}S_{\boldsymbol{v}}\; \boldsymbol{p}(\boldsymbol{x},\boldsymbol{v})^T \cdot \frac{1}{4\pi} \int_{\mathbb{S}^2} \mathrm{d}S_{\boldsymbol{v}'}\; \boldsymbol{Z}(\boldsymbol{x},\boldsymbol{v},\boldsymbol{v}') \cdot \boldsymbol{u}(\boldsymbol{x},\boldsymbol{v}'), \\
&= \int_D \mathrm{d}V_{\boldsymbol{x}} \int_{\mathbb{S}^2} \mathrm{d}S_{\boldsymbol{v}'} \int_{\mathbb{S}^2} \mathrm{d}S_{\boldsymbol{v}}\; \frac{1}{4\pi} \boldsymbol{p}(\boldsymbol{x},\boldsymbol{v})^T \cdot \boldsymbol{Z}(\boldsymbol{x},\boldsymbol{v},\boldsymbol{v}') \cdot \boldsymbol{u}(\boldsymbol{x},\boldsymbol{v}'), \\
&= \int_D \mathrm{d}V_{\boldsymbol{x}} \int_{\mathbb{S}^2} \mathrm{d}S_{\boldsymbol{v}'}\; \left(\frac{1}{4\pi} \int_{\mathbb{S}^2} \mathrm{d}S_{\boldsymbol{v}}\; \boldsymbol{Z}(\boldsymbol{x},\boldsymbol{v},\boldsymbol{v}')^T \cdot \boldsymbol{p}(\boldsymbol{x},\boldsymbol{v}) \right)^T \cdot \boldsymbol{u}(\boldsymbol{x},\boldsymbol{v}'), \\
&= \Big\langle \mathcal{Z}^*[\,\boldsymbol{p}\,], \boldsymbol{u} \Big\rangle_{D\times\mathbb{S}^2}.
\end{aligned}$$

□

Theorem B.9 (Reflection operator adjoint property)**.** *The reflection operations $\mathcal{R}$ and $\mathcal{R}^*$ are adjoint:*

$$\Big\langle \boldsymbol{w}|_{\Gamma_-}, \mathcal{R}\big[\,\boldsymbol{u}_{\Gamma_+}\,\big] \Big\rangle_{\Gamma_-} = \Big\langle \mathcal{R}^*\big[\,\boldsymbol{w}|_{\Gamma_-}\,\big], \boldsymbol{u}_{\Gamma_+} \Big\rangle_{\Gamma_+} \tag{B.13}$$

Proof. The left hand side Eq. (B.13) is equated with the right-hand side by interchanging the order of integration:

$$\begin{aligned}
\Big\langle \boldsymbol{w}|_{\Gamma_-}, \mathcal{R}\big[\,\boldsymbol{u}|_{\Gamma_+}\,\big] \Big\rangle_{\Gamma_-} &= \int_{\partial D} \mathrm{d}S_{\boldsymbol{x}_-} \int_{\boldsymbol{v}_-\cdot\nabla h<0} \mathrm{d}S_{\boldsymbol{v}_-} |\boldsymbol{v}_-\cdot\nabla h| \Big[\\
&\qquad \boldsymbol{w}(\boldsymbol{x}_-,\boldsymbol{v}_-)^T \cdot \frac{1}{2\pi} \int_{\boldsymbol{v}_+\cdot\nabla h>0} \mathrm{d}S_{\boldsymbol{v}_+} |\boldsymbol{v}_+\cdot\nabla h|\; \boldsymbol{R}(\boldsymbol{x}_-,\boldsymbol{v}_-,\boldsymbol{v}_+) \cdot \boldsymbol{u}(\boldsymbol{x}_-,\boldsymbol{v}_+) \Big], \\
&= \int_{\partial D} \mathrm{d}S_{\boldsymbol{x}_-} \int_{\boldsymbol{v}_+\cdot\nabla h>0} \mathrm{d}S_{\boldsymbol{v}_+} |\boldsymbol{v}_+\cdot\nabla h| \Big[\\
&\qquad \left(\frac{1}{2\pi} \int_{\boldsymbol{v}_-\cdot\nabla h<0} \mathrm{d}S_{\boldsymbol{v}_-} |\boldsymbol{v}_-\cdot\nabla h|\; \boldsymbol{R}(\boldsymbol{x}_-,\boldsymbol{v}_-,\boldsymbol{v}_+)^T \cdot \boldsymbol{w}(\boldsymbol{x}_-,\boldsymbol{v}_-) \right)^T \cdot \boldsymbol{u}(\boldsymbol{x}_-,\boldsymbol{v}_+), \Big] \\
&= \Big\langle \mathcal{R}^*\big[\,\boldsymbol{w}|_{\Gamma_-}\,\big], \boldsymbol{u}|_{\Gamma_+} \Big\rangle_{\Gamma_+}.
\end{aligned}$$

□